TESIS DE LA UNIVERSIDAD DE ZARAGOZA

2012

24

Juan Antonio Ramírez Vázquez

A computational fluid dynamics investigation of turbulent swirling burners

Departamento

Instituto Universitario de Investigación Mixto CIRCE

Director/es

Cortés Gracia, Cristóbal

ISSN 2254-7606

Prensas de la Universidad Universidad Zaragoza

Universidad Zaragoza
1542

Tesis Doctoral

A COMPUTATIONAL FLUID DYNAMICS INVESTIGATION OF TURBULENT SWIRLING BURNERS

Autor

Juan Antonio Ramírez Vázquez

Director/es

Cortés Gracia, Cristóbal

UNIVERSIDAD DE ZARAGOZA

Instituto Universitario de Investigación Mixto CIRCE

2012

Ph.D. Thesis

A COMPUTATIONAL FLUID DYNAMICS INVESTIGATION OF TURBULENT SWIRLING BURNERS

By Juan Antonio Ramírez Vázquez

May 2012

Advisor:

Cristóbal Cortés Gracia, Ph.D.

Instituto CIRCE

Escuela de Ingeniería y Arquitectura

Universidad de Zaragoza

A mis padres y mi esposa

A computational fluid dynamics investigation of turbulent swirling burners

Juan Antonio Ramírez Vázquez

Thesis submitted in partial fulfillment of the requirements for the degree of Doctor of Philosophy

University of Zaragoza, Spain

Abstract

This thesis presents detailed numerical calculations of the Unsteady, Reynolds-Averaged Navier-Stokes (URANS) equations to simulate isothermal, single-phase flow in the geometries of realistic swirl burners at large Reynolds numbers. Simulations are run with two different turbulence closures, viz., the standard $k-\epsilon$ and Reynolds stresses (RSM) models. The numerical method is validated concerning convergence, grid density and far-field influence. Results describe a flow that is in any case periodic or pseudo-periodic, and exhibits quite convincing time-dependent features: bubble- and spiral-type vortex breakdowns and vortex core precession. Some simulations are validated by comparison with corresponding experiments. Good agreement with the experiments has been obtained for mean flow, and frequency peaks of the power spectral density of

pressure fluctuations.

In order to asses the reliability of URANS methods within this context, calculated time-averaged flow and coherent structures are documented via 2D graphs, spectral analysis, 3D isosurfaces and advanced, vortex-related visualization methods and 2D snapshot proper orthogonal decomposition (S-POD). Differences arising from the nature of the turbulence model ($k - \epsilon$ vs. RSM) are very relevant indeed, given the cost factor involved and the apparent verisimilitude of the predicted flow; they are thoroughly analyzed.

A computational fluid dynamics investigation of turbulent swirling burners

Juan Antonio Ramírez Vázquez

Tesis realizada para cumplir con los requisitos del grado de Doctor

Universidad de Zaragoza, España

Resumen

Esta tesis presenta cálculos numéricos pormenorizados de las ecuaciones URANS para simular flujo isotermo, monofásico en geometrías reales de quemadores de giro inducido a grandes números de Reynolds. Las simulaciones se ejecutan con dos modelos de turbulencia diferentes, a saber, el modelo $k-\epsilon$ estándar y el modelo de esfuerzos de Reynolds (RSM). El método numérico se valida con referencia a la convergencia, a la densidad de malla y a la influencia de la posición del campo lejano. Los resultados describen un flujo que es en cualquier caso periódico o falso-periódico, y expone de manera convincente las siguientes características temporales: rompimiento de vórtice del tipo burbuja y espiral y el movimiento de precesión de núcleo de vórtice. Algunas de las simulaciones se validan mediante la comparación con sus respectivos experimentos. Se ha

obtenido una buena concordancia entre los datos experimentales y el flujo medio y los picos de frecuencia de la densidad de potencia espectral de las fluctuaciones de presión.

Para garantizar la confiabilidad del uso de las URANS, el flujo promedio temporal y las estructuras coherentes se justifican mediante gráficas en 2D, análisis espectral, isosuperficies en 3D, técnicas de visualización de vórtices avanzadas y descomposición ortogonal propia instantánea en 2D (S-POD) . Las diferencias que surgen de la naturaleza de los modelos de turbulencia ($k - \epsilon$ vs. RSM) son muy relevantes, debido al factor de costo involucrado y la aparente verosimilitud del flujo previsto; todo ello se analiza detenidamente.

Agradecimientos

Esta Tesis doctoral ha sido financiada por el ministerio Español de Ciencia e Innovación con los proyectos TERMOPIV *ENE2006-13617/CON* y BIOSWIRL *ENE2007-65072/ALT*.

Quiero agradecer a al Profesor Cristóbal Cortés por su guía, apoyo y paciencia. Sin su pasión por la investigación y sus consejos científicos este trabajo no habría sido posible. Ha sido un honor haber trabajado contigo.

Me gustaría agradecer profundamente al Profesor Abel Hernández Guerrero, pues fue él quien me introdujo en el campo de la fluidodinámica computacional y me enseñó el camino de la investigación.

A Mathieu Legrand de la Universidad Carlos III por compartir sus resultados experimentales, gracias a ello fue posible validar este trabajo.

También quiero agradecer al Instituto CIRCE por su apoyo financiero, a su Director Antonio Valero por su confianza y a todos los investigadores e investigadoras por el excelente ambiente de trabajo. En especial debo agradecer a los miembros del Área de Sistemas Térmicos. Ha sido un placer para mí haber trabajado con gente tan capaz, inteligente y responsable, su compromiso con la investigación es admirable, ojalá no se pierda nunca.

Hace años, cuando llegué a Zaragoza, no sabía lo que se presentaría en mi estancia por la ciudad. Al principio creí que era una etapa más. Luego, me di cuenta lo afortunado que era pues estaba rodeado por personas más que valiosas. Mil gracias por estar incondicionalmente en lo bueno y en lo malo. A Ana G. por su bondad. A Ana M. por su alegría. A Amaya por compartir su fortaleza. A Carlos H. por su sentido del humor. A Guille por la música. A Javi por estar hecho de

otra pasta. A Josemi por su confidencialidad. A Luisig por su generosidad, su honestidad, su honradez y su profesionalidad, nadie como él. A Miguel por su lealtad. A Pilar por darme el mejor consejo que alguien me ha dado nunca. Y a Sergio por su confianza y sus incalculables y acertados consejos. Sin duda, Ustedes son las mejores personas que he conocido en mi vida.

Un agradecimiento al grupo con el que compartimos antojitos, mucha charla y muy buenos momentos: Carlos y Mayra, Don Carlos, Bety y Manuel Alberto, Jesús, Miguel, Agustín y Margarita, Andrea y Mauricio.

Gracias a mis padres por haberme ensañado a ser lo que soy, gracias por su respaldo, por ayudar siempre a levantarme y por alentarme a nunca darme por vencido. A mis hermanos por tantos momentos compartidos y a la más pequeña de la familia, Marifer.

Finalmente, Gaby, quiero pedirte perdón por todos los momentos duros que te ha generado esta tesis. Nos ha robado mucho tiempo, espero que lo podamos recuperar. Gracias por estar a mi lado.

Contents

List of Figures

List of Tables

Nomenclature

A	snapshot data matrix
A_i	cross-sectional area of the primary air inlet
C	nonnegative Hermitian matrix
C_μ	constant
D	diameter of the annular pipe for secondary air
D	symmetric part of the velocity gradient tensor
E	expansion ratio of diameters ($= D_o/d_i$)
F	unitary $M \times M$ matrix
F_k^e	the kth component of the Fourier transform of length $N/2$ formed from the even components

F_k^o the kth component of the Fourier transform of length $N/2$ formed from the odd components

Fs factor of safety

GCI_{fine}^{ij} grid convergence index using the i^{th} and j^{th} grid

$G^\dagger$ unitary $N_t \times N_t$ matrix, conjugate transpose of G

H_n complex amplitudes

I turbulence intensity

M number of realizations of $u(\mathbf{x}, t)$

N number of samples

N_c number of cells

N_t number of intervals of time

Q_{2D} second invariant of $\nabla \mathbf{u}$

R two-point spatial correlation tensor

Re Reynolds Number

S_w geometric swirl number

W complex number

$\langle \cdot \rangle$ average operator

$\mathbf{A}_\lambda$ matrix for the calculation of the invariants of the velocity gradient tensor

$\nabla \mathbf{u}$ velocity gradient tensor

$\sum$ diagonal matrix

‘V^i temporal eigenfunctions

$\mathbf{X}$ variable assimilated to the space $\mathbf{x}$ defined over the domain Ω_s

$\mathbf{x}$ spatial coordinate $\mathbf{x} = (x, y, z)$

$a^{(k)}(t)$ POD coefficients

c_n complex coefficients

d diameter of the annular pipe for primary air

e_a^{ij} approximate relative error using the i^{th} and j^{th} grid

e_{ext}^{ij} extrapolated relative error using the i^{th} and j^{th} grid

$h(t)$ time function

h_k sampled function

h_{coarse} size of the coarse grid

h_{fine} size of the fine grid

k turbulence kinetic energy

l integral length scale

p grid apparent order

r grid refinement factor

r_o outer radius

t temporal coordinate

$u(\mathbf{x}, t)$ vector-valued function

u_i inlet velocity

u_{num} standard uncertainty

y^+ normalized distance from the wall

St Strouhal number ($= 2E^2 f d_i / \sqrt{\pi} u_p$)

rsm root mean square

Acronyms

AR Autoregressive

ARMA Autoregresive Moving Average

CS Coherent Structure

DNS Direct Numerical Simulation

FFT Fast Fourier Transform

GCI Grid Convergence Index

HV Helical Vortex

IEA International Energy Agency

IRZ Inner Recirculation Zone

IV Inner Vortex

LDA Laser Doppler Anemometry

LES Large Eddy Simulation

MA Moving Average

ORZ Outer Recirculation Zone

OV Outer Vortex

PIV Particle Image Velocimetry

POD Proper Orthogonal Decomposition

PSD Power Spectral Density

PVC Precessing Vortex Core

RANS Reynolds Averaged Navier-Stokes

RE Richardson Extrapolation

RSM Reynolds Stresses Model

S-PIV Stereo-Particle Image Velocimetry

URANS Unsteady Reynolds Averaged Navier-Stokes

Greek Letters

$\mathbf{\Phi}(\mathbf{x})$ POD modes matrix

Δt time step

ΔV_i volume of the i^{th} cell

$\delta_{k_1 k_2}$ Kronecker delta

δ_{num} numerical error

ϵ dissipation rate per unit mass

ϵ_{ij} $\epsilon_{ij} = \phi_i - \phi_j$

λ eigenvalues

λ_i $i^{th} eigenvalue$

Ω antisymmetric part of the velocity gradient tensor

ω_θ azimuthal vorticity

Ω_s spatial domain

ω_z axial vorticity

ϕ control variable

ϕ_{ext}^{ij} extrapolated values using the i^{th} and j^{th} grid

$\phi^k(\mathbf{x})$ basis function for POD approximation method, POD modes

ϕ_v vane angle (circumferential direction)

σ standard deviation

τ dimensionless time ($= u_i t/d_o$)

Subscript/Superscript

$_{,\theta}$ partial derivate with respect to angular coordinate

$_{,r}$ partial derivate with respect to radius

$_{,z}$ partial derivate with respect to axial coordinate

Chapter 1

Scope, aims and outline of this Thesis

This thesis describes the study of Unsteady Reynolds Averaged Navier-Stokes (URANS) schemes for the simulation of isothermal flow in swirl burners. The aim of the present thesis is to demonstrate that URANS can simulate complex swirl flows with good quality compared to experimental data. The thesis proposes also that the use of URANS can provide enough information to understand the complex dynamics of the coherent structures in these flows.

In the Introduction (Chapter 2) the complex swirl flow and its role in the generation of coherent structures and vortex breakdown is reviewed, with special emphasis in numerical simulations. The structure and dynamics of different types of vortex breakdowns are described as well as their link with coherent structures. Furthermore, advances in the field of computational fluid dynamics research in turbulent swirl flows are discussed in the context of non-reactive flow.

Chapter 3 gives an overview of numerical methods used for pre-processing and post-processing data such as grid convergence index (GCI), fast Fourier transform

(FFT), proper orthogonal decomposition (POD) and λ_2 coherent structures visualization technique. Grid convergence index (GCI) assures a grid-independent solution based on a study of the convergence of average magnitudes, in other words, GCI is a method for estimating the standard uncertainty associated with numerical errors. Fast Fourier transform is used as a tool of spectral analysis of the oscillations in the flow. Proper orthogonal decomposition (POD) and λ_2 coherent structures visualization technique are two advanced and specialized criteria to study and identify flow features such as precessing vortex core (PVC), coherent structures and detached vortices.

Results of URANS schemes for the simulation of isothermal single-phase flow in a burner of pulverized solids are described in Chapter 4. The geometry of swirl generation is completely realistic, comprising a tangential inlet for primary air (fuel transport) and movable guide vanes for secondary air. To model turbulence, two different schemes are used: second order closure by a Reynolds Stresses Model (RSM) and the $k-\epsilon$ model. In both cases, the model is kept intentionally simple, with no modifications over the standard version. Special concern is taken in assuring a grid-independent solution, by studying the convergence of average magnitudes, and also the characteristics of the oscillations numerically reproduced. The upstream placement of fluid inlets, which is relevant both for the real equipment and the economy of the calculation, turns out to have a pronounced effect on the oscillations, and then on the mean flow; the effect is documented at length.

In Chapter 5, a complete analysis of URANS schemes applied to simulate an atmospheric low swirl burner under isothermal conditions is described. This

burner was designed and investigated by Legrand et al. [94, 95]. Reynolds Stress Model (RSM) and the $k-\epsilon$ model schemes are also used to model turbulence. Grid-independent solution is assured following the same procedure as in Chapter 4 for the confined burner. Flow features are compared with stereo particle image velocimetry (S-PIV) measurements published by Legrand [94].

Dominant structures are also studied in Chapters 4 and 5 using the advanced post-processing techniques described in Chapter 3, with special attention to the PVC, coherent structures and detached vortices. The relation between the oscillations and the coherent structures is analyzed.

Finally, Chapter 6 presents a summary and a general discussion on the major results. New contributions and recommendations for continuing research are also included.

Chapter 2

Introduction

2.1 Motivation

Combustion of primary energy sources is the main source to produce electrical and mechanical energy. According to the statistical report of the International Energy Agency (IEA), in 2008, the 81.3% of primary energy was consumed for this purpose [77]. In 2030, consumption will remain high: 68.1%. For this reason, the effort must to be focus to study, develop and/or modify combustion devices to burn more efficiently. Actually, swirl is one of the main technologies used in new burners. Their application allows to stabilize lean flames in gas turbine burners or to provide stable and complete combustion of solids in industrial power boilers [64]. Unfortunately, swirl generates very complex patterns in the flow in form of vortex breakdown and coherent structures. Külsheimer and Büchner [86] suggest that the formation of these vortical structures are the main mechanism which is

responsible of the instabilities in a combustion process. For this reason, it is very important to study the formation of vortex breakdown and coherent structures [6]. Although the application centers on reacting flows, an adequate modeling of isothermal flow is the first step to the adequate modeling of coupled variable density, escalar transport and reaction. We therefore limit the study to isothermal flow conditions. Swirl is applied also in these conditions, for instance in cyclones and swirl tubes.

2.2 Swirl Phenomena, Vortex Breakdown and Coherent Structures

Swirl is employed in diverse technical applications: as a means to effect separation in cyclones, to enhance heat transfer in heat exchangers, to stabilize lean flames in gas turbine burners or to provide stable and complete combustion of solids in industrial and power boilers [64, 170, 154]. Whenever substantial swirl is present, even at moderate Reynolds numbers, the flow usually develops vortex breakdown and coherent structures. According to Benjamin [10] and Squire [147], vortex breakdown can be conceived as a critical phenomenon of swirling flows, much like an hydraulic jump in a channel. Escudier and Sehnder [38] identified three basic types: axisymmetric, spiral, and double helix; other intermediate forms have been observed depending upon the particular combination of Reynolds and swirl numbers [99, 130]. At high Reynolds numbers, it has been reported that the core initiates a kink, followed by a spiral [111]. At a value large enough, bubble and

spiral structures are suppressed and the flow transforms into a nominally axisymmetric cone of swirling turbulent flow. Sarpkaya [131] considers this the fourth fundamental type. Reviews of the topic have been given by Sarpkaya [130], Hall [66], Leibovich [97], Escudier [33] and Lucca-Negro and O'Doherty [101].

For swirling flows at high Reynolds numbers, different patterns of coherent structures (CS) have been documented by advanced experimental methods (LDA and PIV measurement and visualization), both at isothermal and non-isothermal conditions: precessing vortex core (PVC), inner and outer recirculation zones, and inner and outer secondary helical vortices [47, 20, 156]. Fick et al. [42] observed how the PVC continuously changes its shape and appearance many times within a single cycle, rotating clockwise and twisting anticlockwise against the direction of the rotating fluid. The basic explanation of a backflow due to the dissipation of the main vortex (e.g., Syred [151]) continuous to hold, but it is clear that it fails to produce a steady flow, causing instead the formation of secondary, non-axisymmetric, unsteady structures [116]. Under non-isothermal conditions (e.g., combustion), flow changes mainly through density; the effect is generally stabilizing, but oscillations may persist, and also acoustic coupling can appear [68, 164, 124, 132, 65, 163, 107, 152]. For reviews of PVC and its influence in isothermal and combustion systems see e.g. Syred [151] and Huang and Yang [75].

2.3 Use of Computational Fluid Dynamics in Swirl Flows

The current status in computational studies of swirling flows can be summarized as follows. Direct numerical simulation (DNS) has been used with success to reproduce and investigate the complex features of isothermal flows at moderate-to-low Reynolds numbers. Some examples are the study of the dinamycs of a swirling jet at Re = 500 of Guohuiet et al. [63] , the fundamental studies of Ruith et al. [125] and Gallaire et al. [49] at Re = 200, the analysis of scalar transport of Freitag et al. [44, 45], at Re = 5 000, the mixing properties enhancement of coaxial jets of Balarac et al. [8, 7], and the simulation of (modeled) two-phase swirling jets of Siamas et al. [140] at Re = 2 000.

For practical conditions, turbulence has to be modeled to some degree. In the extreme of maximum simplicity and minimum cost, closure of the Reynolds Averaged Navier-Stokes (RANS) equations has been practiced since more than two decades for many realizations of swirling flows, leading to apparently realistic steady-state solutions that exhibit backflow, see e. g. the axisymmetric calculation by Mondal et al. [109] and Kriaa et al. [85]. However, in modern times, a variety has emerged called Unsteady RANS (URANS) that presents a clear advantage for unstable swirling flows. Operationally, a URANS simulation simply consists in retaining the time derivatives of the RANS equations while relying as usual on a standard, steady-state turbulence model. Then, for some flows and depending also on the specific model, a periodic or pseudo-periodic, converged solution is

found, even with steady boundary conditions [142]. At the beginning, the effect was thought to be a purely numerical artifact, and the scheme considered not physically sound for turbulent flows. But soon it became clear that a URANS scheme is simply an economical way of simulating flows that develop discrete natural frequencies, for which it is very superior to steady RANS [31, 76].

Accordingly, URANS simulations have been attempted for a variety of swirling flow geometries. Guo et al. [61] used the standard $k-\epsilon$ formulation to model a suddenly expanded jet, and successfully reproduced the PVC and detached vortices. Jakirlic et al. [79] analyzed three versions of the second-moment closure and two eddy-viscosity models when simulating swirling and rotating pipe flows. They observed that the standard $k-\epsilon$ model invariably results in unrealistic steady-state, solid-body rotation, which was attributed to poor rendering of streamline curvature effects. More refined turbulence modeling was needed, RSM giving the best performance. Cortés and Gil [26] arrived at a similar conclusion after the simulation of gas flow in a cyclone separator. The fact that the $k-\epsilon$ model can lead to excessive dissipation in coarse grids has been also signaled as the ultimate reason for steady-state URANS solutions that are not physically sound. Advanced RSM has been used by Ali and Georgios [4] in confined geometries and by Jochmann et al. [81] in expanded jets to demonstrate that URANS schemes can realistically predict time-dependent features of turbulent swirling flows.

On the other hand, Large Eddy Simulation (LES) is used more and more for advanced calculations, and swirling flows are not a exception. Some noteworthy examples are the studies of large-scale coherent structures and scalar mixing of Garcia-Villalba et al. [51] and Fröhlich et al. [46], the simulation of aerodynamic

noise by Flemming et al. [43], the effects of the confinement in a combustor by Lin Lin [100], Stone and Menon [149] and Grinstein and Fureby [60], and . For pulsating flows not dominated by wall phenomena, LES is obviously well adapted, although approximate modeling is normally needed for wall regions in closed geometries. In spite of this, a rigorous application of the technique requires much higher spatial and temporal resolution than any model of the effect of turbulence on the mean flow, and this acquires a special relevance when considering URANS schemes. Likewise, LES also requires very long integration times to build an ensemble-averaged solution [5], whereas just a few periods are usually enough in URANS, since the solution tends to be of a deterministic nature.

For these reasons, the prediction that RANS-based simulations, albeit less reliable, will remain useful and competitive versus LES [67] has been mostly accomplished, specially for the kind of flows we consider here (see also e. g. Wegner et al. [161]). In addition, the necessity of simulating complex processes where different physics merge and interact also puts a limit on the computational cost of the models that can be used. LES has now successfully surpassed the barrier of single-phase, isothermal flow calculations. Some significant contributions related to swirling flows are the works of Wegner et al. [161] on non-premixed combustion with fast chemistry, Derksen et al. [30] on interacting gas-particle flow in cyclone separators and Duwig and Fuchs [32] on vortex/flame interaction in premixed combustion via flamelet models. However, as it is obvious, many real-world situations are much more complex. For instance consider a swirl-stabilized combustor of pulverized solids. A complete simulation would need to model transport of mass, species, momentum and energy, in the gas phase

and solid particles, under homogeneous and heterogeneous chemical reactions, by flow, diffusion, turbulence, and gaseous and particle thermal radiation. It is clear that such a calculation cannot afford LES schemes for the flow and retain at once reasonable models for the remaining phenomena. Instead, a steady calculation based on RANS and a classical turbulence closure are used, and, when pulsating phenomena and coherent structures can be of interest, URANS is a good starting point. LES has obvious advantages for coupled phenomena; for instance, as signaled in [104, 105], it can render unnecessary a model for the turbulent dispersion of particles, which is mandatory in RANS or URANS. However, computational cost still favors URANS, specially when the complexity and modeling needs of the situation are high. A good example of this use of URANS are Ref. [127, 134], where advanced combustion models for partially premixed, swirling-flow systems are studied.

2.4 Vortex Breakdown Review

The phenomenon of vortex breakdown is an abrupt change of flow structure with a very pronounced retardation of the flow along the axis and a corresponding divergence of the stream surfaces near the axis. Numerous theoretical and experimental investigations over the last 4 decades have been carried out to understood this fluid dynamical phenomenon. But despite the effort, actually, the vortex breakdown is poorly understood. In this section these issues are reviewed and discussed.

2.4.1 Theoretical Studies

Theoretical work on vortex breakdown can be classified into three main categories: (1) theories based on hydrodynamic instability, (2) theories based on deceleration of axial flow leading to stagnation, and (3) theories based on a transition from one flow state to another.

Theory of hydrodynamic instability proposes that vortex breakdown (VB), with a local stagnation of axial flow, is a direct consequence of hydrodynamic instability with respect to spiral disturbances. This is, the spiral disturbances might be amplified and induce an asymmetry in the vortex core, which could readily lead to stagnation when there was a total pressure defect in the core, or in other words, the vortex breakdown is associated with a range of velocity gradients. Stuart [150] observed that hydrodynamic instability appears to be insensitive to downstream boundary conditions which is contrary to the observations in a vortex breakdown. In fact, experiments of Brücker et al. [18, 17, 19] demonstrated that spiral and axisymmetric forms are found in the same continuous range and are even interchangeable in the appropriate flow conditions. For instance, application of downstream suction results in a vortex flow without breakdown. Thus, flow instability as a mechanism is considered unimportant.

Hall [66] suggests that this explanation cannot be regarded as satisfactory. Because spiral and axisymmetric forms are found in the same continuous range and even interchangeable. Moreover, in a range of velocity gradients there will be instabilities somewhere.

Axial deceleration is a natural tendency of swirling flows that are dominantly

axisymmetric. In a vortex, the axial pressure gradient on the axis is higher than elsewhere. Brown and Lopez [16] proposed a breakdown criterion which states that the helix angle for velocity must be larger than the helix angle for vorticity.

Before the theory suggested by [10], there were several attempts to account for the phenomenon theoretically. Some of them explained it as the outcome of instability of the original flow. Benjamin [10] proposed that it is a finite transition between two dynamically conjugate states of axisymmetric flow, analogous to the hydraulic jump in open channel flow. In other words, Benjamin [10] explains vortex breakdown to be a finite amplitude transition from supercritical state of flow to a conjugate subcritical state. As in channel flow, "sub-" and "supercritical" are interpreted by analogy with sub- and supersonic gas flow: a flow having velocity respectively smaller or larger than that of a disturbance. Contrary to this analogy, nature of the disturbance which makes a good definition (superficial wave in a liquid, sound in a gas), is not clear here. Recently, Ruith et al. [125] show that a transition from super- to subcritical flow as defined by Benjamin [10] accurately predicts the parameter combination yielding breakdown, if applied locally to a flow with supercritical inflow profile. Moreover, they proposed the concepts of local absolute (AI) and convective (CI) instability and their implications for global instability of a spatially developing flow to explain the VB phenomenon.

In [147], it is proposed that waves present in a flow, when the maximum swirl is rather larger than the axial velocity, are conditions for vortex breakdown. This theory estimate the "critical" value of the swirl angle to lie between 45° and 50.2°. This "critical" value is considered as the onset of a bubble type vortex breakdown.

2.4.2 Experimental Studies

Harvey [69] investigated the VB in a controlled laboratory experiment in which the swirl angle could be varied. He defined the swirl angle as the inverse tangent of the ratio of maximum axial velocity to the maximum swirl velocity. He observed onset of a bubble type of vortex breakdown at a critical value of the swirl angle of about $50.5°$. Value which agrees with Squire theory [147], where the critical value is lies between $45°$ and $50.2°$. The experiments of Harvey also showed that the bubble shape was nearly axisymmetric and the flow downstream of the bubble nearly resembled the parallel flow upstream. Some researchers suggested that this flow behaviour is governed by two different mechanisms: hydrodynamic instability and finite-transition to a sequent state [130, 66]. Recently, Mourtazin and Cohen [110] included buoyancy effects to enhance the criterion for the onset of vortex breakdown.

Sarpkaya [130] observed three types of VB: double helix breakdown, spiral breakdown and axisymmetric breakdown. The type and the shape of the intermediate forms depend upon the particular combination of the Reynolds and swirl number. Faler and Leibovich [39, 40] had made elaborate studies including flow visualization and quantitative measurements. They observed seven distinct structures of vortex breakdown (numbered from 0 to 6). The authors describes clearly the structure of each vortex breakdown type. The type 0, type 2 and type 5 are the bubble, spiral and double helix types, respectively. They concluded that all flows that exhibit vortex breakdown of the bubble (type 0) form and/or spiral form (type 2) are supercritical upstream. Moreover, they claim that the axisymmetric

vortex breakdown is a misnomer that may have lead to the over-emphasis of axial symmetry in theoretical work. For spiral form if Reynolds number or circulation number is increased, the frequency of rotation of the spiral is increased too. With respect to the quantitative measurements, they suggest that the inner eddy presumably is connected with the strong, very angular, azimuthally asymmetric fluctuations that occur inside the recirculation.

Garg and Leibovich [54] reported that flows with VB contain prominent oscillations in identical experimental conditions to those of Faler and Leibovich [39, 40]. They found that power spectra is more energetic for the bubble type of breakdown than for the spiral form.

Escudier et al. [34] (also see [35, 38, 36, 33, 37]) elaborated studies based on laser Doppler anemometer (LDA) measurements. They used an inlet cylindrical tube coupled with a contraction followed often by a divergent section. The experiments describe the fundamental types of VB: spiral, double helix, and bubble form. In this sense, they propose that the transition in a vortex breakdown involves two stages, the first isentropic from the initial supercritical state to an intermediate state which is also supercritical. The second stage of the transition, to the downstream supercritical state, is non-isentropic, much like a hydraulic jump or shock wave. In other words, the first transition is both isentropic and also involves no change in the flow force even for a large scale transition. They suggest that there is no fundamental difference between the so-called spiral type of breakdown and the axisymmetric bubble type. Moreover, they suggested that the specification of the downstream boundary conditions must be located where the swirl has fallen to a sufficiently low level that the flow is again supercritical.

Brücker and co-workers investigated the bubble-type VB [18], the spiral-type VB [17] and their time-dependent nature [19]. They used a vertical low speed water-channel with the particle tracking velocimetry (PVT) technique for measurements. The two-dimensional velocity field and the vorticity distribution show the existence of a single vortex ring in the lower part of the bubble which is tilted against the centerline and spins around it. They suggested that this vortex ring is the responsible of the strong pressure gradient. With respect to the spiral-type VB, they found that the stagnation point is not located on the centerline as often supposed but rotates around it. This behaviour may be the explanation of the low periodic fluctuations inside the breakdown region. The sense of the spiral's winding is opposite to the sense of basic flow rotation. They conclude that the spiral is nothing but a bubble with an off-axis stagnation point that rotates around the vortex axis. In the time-dependent analysis, they observed that spiral-type VB should be viewed as the result of the bubble's instability because the topological characteristics of the spiral and its front part indicate its origin from the bubble-mode [87, 99]. In other words, just a certain degree of asymmetry initiates the transition to the spiral. These topological characteristics were also identified by Sheen et al. [136] which observed seven regions in a vortex breakdown: stable flow, vortex shedding, transition, pre-penetration, penetration, vortex breakdown, and attachment.

Almost all experimental studies of vortex breakdown use confined configurations for measurements. Khoo et al. [83] observed all seven modes of vortex breakdown documented by Faler for a confined flow [39]. They found that vortex core disrupted in filament disruption, double helix disruption, flattened bubble or

spiral breakdown at very low Reynolds numbers ($300 \leq Re \leq 750$); bubble and spiral breakdown are rather unstable. Spiral vortex breakdown occurs at a Reynolds number range of $750 \leq Re \leq 2000$ and a swirl ratio range of $2.5 \leq S \leq 18$. They observed that the whole spiral structure rotates about the centerline in the same sense as the outer flow rotation. At Reynolds number range of $2000 \leq Re \leq 3200$ three types of VB can be formed: closed bubble breakdown, open bubble breakdown and spiral breakdown. The open bubble breakdown is the Type 1 breakdown and the closed bubble breakdown is the Type 0 of those reported by Faler et al. [39]. In the range of $3200 \leq Re \leq 3600$ and $2.9 \leq S \leq 9.5$, the vortex breakdown observed is conical breakdown, documented by Sarpkaya [131].

Vortex breakdown was also characterized by Billant et al. [14] using a swirling water jet. They identified four distinct forms of vortex breakdown: the well documented bubble state, a cone configuration in which the vortex takes the form of an open conical sheet, and two associated asymmetric bubble and asymmetric cone states. In the experiments, the confinement effects can be assumed as negligible since the jet exhausts into a large water tank. For the case of asymmetric bubble, they claim that this structure correspond to the spiral mode of breakdown; differs from the bubble by the precession of the stagnation point around the jet axis. The asymmetric cone is a variation on the cone in the same way as the asymmetric bubble on the bubble. Both asymmetric states are observed at large Reynolds numbers.

The basic features that have emerged from the experiments are: (1) abrupt and drastic structural changes occur in a vortex breakdown, (2) axial flow in the core decelerates, sometimes resulting in stagnation and reversal flow, (3)

the flow is unsteady within the breakdown structure and turbulent downstream, (4) axisymmetric breakdown is characterized by slow oscillations, and (5) the breakdown itself is not a result of instability but a sudden and finite transition from one state to the other as suggested in Harvey [69].

Patte-Rouland et al. [113] studied the recirculation zone in an annular jet using POD analysis of PIV measurements. They observed the interaction of the layers: one between the layer which separates the jet flow and the recirculation zone and the other one which separates the jet flow with the surrounded air. The same interaction between shear layers were analyzed in [73] for four modes of flow structures: bubble, dual rings, vortex breakdown, and vortex shedding. They observed an off-axis saddle point which induces large turbulence intensities. The same large turbulence intensities were observed for a non-swirling flow by Tim et al. [15]. Some other studies have been focused in the analysis of the interior of the bubble vortex. Giannadakis et al. [57] identified low azimuthal vorticity values in the upstream region, close to the swirling nozzle and higher ones in the region between the vortex ring core and the bubble's aft in addition to low turbulent dynamics inside the bubble. Similar results were observed by Ivanic et al. [78], Liang et al. [98] and Vanierschot et al. [158]. These shear layers have been also identified in combustion applications where the reaction zones are formed at the outer or inner shear layers [59, 74, 126].

The size of the recirculation zone increases when a secondary coaxial stream is added [119, 93]. Lee et al. [93] found that the recirculation zone increases up to above 36% compared with the case of no secondary stream, depending on the pressure ratio of the secondary stream. The swirl direction of the secondary

stream does not significantly change the pressure distributions along the jet axis. The secondary stream of counter-swirl reduces the size of the recirculation region compared with the size recirculation of co-swirl. Another important feature which alters the recirculation zone is the type of injection topologies, i. e., co-axial and radial, leading to different mixing mechanisms and, hence, altering the recirculation zone [112]. Shtork et al. [137, 139] confirmed that the time-averaged flow field characteristics indicate the usual features of swirling jet breakdown with central reverse flow, while phase averaged analysis shows an asymmetrical flow pattern with the vortex core center shifted away from the nozzle axis. On the other hand, Alekseenko et al. [1, 2] show the evolution of the recirculation zone size. Moreover, an intense generation of turbulence was observed in the initial region of the jet leading by the vortex breakdown. The intensity of this turbulence (the Reynolds stress $\langle uv \rangle$ and third-order moments) was about 5 times higher than in the rest of the flow domain. The forcing increases the total turbulence kinetic energy, but it does not affect the mean flow. They observed that large-scale structures rotating in the opposite direction to the mean flow are responsible for the mixing enhancement. In addition, the results of Coghe et al. [25] show the evidence of different recirculation regions which influence the main combustion features. A toroidal central recirculation region influences reactants mixing and flame stabilization [27, 24, 12, 146, 13, 84]. The corner recirculating zone induces entrainment of a large amount of hot burned gases into the outflowing reactant mixture while the recirculation zone acts as a bluff-body [168, 153, 160, 159, 148, 156].

Another important coherent structure present in swirl flows is the precessing vor-

tex core (PVC). The PVC is a three-dimensional time-dependent CS developed in the exhaust nozzle [106]. Froud et al. [47] and Selle et al. [135] claim that the PVC is caused by the displacement of the center of the vortex. Moreover, they also observed a similar displacement from the axis of symmetry of the recirculation zone which rotates through a region of forward flow. This mechanism provides stabilization and increases the mixing processes when combustion is present [165]. Schneider et al. [133] used LDA to investigate fluid dynamical features caused by combustion process in an atmospheric burner. They observed that downstream axial velocity is maintained while tangential momentum is passed over to radial momentum. A precession of the IRZ was observed leading to distinct frequencies in the PSD when it is compared with reacting case.

Fick et al. [42] visualized the PVC and RZ in a combustion process. They observed that the PVC continuously changes its shape and appearance many times within a single cycle in addition to it rotates clockwise and is twisted anticlockwise against the direction of the rotating flow. Schildmacher [132] linked the presence of a PVC with thermo-acoustic instabilities and their interaction with the periodic fluctuations of the velocity and pressure. In addition, they found a phase lag between the different signals.

2.4.3 Numerical Studies

The main advantage in the use of numerical simulation for the analysis of complex flows is that it allows to understand flow features by means of a detailed

explanation of the structure and dynamics for isothermal and non-isothermal flows [145, 167, 56, 170, 129, 108, 55, 171]. Spall et al. [144] compared the topological structure of four different types of vortex breakdown (weak helical, double helix, spiral and bubble-types) with the experimental analysis made by Faler and Leibovich [39]. They identified velocity fluctuations which are responsible of the exchange of fluid between the inner zones and the free stream. Moreover, these types of vortex breakdown exhibit an axial stagnation point which indicates the origin of the location of VB [11]. This location depends on a number of parameters: the core Reynolds number, the flow divergence, the swirl velocity ratio, and the strength of the vortex. The breakdown location moves upstream as the core Reynolds number increases, or the initial adverse pressure gradient increases. Some studies have shown that the transition between different types of vortex breakdown are caused by absolute instabilities inside of the recirculation zone [70].

Reynolds-averaged Navier-Stokes (RANS) and unsteady RANS play an important role in the approach of the computation of turbulent flows and heat transfer especially in industrial applications. Some studies assess the performance of different turbulence modes for predicting isothermal flow in complex combustors [82]. RANS models are capable of predict mean and turbulent flow quantities reasonably well except near the wall [82].

Standard $k - \epsilon$ model is the most frequently used model over the past three decades. It has been also used in the prediction of the precessing vortex core. Guo et al. [61, 62] claim that the turbulence model performs extremely well for swirl flow and conclude that the intensive mixing after the breakdown may be

produced primarily by the small-scale turbulence rather than the large-scale flow entrainment. However, the application of the standard $k-\epsilon$ model in swirling flows results in a solid-body rotation flow under some circumstances [79]. Despite this, the standard $k-\epsilon$ is capable to predict the central recirculation zone with enough detail in terms of size, location and strength [109]. Moreover, it is possible to use it to model swirl effect in combustors with good accuracy in the prediction of the temperature regions in flames [55].

The main disadvantage of the standard $k-\epsilon$ model is that the effects of severe streamline bending due to swirl are unconsidered. Launder [88, 89] proposed transport equations to solve the Reynolds stress which allows to account the effects of swirl in a more rigorous manner than standard $k-\epsilon$ model. Some numerical studies have shown capacity to predict in good agreement with measured data axial and tangential velocities, temperature and turbulent correlations and rms (root mean square) of fluctuating velocities. When rms of the fluctuating velocity components are compared with those obtained by the $k-\epsilon$ model, the results obtained by RSM are closest to the experimental data [96, 162, 169]. It indicates that RSM may be capable of predicting the correlations and the mean quantities of swirl flows with enough accuracy to model industrial applications [143].

Chapter 3

Pre and post processing methods

3.1 Solution verification in numerical simulations

Finite volume discretization is used to obtain a discrete approximation of Unsteady Reynolds Averaged Navier-Stokes equations for swirl flows. Due to this practice, there is a difference between a quantity simulated and the exact solution of governing equations; this is the called numerical error, δ_{num}. Also, the numerical error have an associated *standard uncertainty*, u_{num}, which corresponds conceptually to an estimate of the standard deviation, σ, of the parent distribution from which δ_{num} is a single realization. These two quantities, δ_{num} and u_{num}, are used to verify the numerical solution.

The objective of verification is to establish numerical accuracy, independent of the physical accuracy that is the subject of validation. In other words, the purpose of verification is to detect inaccuracies in numerical solution and provide

an estimate of error. The procedure to obtain an estimate of error is by means of systematic grid refinement. Grid refinement is no longer necessary once the solution satisfies the error level criterion. The most widely used method to obtain an error estimate is classical Richardson Extrapolation (RE) [120, 121]. RE is the most popular form of error estimation since the method requires solutions of the same problem on two meshes. The basic idea of Richardson extrapolation is to obtain an approximation of the leading term in the truncation error from suitably weighted solution on two meshes with different cell size. Although grid doubling (or halving) is often used with RE, it is not required [123], and the ratio of grid spacing may be any real number greater than 1.3.

Before to obtain estimate error, it must be ensured that iterative convergence is achieved. Otherwise, the incomplete iteration will pollute the uncertainty estimation. A residual drop of three orders of magnitude in properly normalized residuals for each equation solved over the entire computational domain is a commonly used criterion. For time-dependent simulations, iterative convergence at every time step should be checked.

3.1.1 Grid convergence index

The grid convergence index (GCI) is used to provide an error band on the grid convergence of the solution. The GCI is based upon a grid refinement error estimator derived from the theory of generalized Richardson Extrapolation [122]. The objective is to provide a measure of uncertainty of the grid convergence. The GCI is a measure of the percentage between the computed value and the value of

the asymptotic numerical value. It indicates how much the solution would change with a further refinement of the grid. A small value of GCI indicates that the computation is within the asymptotic range. Estimation of discretization error is as follows:

1. Mesh or grid size h is defined.

$$h = \left[\frac{1}{N_c} \sum_{i=1}^{N_c} (\Delta V_i) \right]^{1/3} \tag{3.1}$$

   where ΔV_i is the volume of the i^{th} cell, and N_c is the total number of cells used for the computations.

2. Three different set of grids are selected and simulations are run to determine the values of the variable ϕ. It is desirable that the grid refinement factor, $r = h_{coarse}/h_{fine}$, be greater than 1.3.

3. For $h_1 < h_2 < h_3$ and $r_{21} = h_2/h_1 = 2$, $r_{32} = h_3/h_2 = 2$, the apparent order, p, is calculated using the expression

$$p = \frac{1}{\ln(r_{21})} \left| \ln \left| \epsilon_{32}/\epsilon_{21} \right| + q(p) \right| \tag{3.2}$$

$$q = \ln \left(\frac{r_{21}^p - s}{r_{32}^p - s} \right) \tag{3.3}$$

$$s = 1 \cdot sign(\epsilon_{32}/\epsilon_{21}) \tag{3.4}$$

where $\epsilon_{32} = \phi_3 - \phi_2$, $\epsilon_{21} = \phi_2 - \phi_1$. Negative values of $\epsilon_{32}/\epsilon_{21} < 0$ are an indication of oscillatory convergence. It should be noted that if either $\epsilon_{32} = \phi_3 - \phi_2$ or $\epsilon_{21} = \phi_2 - \phi_1$ is "very close" to zero, the above procedure does not work. This might be an indication of oscillatory convergence or, in rare situations, it may indicate that the "exact" solution has been attained.

4. The extrapolated values are calculated from

$$\phi_{ext}^{21} = (r_{21}^p \phi_1 - \phi_2)/(r_{21}^p - 1) \tag{3.5}$$

5. The approximate relative error, extrapolated relative error and the fine grid convergence index, along with the apparent order p, are calculated.

$$e_a^{21} = \left| \frac{\phi_1 - \phi_2}{\phi_1} \right| \tag{3.6}$$

$$e_{ext}^{21} = \left| \frac{\phi_{ext}^{12} - \phi_1}{\phi_{ext}^{12}} \right| \tag{3.7}$$

$$GCI_{fine}^{21} = \frac{Fs \cdot e_a^{21}}{r_{21}^p - 1} \tag{3.8}$$

The relative error estimates and the GCI may use dimensional values instead of relative or normalized values. The Factor of Safety, Fs, originally was assigned a value of 3 for two-grid studies, but Roache [123] has recommended a less conservative value $Fs = 1.25$, but only when using at least solutions in three grids.

This procedure makes no distinction between steady state computations and time-dependent computations. The method is independent of temporal resolution in the sense that Δt does not appear in any of the equations. So, for time-dependent computations, the effect of the numerical time step Δt is evaluated for three values by means of the power spectral density (PSD) at a given node and applying the GCI procedure; the Δt is teated just like Δx is treated.

3.2 Spectral analysis

Spectral analysis is used to obtain information about the frequencies contained in a data set, to analyze the spectral components shared by several signals or to determine the transfer function of a system.

Classical spectra analysis generally uses fast Fourier transform (FFT) which is a common tool in practical applications. Actually, efficient computational algorithms are available and allow the implementation of FFT methods on signal processing. However, fast Fourier methods induce various difficulties, in part due to the assumptions made to improve the numerical efficiency. These difficulties affect the results by finite-length effects: a signal cannot be known during a infinite time. These effects may be attenuated by windowing the signal. Another problem

with Fourier transform spectral analysis relates to the compromise between the frequency resolution and statistical stability. The shorter is the sampling time, lower is the frequency resolution. Hence, statistical stability of the results may be achieved only by averaging a large number of periodograms (averaging of 100 periodograms or more is usual and enough).

3.2.1 Fast Fourier transform

The fast Fourier transform (FFT) is a recursive algorithm for evaluating the discrete Fourier transform and its inverse. Suppose that a physical process is represented by time function, $h(t)$. The function is sampled at N times, $t_k = k\Delta t$ where $k = 0, 1, 2, \ldots, N-1$. From these N measurements, h_k, N complex amplitudes, H_n, are determined which satisfy the N equations

$$H_n = \sum_{k=0}^{N-1} h_k e^{ik\frac{2\pi n}{N}} \tag{3.9}$$

The sampled function then has the discrete Fourier expansion

$$h_k = \frac{1}{N} \sum_{n=0}^{N-1} H_n e^{-in\frac{2\pi k}{N}} \tag{3.10}$$

This equation can be reduced in familiar form with $2\pi k/N = (2\pi/T_o)\, k\, (T_o/N) = \omega_o k\Delta t = \omega_o t_k$

$$h_k = \frac{1}{N} \sum_{n=0}^{N-1} H_n e^{-in\omega_o t_k} \tag{3.11}$$

The right-hand side is the discrete analogue to the complex form of the Fourier expansion

$$h(t) = \sum_{n=-\infty}^{\infty} c_n e^{in\omega_o t} \tag{3.12}$$

where the complex coefficients, c_n, are given by

$$c_n = \frac{1}{T_o} \int_0^{T_o} h(t) e^{-in\omega_o t} dt \tag{3.13}$$

Now, if W is defined as a complex number

$$W \equiv e^{2\pi i/N} \tag{3.14}$$

Then Eq. 3.9 can be written as

$$H_n = \sum_{k=0}^{N-1} W^{nk} h_k \tag{3.15}$$

In other words, the vector of $h_k's$ is multiplied by a matrix whose (n,k)th element is the constant W to the power $n \times k$. The matrix multiplication produces a vector result whose components are the $H_n's$. This matrix multiplication evidently requires N^2 complex multiplications, plus a smaller number of operations to generate the required powers of W. So, the discrete Fourier transform appears to be an $O(N^2)$ process. The discrete Fourier transform can, in fact, be computed in $O(N \log_2 N)$ operations with an algorithm called the *fast Fourier transform*. The

difference between $N \log_2 N$ and N^2 is immense.

Danielson and Lanczos [29] provided one of the clearest derivation of the algorithm. They showed that a discrete Fourier transform of length N can be rewritten as the sum of two discrete Fourier transforms, each of length $N/2$. One of the two is formed from the even-numbered points of the original N, the other from the odd-numbered points. The proof is simply this:

$$\begin{aligned} F_k &= \sum_{j=0}^{N-1} e^{2\pi ijk/N} f_j \\ &= \sum_{j=0}^{N/2-1} e^{2\pi ik(2j)/N} f_{2j} + \sum_{j=0}^{N/2-1} e^{2\pi ik(2j+1)/N} f_{2j+1} \\ &= \sum_{j=0}^{N/2-1} e^{2\pi ikj/(N/2)} f_{2j} + W^k \sum_{j=0}^{N/2-1} e^{2\pi ikj/N(N/2)} f_{2j+1} \\ &= F_k^e + W^k F_k^o \end{aligned} \tag{3.16}$$

In last line, W is the same complex constant as in Eq. 3.14, F_k^e denotes the kth component of the Fourier transform of length $N/2$ formed from the even components of the original $f_j's$, while F_k^o is the corresponding transform of length $N/2$ formed from the odd components. Notice also that k in the last line of Eq. 3.16 varies from 0 to N, not just to $N/2$. Nevertheless, the transforms F_k^e and F_k^o are periodic in k with length $N/2$. So each is repeated through two cycles to obtain F_k.

This procedure can be used recursively. Having reduced the problem of

computing F_k to that of computing F_k^e and F_k^o. So, the same reduction of F_k^e to the problem of computing the transform of *its* $N/4$ even-numbered input data and $N/4$ odd-numbered data. In other words, its is possible define F_k^{ee} and F_k^{eo} to be the discrete Fourier transforms of the points that are respectively even-even and even-odd on the successive subdivisions of the data.

3.3 Proper orthogonal decomposition: POD

3.3.1 Basics

Numerical simulations generate a very large amount of data. There is therefore a great need to have specific postprocessing techniques able to extract from these large quantities of high-dimensional data, synthetic information essential to understand and eventually to model the processes under study. The proper orthogonal decomposition (POD) is one of the most powerful method of data analysis for multivariate and non linear phenomena. Essentially, POD is a linear procedure that takes a given collection of input data and creates an orthogonal basis constituted by functions estimated as the solutions of an integral eigenvalue problem known as Fredholm equation. These eigenfunctions are by definition characteristic of the most probable realization of the input data. Moreover, it can be shown that they are optimal in terms of representation of the energy present within the data.

The POD was introduced in the context of turbulence by Lumley [102] as an objective definition of what previously was called ’ big eddies’ by Townsend [155]

and which is now widely known as coherent structures. According to Lumley [103], the POD is a natural idea to replace the usual Fourier decomposition in nonhomogeneous directions. The POD method was introduced for different purposes independently by several scientists. The POD has been used widely in studies of turbulence but other popular applications involve random variables, image processing such as characterization of human faces, signal analysis, data compression, and more recently optimal control.

From a mathematical point of view, the proper orthogonal decomposition is just a transformation that diagonalizes a given matrix A and brings it to a canonical form $A = F \sum G^{\dagger}$ where $\sum$ is a diagonal matrix. The mathematical content of POD is therefore classical and is based on the spectral theory of compact, self-adjoint operators. Two geometric interpretations of this mathematical procedure are discussed later.

The coherent structures identification has to be done for at least two reasons: firstly, from an energetic point of view because the relative energy content of the CS compared with the total turbulent energy can be from 10% (for boundary layers, far jets) up to 20% (far wakes, plane mixing layers) or 25% (near wakes or jets); secondly, because the dynamical properties of CS play an essential role in mixing processes, drag, noise emission, etc. For these reasons, the idea of controlling turbulent flows by means of influencing their coherent structures seems promising.

Several characteristics of the proper orthogonal decomposition technique, as introduced by Lumley [102], are quite attractive in terms of CS identification. Firstly, compared to many other classical methods used for large-scale identifica-

tion (flow visualization, conditional methods, variable integration time average, pattern recognition analysis), no a priori is needed for the eduction scheme. CS are defined in an objective and unique manner as the flow realization that possesses the largest projection onto the flow field. Secondly, the POD yields an optimal set of basis functions in the sense that no other decomposition of the same order captures an equivalent amount of kinetic energy. Up to now, POD is only presented as a data analysis method that takes as input an ensemble of data, obtained from physical experiments of from detailed numerical simulations, and extracts basis functions optimal in terms of the representativeness of the data. POD can also be used as an efficient procedure to compute low-dimensional dynamical models of the CS.

Due to the optimality of convergence in terms of kinetic energy of the POD functions, only a small number of POD modes are necessary to represent the dynamical evolution of the flow correctly.

3.3.2 POD approximation method

Suppose a vector-valued function $u(\mathbf{x}, t)$ over some domain of interest Ω_s. It can be approximate as a finite sum in the separated-variable form:

$$u(\mathbf{x}, t) \simeq \sum_{k=1}^{K} a^{(k)}(t)\phi^{(k)}(\mathbf{x}) \tag{3.17}$$

$\mathbf{x}$ can be viewed as a spatial coordinate and t as a temporal coordinate.

A classic way to solve this approximation problem is to use for the basis

functions $\phi^k(\mathbf{x})$, functions given a priori, for example Fourier series, Legendre polynomials of Chebyshev polynomials. An alternative approach could be to determine the functions $\phi^k(\mathbf{x})$ that are naturally intrinsic for the approximation of the function $u(\mathbf{x}, t)$.

An additional difficulty is that a different sequence of time functions $a^{(k)}(t)$ corresponds to each choice of basic functions $\phi^k(\mathbf{x})$. So, given $\phi^k(\mathbf{x})$, the coefficients $a^{(k)}(t)$ can be determined as follows. Suppose we have chosen orthonormal basis functions, i. e.,

$$\int_{\Omega_s} \phi^{(k_1)}(\mathbf{x})\phi^{(k_2)}(\mathbf{x})d(\mathbf{x}) = \delta_{k_1 k_2} \tag{3.18}$$

where

$$\delta_{k_1 k_2} = \begin{cases} 0 & \text{for } k_1 \neq k_2 \\ 1 & \text{for } k_1 = k_2 \end{cases} \tag{3.19}$$

is the Kronecker delta symbol, then:

$$a^{(k)}(t) = \int_{\Omega_s} u(\mathbf{x}, t)\phi^{(k)}(\mathbf{x})d\mathbf{x} \tag{3.20}$$

Therefore for orthonormal basis functions, $a^{(k)}(t)$ depends only on $\phi^{(k)}(\mathbf{x})$ and not on the other ϕ. So far selecting the function $\phi^{(k)}(\mathbf{x})$, it would be useful to use the orthonormality condition.

Now consider experimental or numerical data at N_t different instants of time, M realizations of $u(\mathbf{x}, t)$ at M different locations x_1, x_2, ..., x_M. The

approximation problem of Eq. 3.17 is then equivalent to finding the orthonormal functions $\left\{\phi^{(k)}(\mathbf{x})\right\}_{k=1}^{K}$ with $K \leq N_t$ that solve:

$$\min \sum_{i=1}^{N_t} \left\| u(\mathbf{x}, t_i) - \sum_{k=1}^{K} \left[u(\mathbf{x}, t_i), \phi^{(k)}(\mathbf{x}) \right] \right\|_2^2 \tag{3.21}$$

where $\|\cdot\|_2$ define the norm associated with the usual L^2 inner product $(.,.)$. The practical method of solving the minimization problem of Eq. 3.21 is to arrange the data set $\mathcal{U} = \{u(\mathbf{x}, t_i), \ldots, u(\mathbf{x}, t_{N_t})\}$ in an $M \times N_t$ matrix A called the snapshot data matrix

$$A = \begin{pmatrix} u(x_1,t_1) & u(x_1,t_2) & \cdots & u(x_1,t_{N_t}) \\ u(x_2,t_1) & u(x_2,t_2) & \cdots & u(x_2,t_{N_t}) \\ \vdots & \vdots & \vdots & \vdots \\ u(x_M,t_1) & u(x_M,t_2) & \cdots & u(x_M,t_{N_t}) \end{pmatrix}, A \in \mathbb{R}^{M \times N_t} \tag{3.22}$$

Each column $A_{:,i} \in \mathbb{R}^M$ of the snapshot data matrix represents a single snapshot $u(\mathbf{x}, t_i)$ of the input ensemble $\mathcal{U}$. It is noted that, if the snapshot data are assumed to be linearly independent, the snapshot matrix has full column rank.

3.3.3 POD applied to turbulent flows

Based on previous and basic analysis. Let $\{\mathbf{u}(\mathbf{X}), \mathbf{X} = (\mathbf{x}, t_n) \in \mathcal{D} = \mathbb{R}^3 \times \mathbb{R}^+\}$ denote the set of snapshots obtained at N_t different time steps t_n over a spatial

domain of interest Ω_s. These snapshots could be numerical solutions of velocity fields, vorticity fields, etc. taken at different time steps. The underlaying problem is to extract from this ensemble of random vector fields a coherent structure. Defining a coherent structure as *the deterministic function which is the best correlated on average with the realizations* ***u(X)***. In other words, a function $\mathbf{\Phi}$ that has the largest mean square projection onto the observations $|(\mathbf{u}, \mathbf{\Phi})|^2$ is looked for.

There are two methods to find $\mathbf{\Phi}$. One where the average $\langle\cdot\rangle$ is temporal and is evaluated as an ensemble average, based on the assumptions of stationarity and ergodicity. The variable $\mathbf{X}$ is assimilated to the space variable $\mathbf{x} = (x, y, z)$ defined over the domain Ω_s. This is the direct method or classical POD.

The other method is the so-called snapshot POD method which is the exact symmetry of the classical POD. The average operator $\langle\cdot\rangle$ is evaluated as a space average over the domain Ω_s. The snapshots are taken at different times. The time step is usually constant but this is not necessary. The only requirement is that the snapshots are linearly independent. This method is efficient when the spatial domain is higher than the number of observations.

Each method has particular characteristics but it is relatively easy to choose the pertinent method for each practical configuration. For example, on the one hand, data obtained by numerical simulations can be highly resolved in space and time but due to cost considerations only a very short time sample is simulated. Conversely, a good spatial resolution can be obtained by particle image velocimetry, but associated with a poor temporal resolution.

On the other hand, experimental approaches such as hot-wire anemometry

or laser Doppler anemometry provide a well-defined time description but with limited spatial resolution. These measurement techniques enabled long time histories and moderate spatial resolution.

Data issued form an experimental approach will generally be treated using the classical method and data issued from numerical simulations by the snapshots method. An exception is the case of data sets obtained from particle image velocimetry.

3.3.4 Snapshot POD

To derive the discrete eigenvalue problem corresponding to the snapshot POD, it is assumed that $\mathbf{\Phi}$ has a special form in terms of the original data

$$\mathbf{\Phi}(\mathbf{x}) = \sum_{k=1}^{N_t} a(t_k)\mathbf{u}(\mathbf{x}, t_k) \tag{3.23}$$

where the coefficients $a(t_k)$, $k = 1, \ldots, N_t$ are to be determined solving the Fredholm integral eigenvalue problem

$$\int_{\Omega_s} R(x, x')\mathbf{\Phi}(x')dx' = \lambda\mathbf{\Phi}(\mathbf{x}) \tag{3.24}$$

The two-point spatial correlation tensor $R(x, x')$ is estimated under stationary and ergodicity assumptions as:

$$\begin{aligned} R(x,x') &= \frac{1}{T}\int_T \mathbf{u}(\mathbf{x},t)\otimes\mathbf{u}^*(\mathbf{x}',t)dt \\ &= \frac{1}{N_T}\sum_{i=1}^{N_t}\mathbf{u}(\mathbf{x},t_i)\otimes\mathbf{u}^*(\mathbf{x}',t_i) \end{aligned} \tag{3.25}$$

Substituting this expression of R and the decomposition of $\mathbf{\Phi}$ (Eq. 3.23) into Equation 3.24

$$\begin{aligned} \sum_{i=1}^{N_t}\left[\sum_{k=1}^{N_t}\frac{1}{N_t}\left(\int_{\Omega_s}\mathbf{u}(\mathbf{x}',t_k)\cdot\mathbf{u}^*(\mathbf{x}',t_i)d\mathbf{x}'\right)a(t_k)\right]\times\mathbf{u}(\mathbf{x},t_i) \\ = \lambda\sum_{k=1}^{N_t}a(t_k)\mathbf{u}(\mathbf{x},t_k) \end{aligned} \tag{3.26}$$

and concluding that a sufficient condition for the coefficients $a(t_k)$ to be a solution of Equation 3.24 is to verify that

$$\begin{aligned} \sum_{k=1}^{N_t}\frac{1}{N_t}\left[\mathbf{u}(\mathbf{x}',t_k)\cdot\mathbf{u}^*(\mathbf{x}',t_i)\right]a(t_k) = \lambda a(t_i), \\ i=1,\ldots,N_t. \end{aligned} \tag{3.27}$$

This can be rewritten as the eigenvalue problem

$$C\mathbf{V} = \lambda\mathbf{V} \tag{3.28}$$

where

$$C = \frac{1}{N_t} \int_{\Omega_s} \mathbf{u}(\mathbf{x}', t_k) \cdot \mathbf{u}^*(\mathbf{x}', t_i) d\mathbf{x} \tag{3.29}$$

and

$$\mathbf{V} = [a(t_1), a(t_2), \ldots, a(t_{N_t})]^T \tag{3.30}$$

Since C is a nonnegative Hermitian matrix, it has a complete set of orthogonal eigenvectors

$$\begin{aligned} \mathbf{V}^{(1)} &= \left[a^{(1)}(t_1), a^{(1)}(t_2), \ldots, a^{(1)}(t_{Nt})\right]^T, \\ \mathbf{V}^{(2)} &= \left[a^{(2)}(t_1), a^{(1)}(t_2), \ldots, a^{(2)}(t_{Nt})\right]^T, \ldots, \\ \mathbf{V}^{(N_t)} &= \left[a^{(N_t)}(t_1), a^{(N_t)}(t_2), \ldots, a^{(N_t)}(t_{Nt})\right]^T \end{aligned} \tag{3.31}$$

along with a set of eigenvalues $\lambda^{(1)} \geq \lambda^{(2)} \geq \ldots \geq \lambda^{(N_t)} \geq 0$. Then, the temporal eigenfunctions $\mathbf{V}^i$ can be normalized by requiring that

$$\begin{aligned} \frac{1}{N_t}(\mathbf{V}^n, \mathbf{V}^m) = &\quad \frac{1}{N_t} \sum_{k=1}^{N_t} a^{(n)}(t_k) a^{(m)*}(t_k) \\ = &\quad \lambda^{(n)} \delta_{nm} \end{aligned} \tag{3.32}$$

Then, the POD eigenfunctions $\mathbf{\Phi}^{(n)}(\mathbf{x})$ are estimated as

$$\mathbf{\Phi}^{(n)}(\mathbf{x}) = \frac{1}{N_t \lambda^{(n)}} \sum_{k=1}^{N_t} a^{(n)}(t_k)\mathbf{u}(\mathbf{x}, t_k) \tag{3.33}$$

3.4 Vortex definition

Vortices are a special existence form of fluid motion with origin in the rotation of fluid elements. It can be possible to recognize the existence of vortices first by their intuitive streamline patterns, which are however not Galilean invariant and cannot be used to define a vortex. A natural invariant approach could be based on the vorticity, from which one can extract vorticity lines and vorticity magnitude. Saffman and Baker [128] defined a vortex as a connected fluid region with high concentration of vorticity compared with its surrounding. In other words, a vortex is a vorticity tube surrounded by irrotational flow. But the vortex boundary becomes fuzzy in viscous flow without sharp boundary. There are a some cases where vortices are axisymmetric of which the outer boundary, of radius r_o, has the maximum value of the circumferential velocity. However, this criterion cannot be generalized to more complex and nonaxisymmetric vortices.

A simple alternative to the vortex definition would be identifying the fluid region with $|\omega| \geq |\omega_0|$, where $|\omega_0|$ is a threshold magnitude. But this criterion is also inadequate because the choice of $|\omega_0|$ is subjective, and the side boundary of a vorticity tube may significantly differ from an isovorticity surface.

A natural basis for developing possible rational criteria is the symmetric-antisymmetric decomposition of the velocity gradient tensor, $\nabla\mathbf{u}$, $\nabla\mathbf{u} = \mathbf{D} + \mathbf{\Omega}$, which suggests that a vortex may be defined as a flow region where the

vorticity (symmetric tensor Omega) prevails over the strain rate (symmetric tensor Omega). This requires the calculation of the invariants of the velocity gradient tensor through its representative matrix, say $\mathbf{A}_\lambda$; which in cylindrical coordinates reads

$$\mathbf{A}_\lambda = \begin{pmatrix} u_{,r} & v_{,r} & w_{,r} \\ (u_{,\theta} - v)/r & (u_{,\theta} + u)/r & w_{,\theta}/r \\ u_{,z} & v_{,z} & w_{,z} \end{pmatrix}, \tag{3.34}$$

where subscript $_{,r}$ is the partial derivate with respect to radius, $_{,\theta}$ is partial derivate with respect to angular coordinate and $_{,z}$ is partial derivate with respect to axial coordinate.

The first criterion along this line was proposed by Weiss for two dimensional incompressible flow ($u,\ v$) based on the eigenvalues σ of $\nabla\mathbf{u}$, of which the characteristic equation is

$$\sigma^2 + Q_{2D} = 0 \tag{3.35}$$

where

$$Q_{2D} = \begin{vmatrix} u_{,x} & v_{,x} \\ u_{,y} & v_{,y} \end{vmatrix} = \frac{1}{2}(\|\mathbf{\Omega}\|^2 - \|\mathbf{D}\|^2) = \frac{1}{4}\omega^2 - \frac{1}{2}\|\mathbf{D}\|^2 \tag{3.36}$$

is the second invariant of $\nabla\mathbf{u}$ (and also the negative of the discriminant Δ_{2D}; the first invariant is tr($\nabla\mathbf{u}$)=0). Here, it is considered $\|\mathbf{S}\| \equiv \left[\text{tr}(\mathbf{S}\cdot\mathbf{S}^T)\right]^{1/2}$ for any tensor $\mathbf{S}$. When Q_{2D} >0 at a point, the flow is called *elliptic* and we have

purely imaginary eigenvalues $\pm i\sigma_i = \pm\sqrt{Q_{2D}}$; for the case of Q_{2D} <0 the flow is called *hyperbolic*. Thus, a vortex is defined as a connected fluid region with

$$Q_{2D} = -\Delta_{2D} = \sigma_i^2 > 0 \tag{3.37}$$

known as the *Weiss criterion*. In particular, if instead of Cartesian we use cylindrical r-phi coordinates (Eq. 3.34 in 2D), for a 2D vortex, there is

$$Q_{2D} = \frac{1}{4}\left\{\left[\frac{1}{r}\frac{\partial}{\partial r}(rv)\right]^2 - \left[r\frac{\partial}{\partial r}\left(\frac{v}{r}\right)\right]^2\right\} = \frac{v}{r}\frac{\partial v}{\partial r} \tag{3.38}$$

and $\sigma_i^2 > 0$ precisely defines the vortex as a fluid within $r = r_0$ where $v = \max$, in consistency with the common concept of vortex core.

Controversy on defining a vortex appears once three-dimensional flow is considered. The characteristic equation for the eigenvalues of $\nabla\mathbf{u}$ is

$$\sigma^3 + Q\sigma - R = 0 \tag{3.39}$$

where

$$\begin{aligned} Q \equiv -\frac{1}{2}u_{i,j}u_{j,i} = \frac{1}{2}(\|\mathbf{\Omega}\|^2 - \|\mathbf{D}\|^2) \\ = \frac{1}{2}\left(\frac{1}{2}\omega^2 - \|\mathbf{D}\|^2\right) = \sigma_1\sigma_2 + \sigma_1\sigma_3 + \sigma_2\sigma_3, \end{aligned} \tag{3.40}$$

$$R \equiv \det(u_{i,j}) = \frac{1}{3} u_{i,j} u_{j,k} u_{k,i} \\ = \frac{1}{3}(D_{ij} D_{ji} D_{ki} + 3 D_{ij} \Omega_{jk} \Omega_{ki}) = \sigma_1 \sigma_2 \sigma_3 \tag{3.41}$$

are the second and third invariants of $\nabla \mathbf{u}$, respectively. The discriminant of Eq. 3.39 is

$$\Delta = \left(\frac{Q}{3}\right)^3 + \left(\frac{R}{2}\right)^2 \tag{3.42}$$

Consequently, in three dimensions the question on how much the vorticity should prevail over the strain rate may have two possible answers, both being within kinematics: either

$$\Delta > 0 \tag{3.43}$$

or

$$Q > 0 \tag{3.44}$$

These are known as the Δ-*criterion*, Dallman, Chong et al., and Q-*criterion*, respectively. The Q-criterion can be equally expressed in terms of the *kinematic vorticity number* m introduced by Truesdell in both two and three dimensions:

$$m \equiv \frac{\|\mathbf{\Omega}\|}{\|\mathbf{D}\|} = \frac{\omega}{\sqrt{2}\,\|\mathbf{D}\|} > 1 \tag{3.45}$$

Moreover, in some complicated vortices, it has been observed how the centrifugal acceleration is balanced by the radial pressure gradient. In other words, the pressure is minimum at the vortex center. This property has also been considered as a dynamic criterion for defining at least a class of low-pressure vortices.

3.4.1 λ_2-criteria

Jeong and Hussain [80] proposed that the vorticity-induced pressure is sectionally minimum in a vortex. With this, they assure the low-pressure feature in an axial vortex in addition to the low-pressure condition ($Q > 0$). They start from the gradient of the incompressible Navier-Stokes equation

$$a_{j,i} = -\frac{1}{\rho}p_{,ij} + \nu u_{j,ikk} \tag{3.46}$$

where $a_{j,i}$ can be decomposed into symmetric and antisymmetric parts

$$a_{j,i} = \left(\frac{\mathrm{D}}{\mathrm{D}t}D_{ij} + \Omega_{ik}\Omega_{kj} + D_{ik}D_{kj}\right) + \left(\frac{\mathrm{D}}{\mathrm{D}t}\Omega_{ij} + \Omega_{ik}D_{kj} + D_{ik}\Omega_{kj}\right). \tag{3.47}$$

While the antisymmetric part just leads to the vorticity transport equation, the symmetric part yields

$$-\frac{1}{\rho}p_{,ij} = \frac{\mathrm{D}}{\mathrm{D}t}D_{ij} - \nu D_{ij,kk} + \Omega_{ik}\Omega_{kj} + D_{ik}D_{kj}. \tag{3.48}$$

In a plane the local pressure reaches a minimum at a point if the tangent

gradient of p vanishes there, and the second-order derivatives along two orthogonal tangent directions are both positive. Since $p_{,ij}$ is a symmetric tensor, the objective choice of the plane can be made in a principal-axis coordinate systems, where the plane is spanned by the two eigenvectors of $p_{,ij}$ and for p to be minimum the associated two eigenvalues must be both positive (the third eigenvalue is the smallest). The eigenvalues of $p_{,ij}$ can be found from the right-hand side of Eq. 3.48, but for picking up the vorticity-induced $p_{\min}$ the effect of the material derivate of D_{ij} (invariant following a fluid element) and its viscous diffusion should be excluded. Thus, the problem amounts to the real eigenvalues $\lambda_1 \geq \lambda_2 \geq \lambda_3$ of the symmetric tensor

$$\mathbf{G} \equiv \mathbf{D} \cdot \mathbf{D}^{\mathrm{T}} - \mathbf{\Omega} \cdot \mathbf{\Omega}^{\mathrm{T}}, \tag{3.49}$$

and the sectional pressure-minimum induced by a vortex is ensured by requiring the second eigenvalue of $\mathbf{G}$ be negative:

$$\lambda_2 < 0. \tag{3.50}$$

This is known as the λ_2-criterion.

Extensive numerical tests of the above three-dimensional invariant criteria have been conducted by many authors (e.g. Jeong and Hussain [80];) for various vortices, including exact isolated vortex solutions and complex turbulent coherent vortices. These authors reported that, roughly speaking, the Δ-criterion sometimes covers too much vortical flow region; the Q- and λ_2-criteria educe quite similar vortex plots in most tested cases, but the former may miss a part of the

vortex; the λ_2-isosurfaces cannot always capture the pressure minimum and also sometimes cover too much space to visualize the coherent vortex structure neatly, while in some other cases it may cut a connected vortex into segments as well. No commonly agreed conclusion has been reached.

Chapter 4

URANS of a turbulent confined swirling burner

4.1 Problem definition, geometry, mesh and numerical method

In this Chapter, as a first step to a comprehensive performance prediction, we study URANS schemes for the simulation of isothermal, single-phase flow in a burner of pulverized solids. The geometry of swirl generation is completely realistic, comprising a tangential inlet for primary air (fuel transport) and movable guide vanes for secondary air. To model turbulence, two different schemes are used: second order closure by a Reynolds Stresses Model (RSM) and the $k-\epsilon$ model. In both cases, the model is kept intentionally simple, with no modifications over the standard version. We take special concern in assuring a grid-independent solution, by

studying the convergence of average magnitudes, and also the characteristics of the oscillations numerically reproduced. The upstream placement of fluid inlets, which is relevant both for the real equipment and the economy of the calculation, turns out to have a pronounced effect on the oscillations, and then on the mean flow; the effect is documented at length.

4.1.1 Modeled equipment and flow conditions

We attempt to simulate the flow in an experimental combustor of $500\ kW$ rated thermal input. Figure 4.1 shows details of the geometry. The combustion chamber has a diameter of $0.990\ m$ and a length of $1.512\ m$. Primary air is swirled by a tangential inlet and then flows through an annular duct of diameters $d_i = 0.054\ m$ and $d_o = 0.107\ m$. The inner pipe accommodates the ignitor and is closed for our conditions. Secondary air is fed to a drum-shaped settling chamber (the "windbox") and flows through a moveable-vane swirler. There are 10 vanes; its angle in nominal conditions is $\phi = 52°$. An annular duct of diameters $D_i = 0.113\ m$ and $D_o = 0.175\ m$ connects the swirler to the base of the burner throat.

Reynolds numbers based on hydraulic diameters of the annular ducts are $25,300$ and $47,000$ for primary and secondary air, respectively ($51,200$ and $81,100$ if based on the outer diameters). The geometric swirl numbers [64] are for primary air and for secondary air.

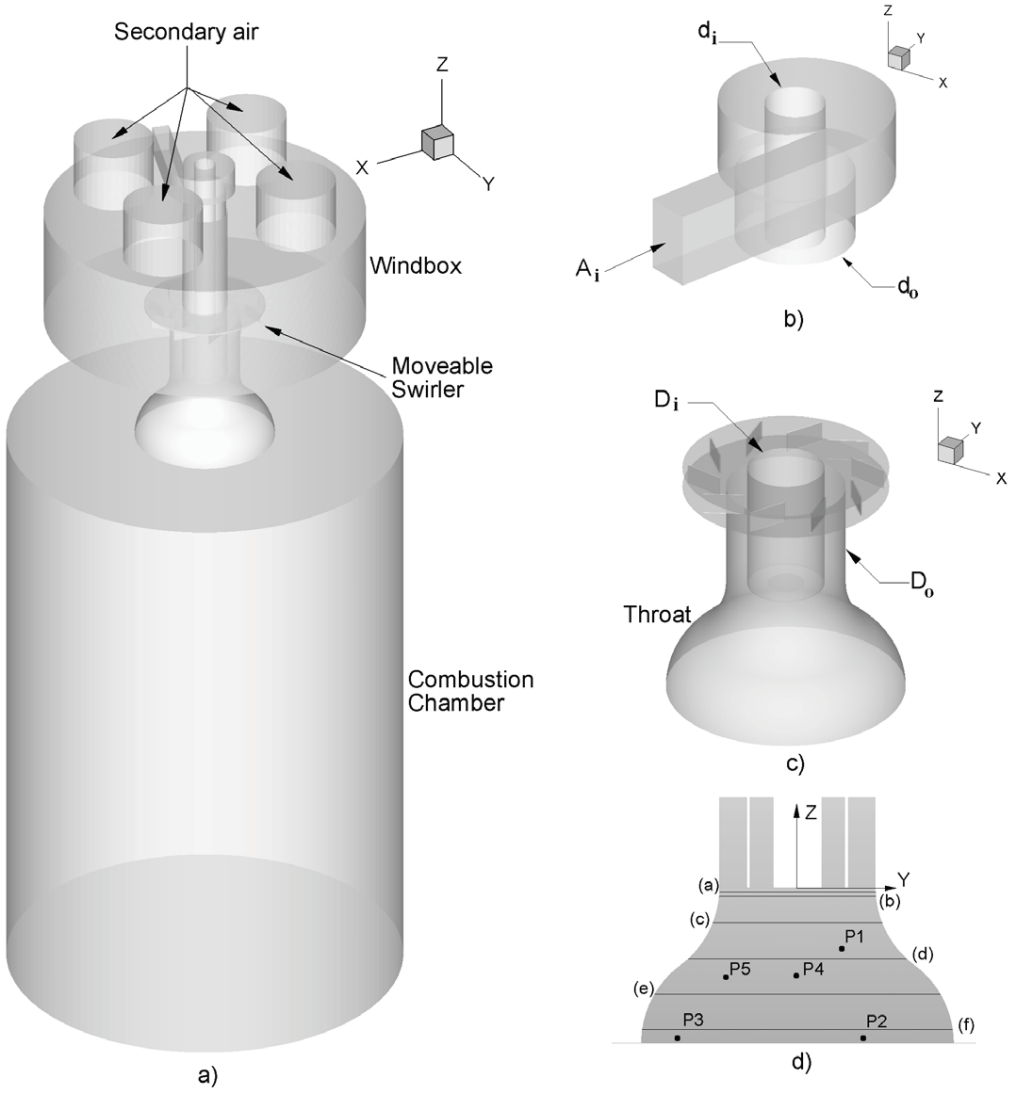

Figure 4.1: Geometry and computational domain. a) General view. b) Detail of primary air inlet. c) Detail of secondary swirler and throat. d) Origin of coordinates, random monitoring points and axial stations.

4.1.2 Physical models, boundary conditions and numerical methods

The incompressible unsteady Reynolds-averaged Navier-Stokes (URANS) equations are solved adopting two different closures for turbulence, the standard $k-\epsilon$ model [92] and a Reynolds stress model with linear pressure-strain term [58, 48, 88]. Wall reflection terms are included in the RSM, in order to consider pressure blocking and redistribution of normal stresses [28]. This was deemed necessary to adequately model wall-dominated regions, such as the spaces between the vanes of the secondary swirler.

Standard wall functions [92] are used for near-wall modeling. The first grid point is located at a maximum distance of $40 < y^+ < 60$ for all meshes.

Inflow conditions are idealized by assuming uniform velocity profiles at the inlet sections, $u_p = 15.11\ m/s$ and $u_s = 1.17\ m/s$ for primary and secondary air, respectively. Turbulence intensity is estimated from fully developed flow correlations as $I = 0.16Re^{-1/8}$ where Re is based on hydraulic diameter. Turbulence kinetic energy is then $k = 3/2(uI)^2$ and its dissipation rate for the $k-\epsilon$ model $\epsilon = C_\mu^{3/4}k^{2/3}l^{-1}$, with $C_\mu = 0.085$. Integral length scales are taken as $l_p = 0.05$ m and $l_s = 0.1$ m. For the RSM, inlet Reynolds stresses are determined under the assumption of isotropic turbulence, i.e., $\langle u'^2 \rangle = 2k/3$, $\langle u'v' \rangle = 0$.

Even for swirling flows, a high value of the Reynolds number normally permits to anticipate a small sensitivity to conditions at the outlet boundary (see e.g., Xia et al. [166]). In order to impose adequate conditions in the present simulations, we performed a brief far-field study. The usual expedient of zero axial velocity

gradients was imposed on three different geometries, each having a different chamber length of $7d_o$, $14d_o$ and $21d_o$, which corresponds to the real open end in isothermal air flow conditions ($14d_o$), and two imaginary open chambers, one shorter and one longer. Values at the exit plane did change slightly between the first and the second geometry, but they did not change appreciably between the second and the third. Accordingly, we extend the computational domain to a length of $14d_o$ downstream of the throat, and use the usual outflow conditions there.

Simulations are performed with the CFD solver FLUENT 6.3.26. We employ second order central differences for convection and diffusion terms and an implicit second-order scheme for the time derivatives. The SIMPLE algorithm is used as the pressure-velocity coupling method, taking care in adopting adequate time steps for the unsteady calculation [9].

4.1.3 Computational mesh

The computational domain is divided in three zones, corresponding to the volumes occupied by primary air, secondary air and combustion chamber. For reasons of convenience, the mesh is unstructured in the tangential inlet of primary air and in the windbox. The remaining zones (annular ducts, secondary air inlet zones and swirler, throat and combustion chamber) are represented by structured meshes.

For the study of grid independence, we used three progressively finer meshes. Following the recommendations of Celik et al. [21], a grid refinement factor greater than 1.3 was chosen to minimize truncation errors, specifically $r = 2$.

Thus, the medium and fine grids have respectively 8 and 64 times as many points as the coarse grid. Figures 4.2(d), (e) and (f) illustrate the geometric relationship. The number of computational nodes for the full geometry is, successively, $84,600$, $676,800$ and $5,414,400$.

4.1.4 Computational cases and numerical performance

Seven different computational cases were ran, as summarized in Table 4.1. Cases 1, 2 and 3 use the $k-\epsilon$ model in the coarse, medium and fine grids. They served to the grid independence study, based on recommended techniques from the literature, that were applied to the time-averaged flow (see 4.2). Additionally, variation of time-dependent features between the medium and fine grids were studied using RSM, cases 4 and 5 respectively. The main investigation then considered the medium grid for the comparison of URANS solutions under different turbulence models, cases 2 and 4. Aside from the "complete" geometry shown in Figure 4.2 (a), a simplified geometry that omits the windbox was considered relevant for the study. The reasons and the outcome are explained in Sect. 4. Simulations were repeated accordingly, cases 6 and 7.

The numerical computation doesn't converge in neither of these cases to a statistically stationary flow, but to oscillatory fields of velocity and pressure. When using the RSM, a representative time per global iteration is 5.19 s; it does not drop very much if the $k-\epsilon$ model is used instead: 3.03 s. However, the second order closure typically takes 28 iterations to converge in each time step, whereas the two-equation model only requires 6. In conclusion, times needed are approximately in

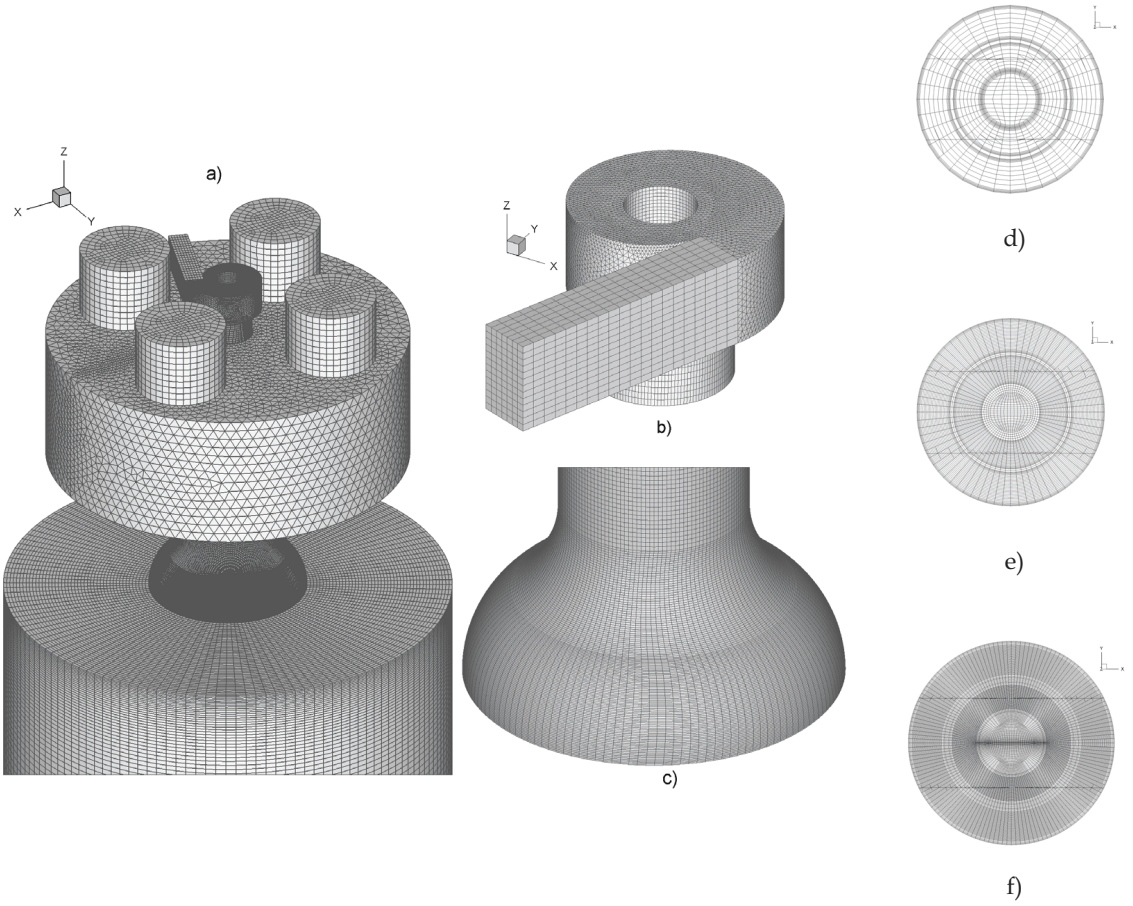

Figure 4.2: Details of the computational mesh: a) General view of the complete geometry. b) Details of primary air tangential inlet. c) Details of the expansion throat. Grid refinement: d) coarse, e) medium and f) fine grids.

Table 4.1: Summary of the computational cases

Run	Grid	Geometry	Turbulence model
1	Coarse	Complete	$k-\epsilon$
2	Medium	Complete	$k-\epsilon$
3	Fine	Complete	$k-\epsilon$
4	Medium	Complete	RSM
5	Fine	Complete	RSM
6	Medium	Without windbox	$k-\epsilon$
7	Medium	Without windbox	RSM

a proportion of six-fold. Time values refer to a Beowulf-type cluster using 6 CPUs of $2,200$ MHz.

4.2 Convergence and grid independence

We report in this section the studies undertaken to assure the quality of the numerical predictions. Basically, the computational procedure behaves well and converges within the preset tolerance to a solution that is independent of the initial conditions and the size of spatial and temporal increments. However, our case is very special in these respects, since we have an oscillatory flow. As a consequence, not only instantaneous or averaged values of flow magnitudes must be studied, but also their frequency content, for the range of frequencies that can be considered a genuine prediction of the URANS technique. This can be stated from a slightly different perspective. A numerical simulation with steady-state conditions is able to reproduce flow periodicities only by means of an initial amplification of numerical errors, which triggers the natural instability embedded in the flow

model, Ruith et al. [125]. Therefore, the converged solution must necessarily satisfy an additional condition, viz., that the oscillations behave independently of arbitrary initial values and grid size. Otherwise, it would be clear that a purely numerical artifact has been obtained, and no claim of representation of the real flow physics could be made.

4.2.1 Convergence of the oscillatory flow

Independence with respect to the initial condition is assured by repeating the same computational cases starting from widely different flow patterns. Two extreme possibilities are a stationary medium (nil velocity and pressure everywhere), and an artificial flow field purposely fabricated to shorten the transient period and speed up the convergence to the final solution. The first may represent a first approach to the real transient experienced by the physical system (although this is not of interest in this study). There are many possibilities for the second. For instance, aside from simply guessed fields, one can use solutions from simpler models in the same grid, or interpolated values from the solution in a coarser one.

Figure 4.3 shows as an example results from case 2 of Table 1. The magnitude represented is the modulus of velocity in the control point P1 of Figure 4.1(d). The fabricated flow field comes from a steady (RANS) solution obtained by using a first order scheme for spatial discretization. The attainment of a steady-periodic regime after an initial transient is clearly observed in both cases. We used in both a variable under-relaxation parameter, starting at a small value and increasing it gradually until the solution began to settle down to a stable oscillation. The

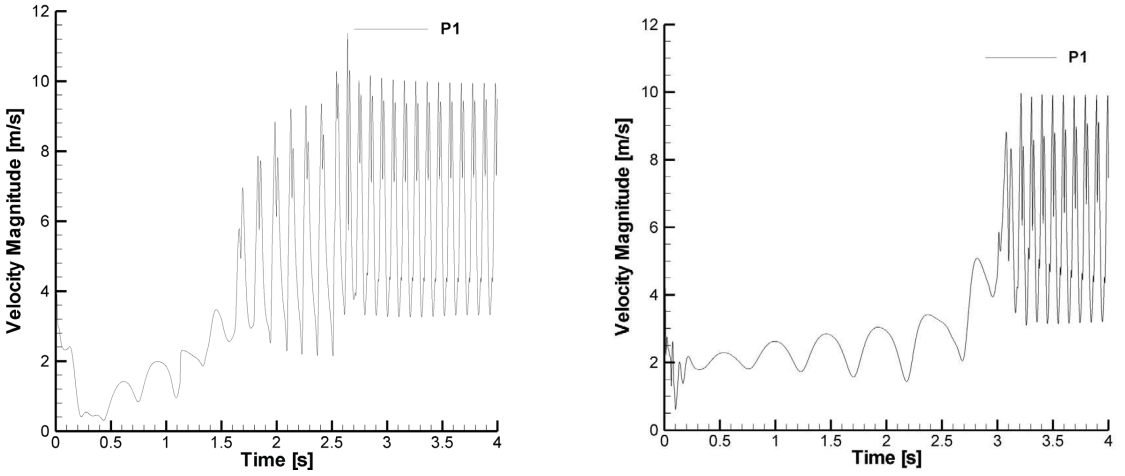

(a) (b)

Figure 4.3: Velocity magnitude at point P1, case 2. (a) Fabricated initial flow field. (b) Static initial conditions.

change is apparent at $2.5\ s$ in the fabricated flow case, Figure 4.3(a); the final oscillatory flow is attained approximately at this point. Logically, the transient is longer for an initially stationary fluid, Figure 4.3(b). As it is apparent in the figure, and can be demonstrated numerically, the two final solutions share the same average and extreme values, waveforms and frequency. (Phase needs not to be equal, for obvious reasons.)

A second consideration is that, since the frequency content predictable by the calculation is unknown beforehand, it is convenient to estimate the effect of the numerical time step Δt on the oscillations. We repeated selected test cases for three values, $\Delta t = 10^{-3}$, 5×10^{4} and $10^{-4}\ s$. Figure 4.4 shows the results for case 4, monitoring point P1, for the extreme values of t. Here we represent the power spectral density (PSD) of the velocity modulus vs. the Strouhal number based on

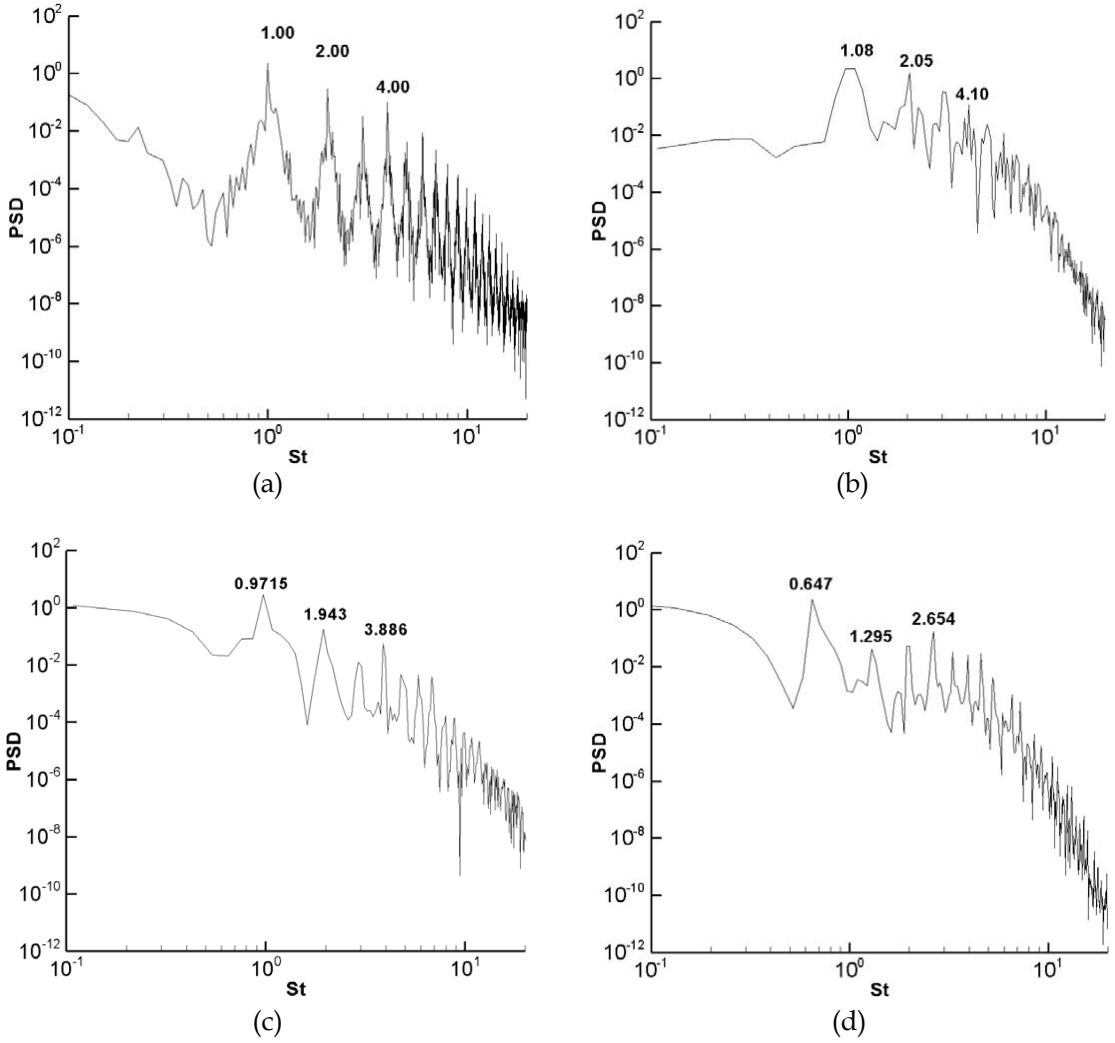

Figure 4.4: Fourier transform of the modulus of velocity at point P1, case 4 under different numerical time steps. (a) $\Delta t = 10^{-3}\ s$. (b) $\Delta t = 10^{-4}\ s$.

axial momentum and outlet diameter of the throat.

The URANS calculation produces distinct low frequency peaks, that can be related to coherent structures formed in the flow, as we will explain later. Tuned with these oscillations, also high frequency peaks are obtained, but with considerably less power (note the logarithmic ordinate), and entering into the inertial subrange of "background" turbulence, where fluctuations are supposedly modeled, so that they shouldn't convey any fundamental information. The decay exhibited at the right of the graph is just due to a Blackman window function used in the spectral analysis. The spectrum is logically much less noisy the lower the time step, but strength and location of the low frequency peaks only suffer minor variations. A value of $\Delta t = 10^{-3}$ s was used accordingly for the rest of the study.

4.2.2 Grid independence

To estimate the error of the numerical simulation, we use well-established procedures from the CFD literature, that involve repeating the calculation in three progressively finer grids, cases 1-3 of Table 1. Since the procedures only apply to steady-state situations, we firstly proceed as if they were also valid for our time-averaged flow. After finding out that the outcome is acceptable, we address separately the effect of grid size on the oscillations.

Figure 4.5 shows axial velocity profiles at six axial stations computed in the three grids. Differences are indeed small, and very similar flow patterns are predicted. In order to quantify the error, we follow the systematic procedure recommended by Celik et al. [21], or grid convergence index (GCI) method, that

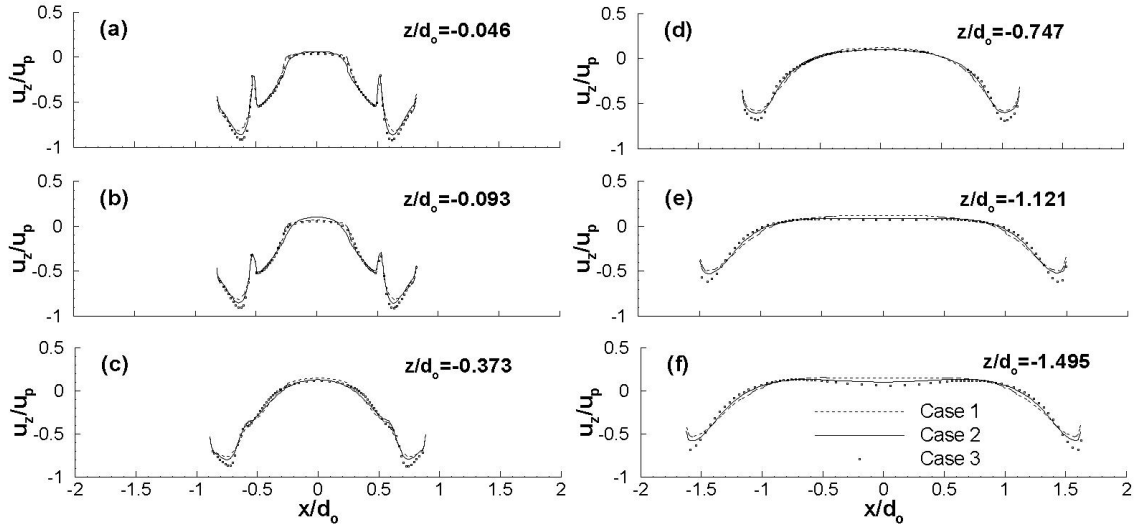

Figure 4.5: Time-averaged axial velocity at different axial locations (Fig. 4.1) for varying grid density.

is based on the Richardson extrapolation. Results at a couple of representative axial stations are as follows. At $z/d_o = -0.093$, the local apparent order of accuracy p ranges from 0.02 to 9.96 with an average of 5.64. The maximum discretization uncertainty is 8.14%, which corresponds to $\pm 0.615\ m/s$. At $z/d_o = -1.121$, p ranges from 0.015 to 8.75, with an average of 4.79 and a maximum discretization uncertainty of 9.67% ($\pm 0.73\ m/s$). Figure 4.6 represents the velocity profiles of the medium grid with the cor-responding local error bars drawn upon them.

The local apparent order of accuracy p ranges from 0.01 to 22.21 for the whole domain, with a volume average of 4.09. The maximum discretization error for the axial velocity is 37%; the average is 7.71% ($0.84 m/s$). Oscillatory convergence

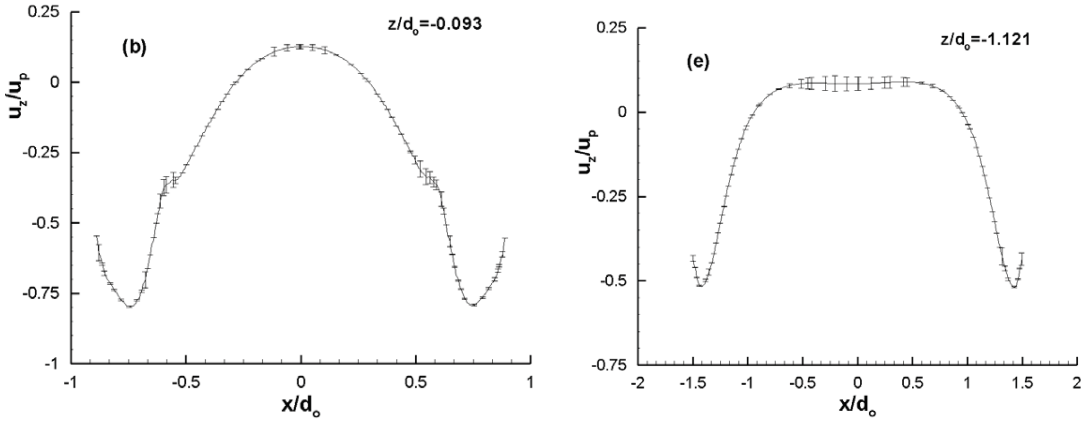

Figure 4.6: Discretization error in axial velocity at two axial positions.

occurs in 15% of total grid points. These figures indicate that computations of the time-averaged flow using the medium grid possess a reasonable numerical accuracy.

Concerning the oscillations, there is not a standardized procedure to quantify their spatial convergence. We adopt here the same expedient as above: to judge if the low-frequency part of the spectrum incorporates similar peaks. Figure 4.7 presents an example of the results using the medium grid (case 4) and the fine grid (case 5), for the same variable and control point as Figure 4.4. It is clear that the oscillations predicted only experience very slight changes in their strength and fundamental frequencies when grid size is reduced, and that the only effect is to attenuate the irrelevant high-frequency peaks.

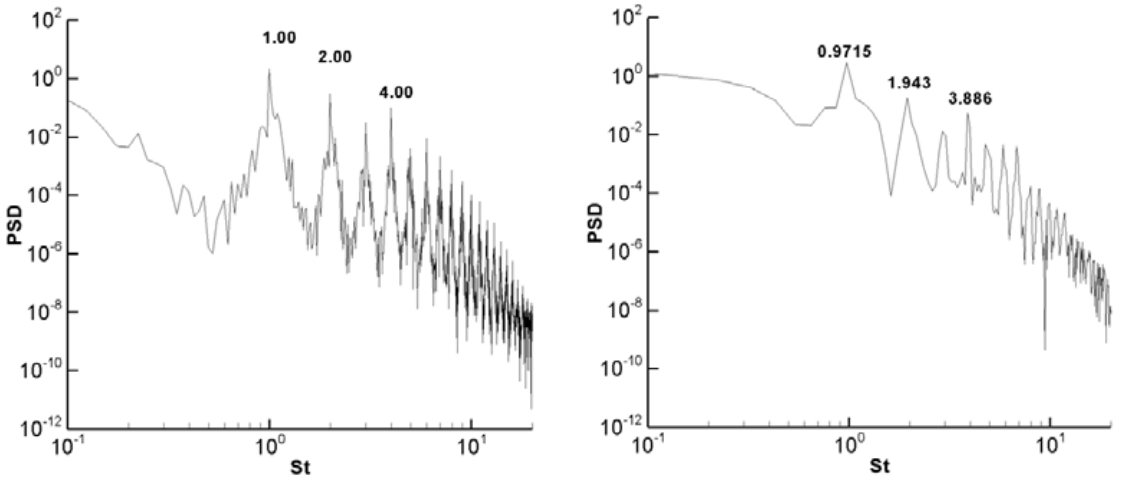

Figure 4.7: Fourier transform of the modulus of velocity at point P1 for varying grid density. (a) Medium grid, case 4. (b) Fine grid, case 5.

4.3 Influence of upstream placement

The settling chamber of the $0.5\ MWt$ pilot combustor ("windbox") has the purpose of providing as much uniformity as possible to the velocity profiles at the entrance of the secondary swirler. In a full-scale furnace, there are several burners of this class, in sizes that typically range from 12 to $60\ MWt$. A usual disposition of secondary air is then a large chamber that constitutes the windbox for all the burners located on one of the furnace walls. These two facts suggest that it could make sense to eliminate from the geometric domain the drums-haped windbox we see in Figures 4.1 and 4.2. In lieu of imposing known velocity conditions at the entrance of the four feeding pipes, the same mass flow can be allocated to the inlet surfaces of the swirler, if velocity profiles on them are uniform enough. This

obviously improves the economy of the calculation, but also makes the outcome of the simulation independent of the upstream disposition of air chambers, which is indeed interesting.

We examine in this section the feasibility of the idea, i.e., whether the main flow produced in the combustor is affected or not by the manner in which the secondary air entrance is simulated. Garcia-Villalba et al. [51] used a similar procedure for unconfined swirl flow. They claim that flow features, including turbulence statistics and coherent structures, are not affected, because the flow readily develops in the duct upstream of the jet exit.

In our case, to the simulations in the complete geometry already explained, cases 2 and 4 of Table 1, we add those in a geometry without windbox, cases 6 and 7 of Table 1. Geometry of the swirler is still represented, including the vanes and the upper cap. Inlet surfaces are now those located between consecutive vanes of the swirler, that lead the flow to the secondary annular duct, Figure 4.8. On them, we impose a uniform velocity whose normal (radial) component preserves the air flow. As for its direction, we rely on the results for the complete geometry (see below): no axial component, and a constant angle between radial and circumferential components given by the average on the surface. More economy would have resulted from eliminating completely the swirler and imposing conditions at its outlet. However, both velocity components are much more variable there, for obvious reasons, which would have demanded to arbitrarily fair their profiles. Constant values at swirler inlet are instead more universal and close to the real flow.

In principle, results from the complete geometry seem to warrant the

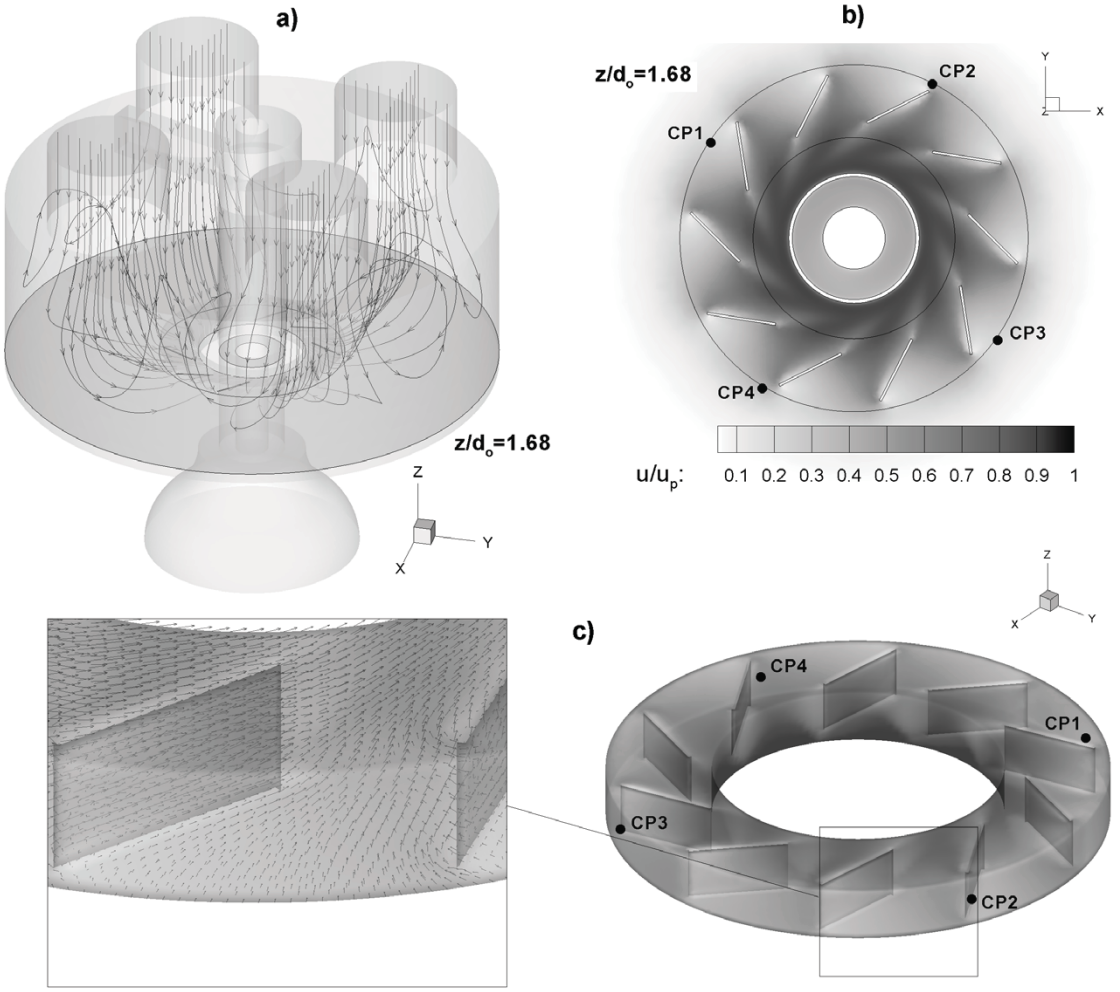

Figure 4.8: Time-averaged velocity field in the windbox and secondary swirler, case 2. (a) Streamlines (b) Contours of velocity modulus. (c) Detail of vector plot. Random control points CP1-CP4 at the inlet of the swirler are shown.

plausibility of this substitution. Figure 4.8 shows time-averaged flow patterns in the windbox and secondary swirler, as calculated by the $k-\epsilon$ model, case 2. The average was taken over 500 time steps of the steady-periodic flow, which corresponds to $0.5\ s$ of physical time. Flow is totally smooth, exhibiting an axisymmetric pattern with no regions of backflow and a good distribution of the secondary air.

However, this smoothness only represents the temporal average. Figure 4.9 shows time series in the four control points $CP1$-$CP4$ represented in Figure 4.8. The magnitude is the modulus of the velocity as calculated by the second order closure, case 4. Although of a small amplitude compared with oscillations in the main chamber, it is clear that velocity at the entrance of the swirler is also oscillatory. We can observe as well a superimposed long term variation, that is specially notorious for point $CP3$, but also present in the others. As we will see, this is a characteristic of the converged solutions obtained with the RSM. Other feature is that the phase of the oscillation seems to vary continuously around the periphery of the swirler, with points located radians apart ($CP1$-$CP3$, $CP2$-$CP4$) being in perfect opposition.

The effect of substituting these oscillations by constant values is documented by comparison of the solution for both geometries, complete and without windbox, in the monitoring point P1 (Figure 4.1). Turbulence is modeled by the RSM, cases 4 and 7 of Table 1. Figure 4.10 shows the time series and the power spectra. Both signals are spectrally quite similar, with a minor shift in the low frequency peaks. (Frequencies are also roughly the same as in points CP1-CP4, case 4, Figure 4.10). The time series shows however that the waveforms are widely different,

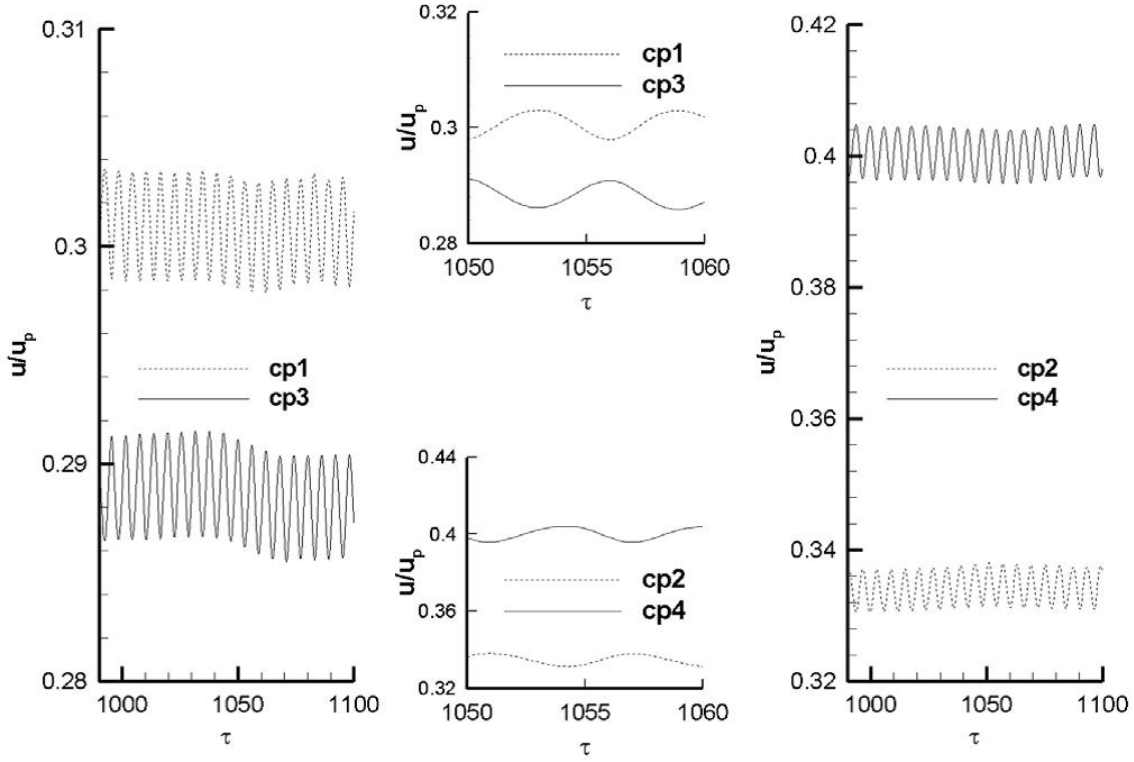

Figure 4.9: Time series of the modulus of velocity in the control points represented in Figure 4.8, case 4.

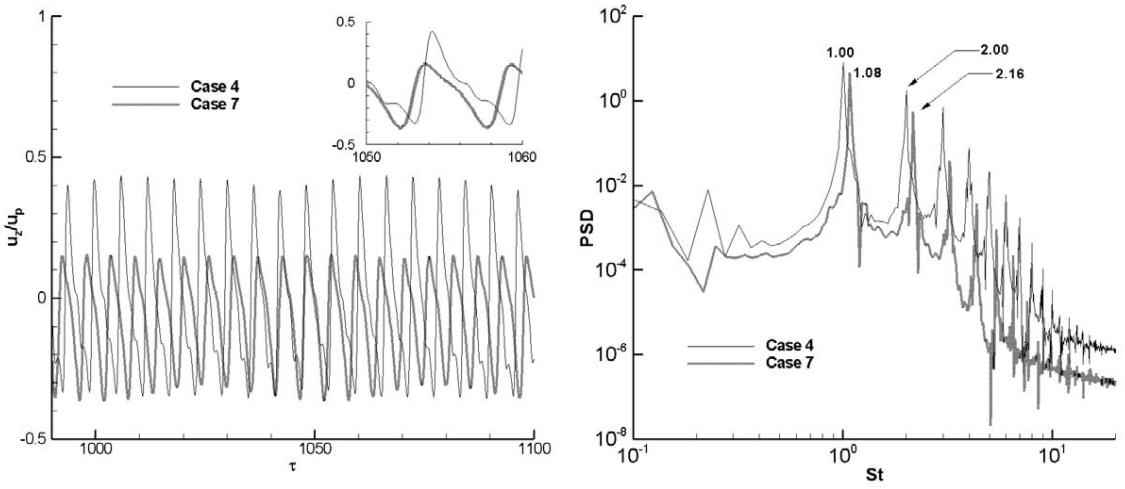

(a) (b)

Figure 4.10: (a) Time series of axial velocity in point P1, cases 4 and 7. (b) Power spectral density of the signal.

with different extreme values; the oscillation is clearly stronger for the complete geometry.

In fact, Figure 4.10(a) clearly suggests different average values in point P1. Figure 4.11 shows the time-averaged radial profile of axial velocity at different axial stations. Differences are indeed noticeable. Magnitude of backflow (positive values) is stronger for case 4, and the inner recirculation zone (IRC) is predicted longer than in case 7. Also the mixing seems stronger in the complete geometry: The positive peaks that signal the presence of primary and secondary fluid injection dissipate upstream in case 4 compared to case 7, and the profile evolves more smoothly.

As a conclusion, a different flow is predicted if a simplified representation of

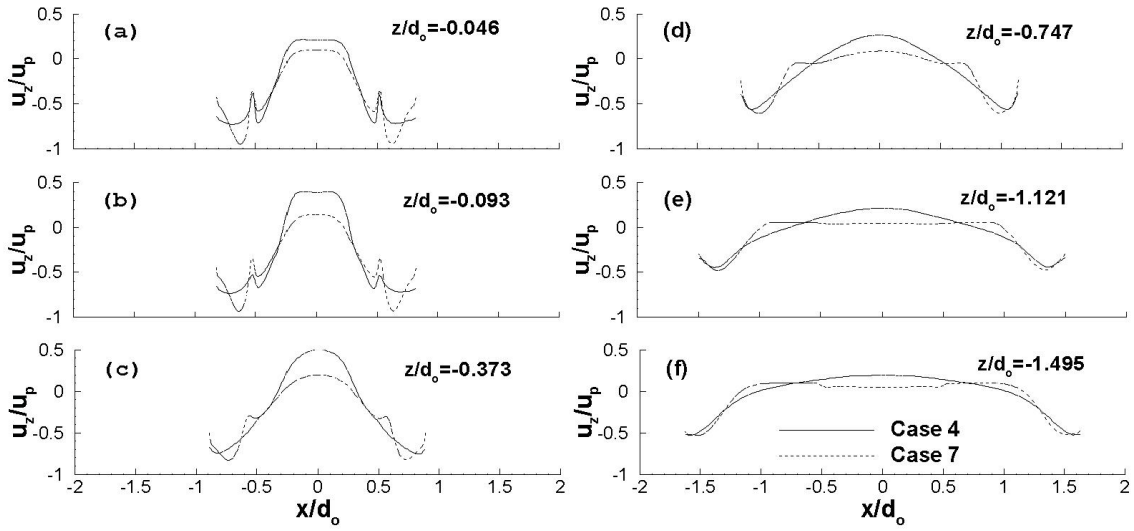

Figure 4.11: Time-averaged axial velocity at different axial positions (Figure 4.1), cases 4 and 7.

the entrance is attempted. It is clear in this case that the simulated oscillation propagates itself upstream to the settling chamber, in a manner that makes the ensemble pulsate differently, with important consequences in the flow patterns. The flow is more oscillatory, which intensifies dissipation and the effect of swirl. Accordingly, cases 2 and 4 are retained for the main study, and 6 and 7 discarded. However, the general implication for the significance of URANS simulations of pulsating flows is not positive. If an adequate prediction of the flow needs such an accurate representation of the entrance, generalization of the models is very difficult. For instance, the small windbox of our pilot combustor is easily amenable to numerical rendition, but this won't be the case of a large, industrial windbox serving a set of individual burners. And vice versa, predictions of ideal cases or laboratory-scale apparatuses could not be extrapolated easily to full-size

equipment.

4.4 Results and discussion

This section examines the oscillating flow solutions obtained by URANS simulations that use the $k-\epsilon$ and Reynolds stresses models of turbulence, cases 2 and 4 of Table 1, respectively. When representing time-series and computing Fourier transforms, averages and other statistics, we discard the initial transient period, retaining only the periodic part. We have organized the presentation in two subsections: time-averaged flow and time-series and spectra.

4.4.1 Time-averaged flow

Figure 4.12 shows profiles of time-averaged axial velocity. We can observe a long inner recirculation zone (positive velocities) and two characteristic peaks that signal primary and secondary air injections. They last up to $z/d_o = -0.093$ and are dissipated by $z/d_o = -0.373$. Differences between both predictions are negligible from $z/d_o = -0.747$ downstream and slight upstream. However, the latter are significant: the simulation with the RSM predicts higher reverse velocities in the near field of the throat.

Streamlines of the time-averaged flow in an axial plane are shown in Figure 4.12, with intervals chosen so as to distinguish vortex and reverse flow zones clearly. Flow inside and close to the throat exhibits what appears to be two toroidal vortexes. The larger is centered approximately at the throat outlet and

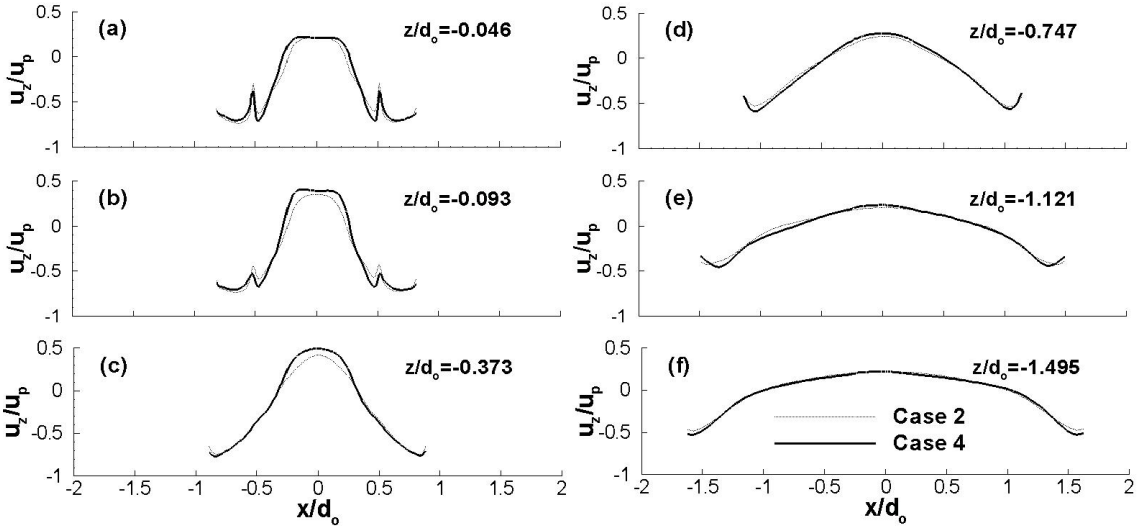

Figure 4.12: Time-averaged axial velocity at different stations in the plane x-z, cases 2 and 4.

penetrates into the chamber, conforming what is classically described as an Inner Recirculation Zone (IRC), see e.g. Figure 1.2 of Syred [151]. There is addition a small torus attached just at the lip of the annular duct, obviously a product of flow detachment. Downstream at the sides we observe the secondary corner vortex originated by the jet. Finally, a second recirculation torus develop that completely fills the chamber.

As for the differences due to the turbulence model, both flows seem to be similar in their basic features and differ only in the details. With the RSM, larger vortices are predicted in the near flow. Their centers are located at $z/d_o = -0.3$, $z/d_o = -2.2$ for case 4 and at $z/d_o = -0.5$, $z/d_o = -1.9$ for case 2. The upper vortex in this latter case ($k-\epsilon$) is of a very reduced size, almost indistinguishable in the plot. In accordance with Figure 4.12(d)-(f), the time-averaged flow apparently

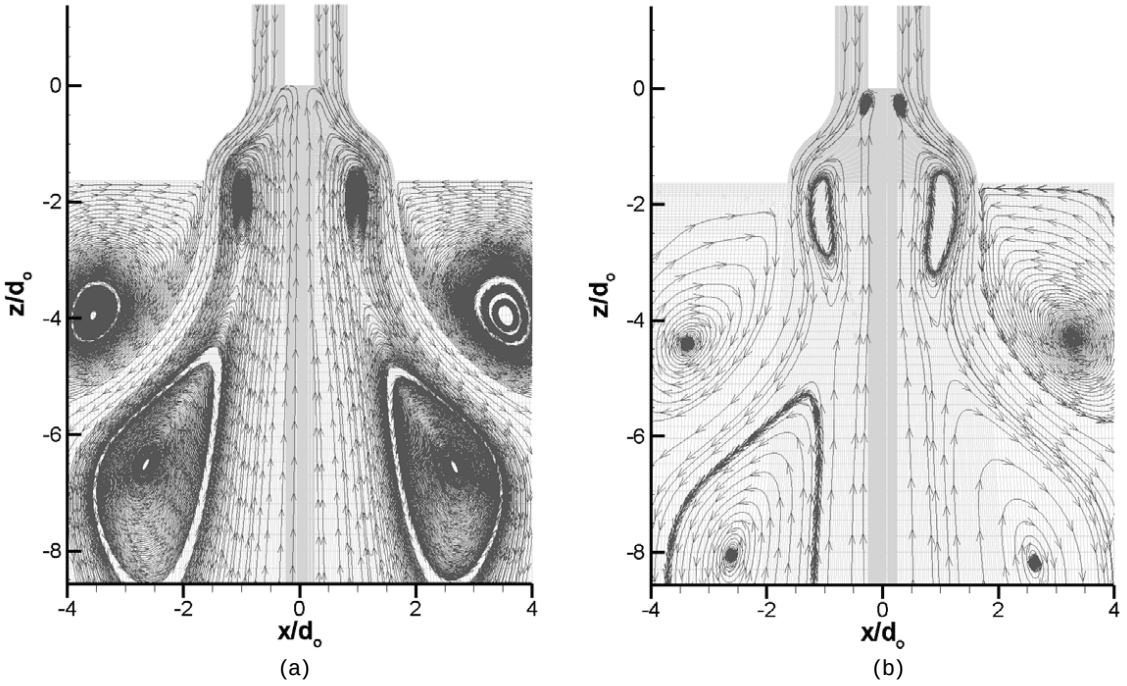

Figure 4.13: Streamlines of the time-averaged flow in the x-z plane (a) Case 2 ($k-\epsilon$ model). (b) Case 4 (RSM).

converges down-stream to an even closer similitude; for instance, the width of recirculation zone at $z/d_o = -3$ is roughly the same, about $1.9d_o$ for case 4 and $2d_o$ for case 2.

This picture is however misleading, because the values and intervals of streamlines are not the same. Rotation in the plane seems stronger and more extended for the $k-\epsilon$ prediction (case 2), but it is so because we are employing much shorter intervals of stream function values in order to detect it. Thus, what we see with the black areas of Figure 4.13(a) are only weak vortexes, that consequently encompass large areas. The flow predicted with the RSM (case 4),

Figure 4.13(b) actually rotates much more vigorously, clearly exhibiting vortexes with concentrated rings and of a richer inner structure.

Finally, it should be noted that the prediction of case 2 is almost axisymmetric, which is in agreement with boundary conditions, barring the surely minor detail of the primary swirler. In contrast, case 4 predicts an asymmetric flow, specially at the throat, in a manner that cannot be related easily to geometry.

4.4.2 Time-series and spectra of flow magnitudes

Figure 4.14 shows time series of the modulus of velocity in the random control points P1-P5 of Figure 4.1(d), as predicted for cases 2 ($k-\epsilon$ model) and 4 (RSM). Velocity seems to be oscillatory everywhere, with an amplitude surpassing 50% of the average in points located upstream and close to the wall (P1). The amplitude drops as the flow evolves downstream, points P5, P3 and P2. Also the oscillation is less pronounced as we move farther from the wall, point P2 vs. point P3. Velocity in P4 is only residually oscillatory, especially for case 2. All these details clearly suggest that the peripheral coherent structures of Figure 4.13 move downstream with the flow, with a central IRZ of ascending flow that is more stable.

Another noteworthy feature is the fundamental difference of the predictions when the RSM is used (case 4) instead of the $k-\epsilon$ model (case 2). In both cases, non-sinusoidal, frequency-rich waveforms obtain. However, the signal is purely periodic for case 2, whereas it presents long time variations for case 4. These variations are much slower than the significant frequency content of the apparent wave-form; it seems as if the second-order closure was successful in

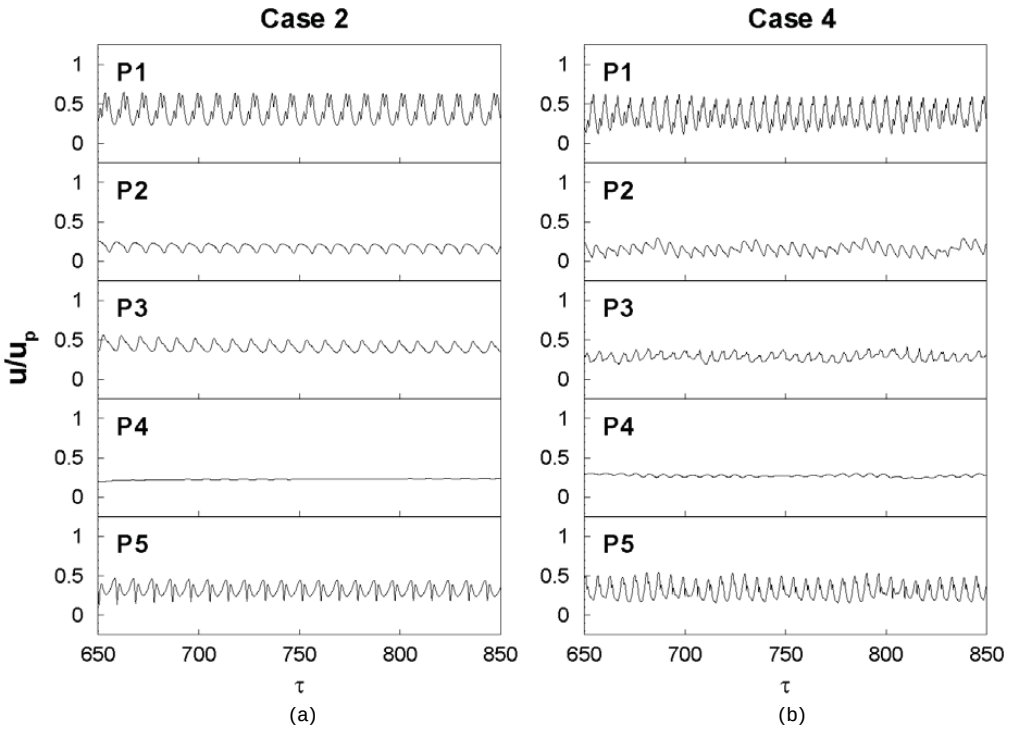

Figure 4.14: Time series of the modulus of velocity in the control points P1-P5, (a) Case 2 ($k-\epsilon$ model). (b) Case 4 (RSM).

modeling a partly stochastic behavior. Obviously this is related to the symmetry of the averaged flow, Figure 4.13: a deterministic prediction will always result in a symmetric flow, whereas a stochastic component seems to realize itself also spatially in non-symmetric flow patterns.

The power spectral density of the signal in point P1 is shown in Figure 4.15 for both predictions. It has been calculated by FFT, and a Blackman window function has been applied to attenuate high-frequency components and clarify the logarithmic plot. A clear dominant, low frequency is predicted in both

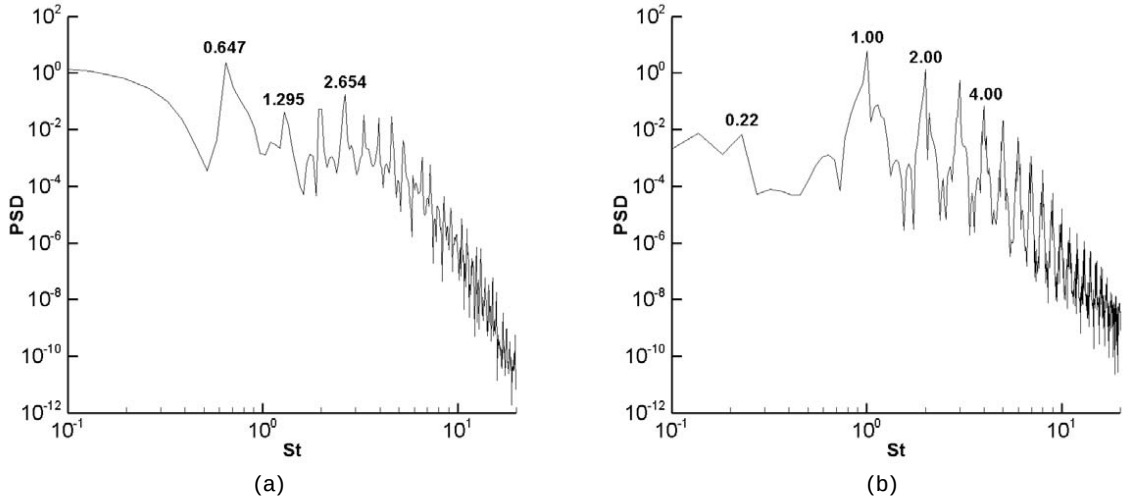

Figure 4.15: Power spectral density of the modulus of velocity at point P1. (a) Case 2 ($k-\epsilon$ model). (b) Case 4 (RSM).

calculations, although the values differ notably: $St = 0.647$ for case 2 and $St = 1.0$ for case 4, which corresponds to frequencies of 15.11 and $23.49\ Hz$, respectively. The peak is somewhat more definite for case 4, but the strength is similar. The spectra also contain secondary harmonics whose frequencies are approximately in a relation of 2 with the dominant and between themselves. They are clearly more intense and definite for case 4. The first three have been indicated in the figure. As noted above, this behavior continues with a much diminished strength up to the high-frequency part of the spectrum. The same dominant frequencies were obtained for pressure, velocity components and velocity magnitude in all monitored points.

4.4.3 Three-dimensional, time-dependent flow and coherent structures

To begin the description of the time-dependent flow, we show in Figure 4.16 six snapshots of flow streamlines in the x-z plane, as predicted in case 4 (RSM), during a complete cycle of oscillation at the dominant frequency ($St = 1$, after Figure 4.15(b)). We observe how the corner vortex seems static and mostly symmetric, though deformed and shaped by the central jet, that is completely dynamical. Apparently, the central ignitor space acts as the rear of a bluff-body from whose surface an unsteady pattern of alternate vortexes detach. But obviously this is an axisymmetric geometry, so that what we actually see is a spiral vortex (SV) permanently attached to the rim of the primary air outlet, that rotates a whole turn. Thus, a vortex break-down of the spiral type, time-dependent and asymmetric, is predicted for our geometry and Reynolds number. The symmetry (or quasi-) and the throat vortexes seen in Figure 4.13(b) are only the time-averaged footprint of this coherent structure, with a strong mark where the spiral vortex is attached and a composite down-stream.

The geometric complication of the burner itself seems to have a minor role. The secondary fluid stream, of roughly double momentum and half the swirl, doesn't originate additional CS, but limits itself to be unsteadily throttled and mixed with the primary stream. Figure 4.17 illustrates another way of looking at this question. Although modeled by RSM, the second moments of the turbulence (for instance, its turbulence kinetic energy) should indicate regions of high shear. The figure shows radial profiles of k/u_p^2 that correspond to the same instant as

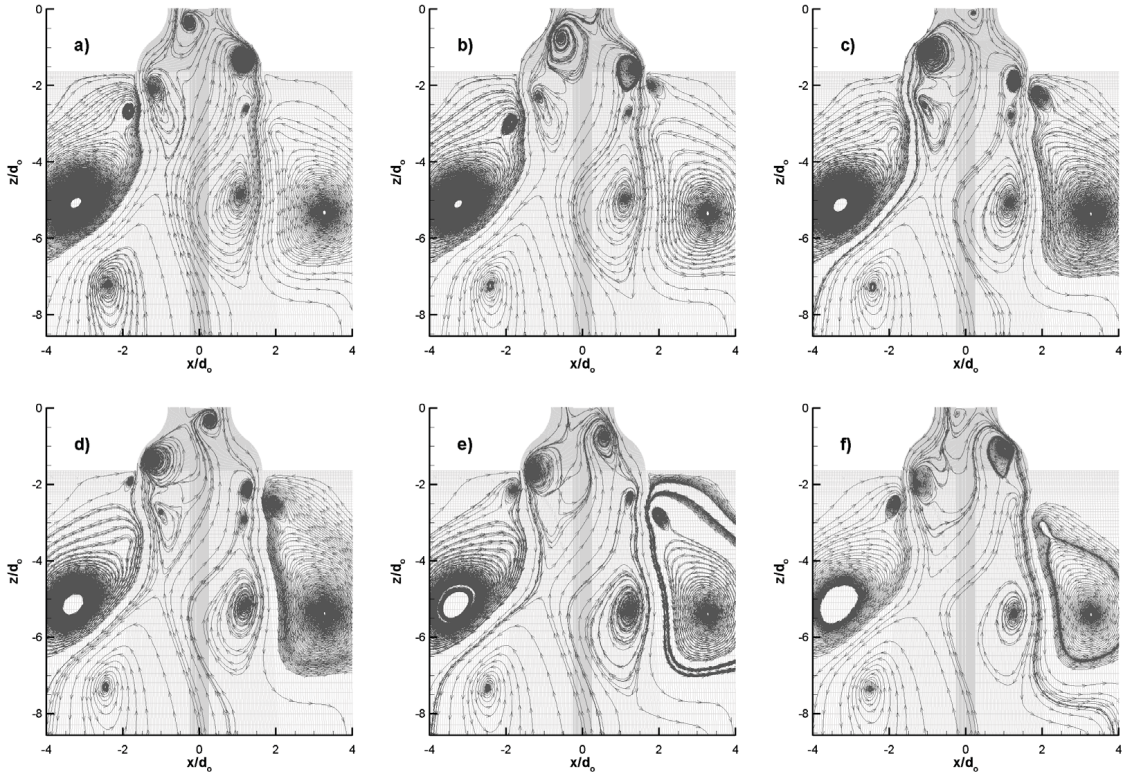

Figure 4.16: Snapshots of flow streamlines in the y-z plane, case 4: a) 0, b) $\pi/3$, c) $2\pi/3$, d) π , e) $4\pi/3$ and f) $5\pi/3$.

Fig 4.16(a); the axial stations (a)-(f) are indicated there. At the highest level (a), which is slightly above the center of attachment of the spiral vortex as seen on the x-z plane, we can distinguish six peaks. These mark the shear layer between successive streams, viz., secondary, primary, vortex and IRZ. By $z/d_o = -0.373$, turbulence kinetic energy drops significantly and the number of peaks reduces to three, the first between the descending stream and the vortex, the second between the vortex and the IRZ and the third between the IRZ and the descending stream; the lack of shear between primary and secondary fluid indicates indeed that they are mixed. From $z/do = -0.747$ downstream, there are only two shear layers, one between the fluid mixture and the recirculation zone (close to the stagnation point) and another between the vortex and the descending stream. The higher values of k indicate that the spiral vortex moves to the periphery, thus increasing the throttling of the descending fluid.

As seen in Figure 4.16, this coherent structure is dissipated not long after the entrance to the combustion chamber, roughly at $z/d_o = -2$. But it induces other two secondary CS that propagate downstream with a weaker intensity. At the outer side of the jet, a small spiral vortex can be observed, e.g., at $z/d_o = -2.75$ and $y/d_o = -1.8$ in Fig. 4.16(a). We will call this structure outer vortex (OV). Looking at the whole sequence, it starts just at the corner between the throat and the wall, thus apparently caused by flow detachment at that point, where the SV and the corner vortex meet, and it seems coupled within the latter. In addition, at the inner jet, an inner, spiral vortex (IV) can be seen, apparently originating slightly downstream where the SV has just dissipated, as an induced, residual motion.

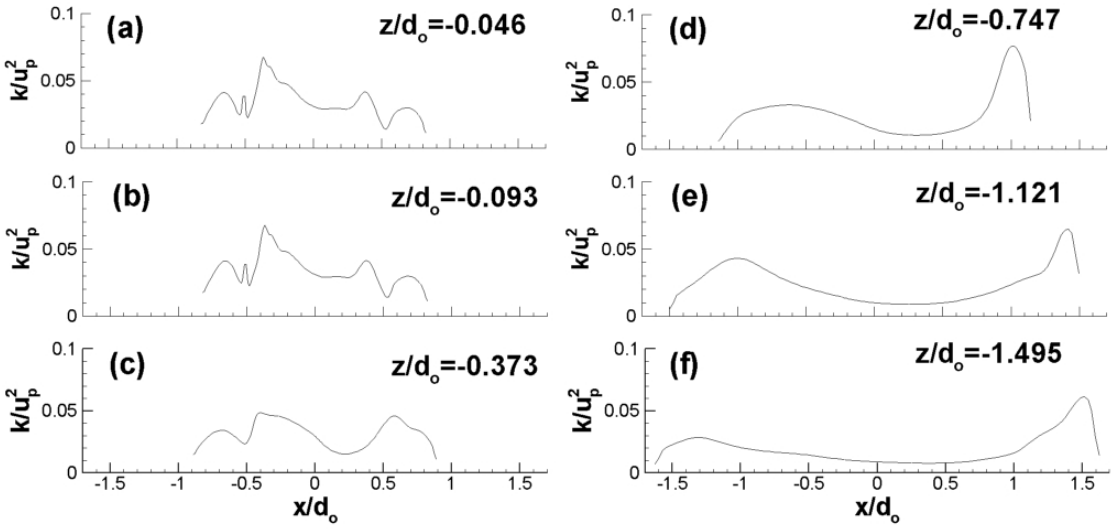

Figure 4.17: Instantaneous profiles of normalized turbulence kinetic energy at different axial positions (Figure 4.1), case 4 (RSM).

Dynamics of both secondary spiral vortexes are completely different. The OV dissipates in a short distance, comparable to that of the SV. It also rotates at a comparable angular speed, as can be deduced from the fact that the apparent alternate detachment repeats itself more or less during the same predefined cycle. On the contrary, the IV seems stationary, which suggest that its frequency is significantly lower. Inside the jet, it doesnt́ dissipate quickly; it instead losses strength and widens, filling the whole chamber. The static and asymmetric appearance of the downstream jet signals both facts; only a long-term time-average can restore some symmetry, as seen in Figure 4.13(b).

To analyze the question in more depth, we employ next the method of eduction of vortical CS developed by Jeong and Hussain [80]. In it, a vortex core is

defined as a connected region with two negative eigenvalues of $S^2 + \Omega^2$, S and Ω being the symmetric and antisymmetric parts of the velocity gradient tensor, respectively. Considering the eigenvalues λ_i ordered, this is equivalent to the condition $\lambda_2 \leq 0$, and the negative intensity of this value indicates that of the vortex. As demonstrated by these authors, the condition detects the pressure defect associated with vortical CS, improving upon other methods (e.g., vorticity isosurfaces), especially for transient flows.

Figures 4.2(a) and (d) show the results for the flow predicted in case 4 (RSM), by means of a 3D isosurface of $\lambda_2/{u_p}^2 = 0$ and an axial color plot of $\lambda_2/{u_p}^2$ values, respectively. The plot confirms the above mentioned features for the three structures, SV, IV and OV. In particular, persistence and relative strength is clearly seen in Figure 4.18(d): The OV is slightly less vortical than the SV and lasts roughly along the same distance, whereas the IV is much weaker but lasts for longer.

As for the frequency of rotation of the three vortices, some figures have been calculated as follows. Considering approximately that the three CS are perfect helical vortexes of constant radius and pitch, we have applied the theoretical model developed by Alekseenko et al. [3]. In this way, the angular speed is deduced from the observed (averaged) pitch and radius and the time of passage of the vortex at a fixed axial section.

From the SV and OV, results are, in dimensionless form, $St = 1.2$ and $St = 0.85$, respectively, which compares quite well with the dominant peak of $St = 1$, Figure 4.15(b). For the OV, the result is 0.13, in agreement with our observations about the static appearance of the downstream jet in Figure 4.16. There is not a

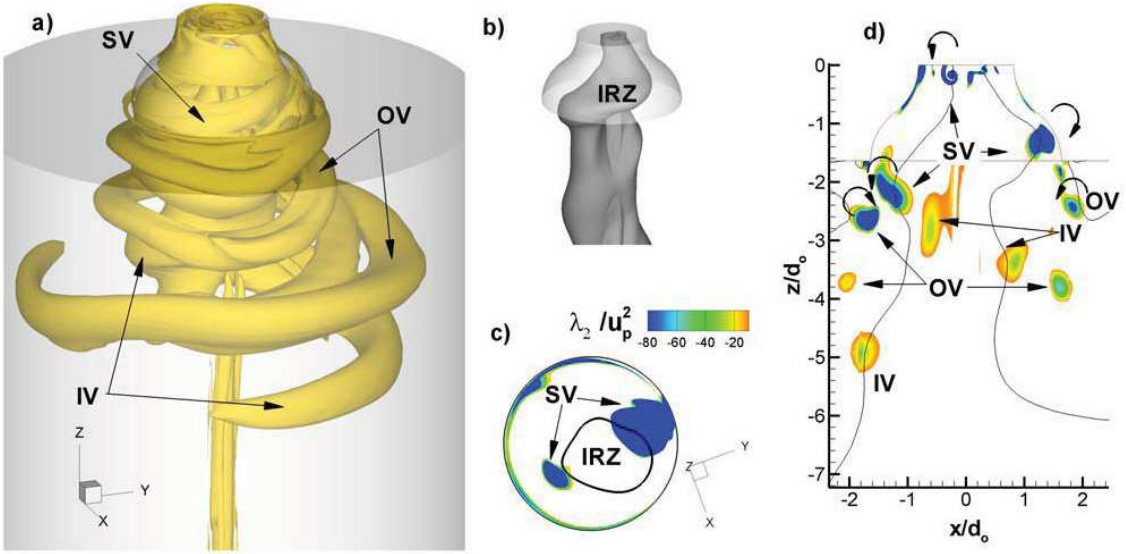

Figure 4.18: Instantaneous flow structures, case 4. (a) Isosurfaces of $\lambda_2/{u_p}^2 = 0$. (b) Isosurface of $u_z/u_p = 0.1$. (c) Color plot of λ_2/u_p in the xy plane, $z/d_o = -0.57$, and contour of $u_z = 0$. (d) Color plot of $\lambda_2/{u_p}^2$ in the x-z plane and lines of $u_z = 0$.

corresponding low-frequency peak in Figure 4.15(b) simply because the record of calculated instants is too short to allow detection by Fourier transform. Note that this agrees with the low frequency variations observed in Figure 4.14(b); it also explains why the time-average flow exhibits residual asymmetry, Figure 4.13(b).

Summing up, the flow can be imagined approximately as three coupled spiral vortices rotating at different speeds. It is also noteworthy that the whole system of CS rotates in a sense opposite to that of the flow, i.e., clockwise, the sense of the swirl being anticlockwise, Figure 4.8. The senses of rotation of the fluid around the spiral axis are indicated by arrows in the xz section of Figure 4.18(d), where we can appreciate how the three vortexes couple between themselves.

The main effect of the vortical CS is to shape and distort the central zone of recirculating fluid, or IRZ, which starts inside the throat but continues well inside the combustion chamber. This is indicated in Figures 4.18 by a isosurface of positive axial velocity, $u_z/u_p = 0.1$. The spiral appearance is evident, a phenomenon normally known as the precessing vortex core (PVC). Here we have shown numerically that it is originated by a system of counter-rotating, spiral-type vortexes. Figures 4.18(c) and (d) show further the effect, by drawing the contours of $\lambda_2/{u_p}^2$ and lines of $u_z = 0$ in the axial plane and a transversal plane just at the end of the throat.

Our results resemble very much those experimentally found by Alekseenko et al. [3], Shtork et al. [138], Cala et al. [20] and Shtork et al. [137]. In this series of works, a system of three spiral, counter-rotating vortexes is educed from PIV measurements at $Re = 1 - 1.5 \times 10^4$ and $S_W \approx 1$, composed by the PVC ("primary vortex") and coupled IV and OV. Differences with our case are

significant, viz.: geometry of throat and swirler, single air entrance and infinite expansion ratio (unconfined flow). This may perfectly explain the differences in flow structure, notably, the absence of a SV in the near-field. In any case, resemblance is noteworthy. On the other hand, we think that the presence of two different air streams has only a limited effect on flow features, due to the high rate of mixing that attains the flow.

Finally, Figure 4.19 repeats the same plots for the prediction of case 2. All the features mentioned above are present, but with significant differences. The prediction with the $k - \epsilon$ model of turbulence appears obviously less rich, and at once more basic, than its counterpart predicted by using the RSM. However, perhaps important features are lost. In particular, all vortical CS are weaker and dissipate earlier, and this affects specially the two secondary vortexes. Accordingly, the IRZ is only distorted by the main spiral vortex inside the throat; it stabilizes and gets symmetric right after entering the chamber. Thus, the flow there can be considered almost steady, contrary to the more elaborated prediction of case 4. The significance of these differences for a combustion system cannot be assessed at this point and must be investigated, i.e., to what extent the loss of intensity of the main vortex changes the near-flow dynamics and whether the practical absence of downstream secondary vortices and PVC is of importance.

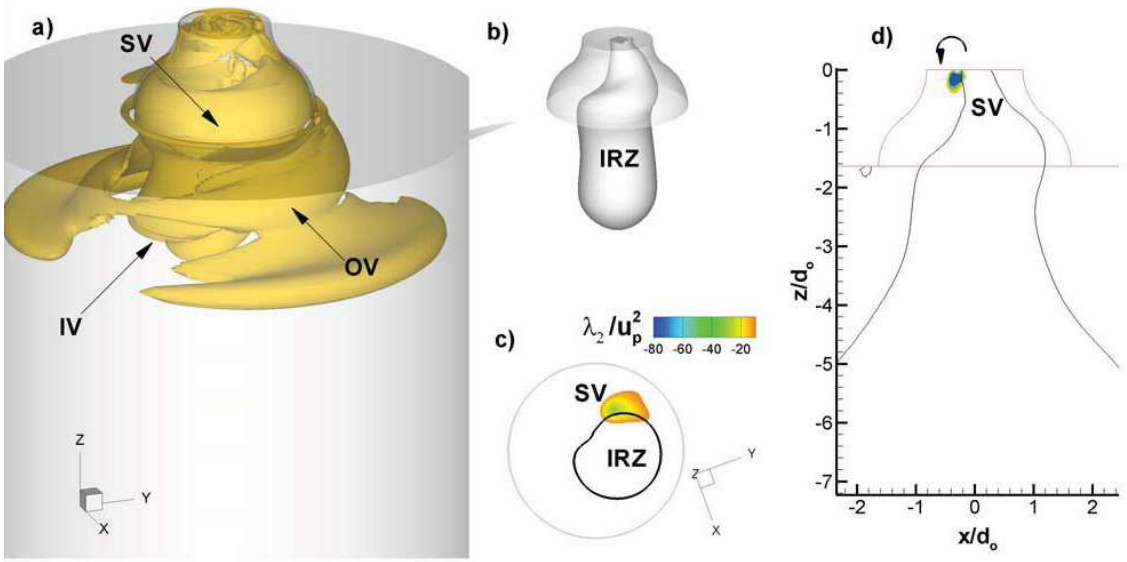

Figure 4.19: Instantaneous flow structures, case 2. (a) Isosurfaces of $\lambda_2/{u_p}^2 = 0$. (b) Isosurface of $u_z/u_p = 0.1$. (c) Color plot of λ_2/u_p in the xy plane, $z/d_o = -0.57$, and contour of $u_z = 0$. (d) Color plot of $\lambda_2/{u_p}^2$ in the x-z plane and lines of $u_z = 0$.

Chapter 5

URANS of turbulent unconfined swirling burner

5.1 Experimental Configuration and Computational Setup

In this chapter, the capacity of prediction of URANS schemes for the simulation of isothermal flow in an atmospheric low swirl burner is studied. A 50 kW atmospheric low swirl burner designed by Legrand et al. [95] is considered. The main characteristic of this burner is that produces a weak recirculation zone which stabilize the flame achieving ultra-low emissions [22, 23]. There are some studies with similar burners which use LES schemes for the flow at isothermal and reactive conditions [72, 71, 52], all of them show advantages for the identification of coherent structures, but we pretend to analyze the performance of the URANS

schemes under isothermal conditions. It is important to mention that numerical results have been compared with the non-reactive experimental measurements made by Legrand et al. [95]. Their experiments are detailed in the following sections.

The burner is completely realistic and some S-PIV measurements have been published [95]. As in Chapter 4, the flow has been simulated with two different, basic, turbulence models, namely second order closure by a Reynolds Stresses Model (RSM) and the $k-\epsilon$ model. In order to assure good numerical results, special emphasis was put in grid-independent solution and the characteristics of the oscillations varying the time step. Flow features are studied and compared with S-PIV measurements. Snapshot POD is used to extract all the information of numerical simulations and link it to physical measurements. Then, the coherent structures are visualized and described with the help of experimental information.

5.1.1 Equipment description and experimental details

In the experiments, velocity and vorticity fields for reactive and non-reactive flows were obtained with S-PIV and then CS were reconstructed via proper orthogonal decomposition (POD). Authors used two CCD cameras and a $532\ nm$ wavelength, $400\ mJ$ Quantel (Twin Brilliant B) double Pulsed Nd:YAG laser for the illumination. The image size was approximately 80×80 mm2 (2000×2000 pixels) in size. For the isothermal case, they used propylene glycol particles, of which 90% have a diameter less than $2\ \mu m$ with a pick in probability density at $1\ \mu m$. With this size of particle they captured maximum frequencies of $1.2\ kHz$. Moreover, a

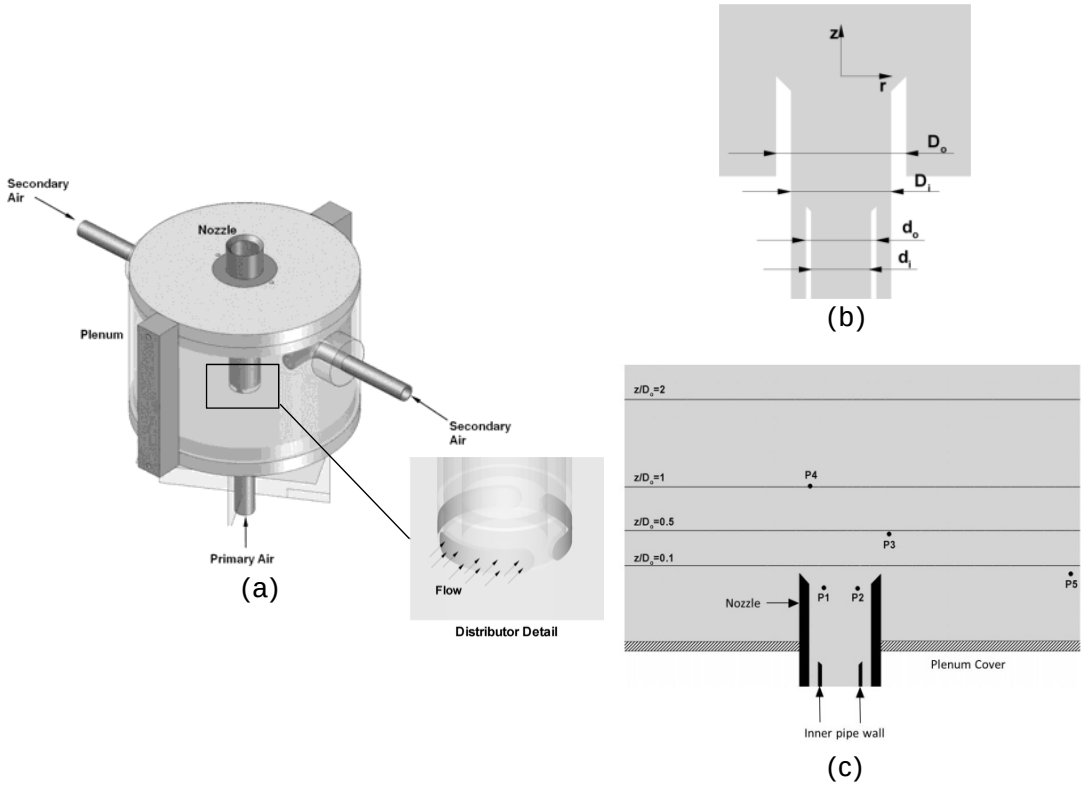

Figure 5.1: Geometry detail: (a) plenum combustor [95], (b) nozzle and (c) levels and monitoring points.

$1/2$ inch B&K condenser microphone was placed at $5.7D_o$ from the axisymmetric axis to acquire pressure signals and via fast Fourier transform calculate acoustic spectral power densities.

In this chapter, we attempt to simulate two non-reactive cases based on their experiments: low swirl case ($S_L = 0.58$) and high swirl case ($S_H = 0.64$). Both under the same mass flow rate, $Re = 12000$ [95]. Reynolds number is based on reference length (D_o) and $\dot{m}$ accounts for the total mass flow rate measured at the burner exit. From continuity, a characteristic velocity is calculated by $u_o = 4\dot{m}/\rho_o \pi D_o^2$ with the objective of dimensionless velocity profiles.

Some arbitrary control levels and monitoring points were considered to compare numerical simulations with experiments, Fig. 5.1c. Moreover, an additional point, located in the same position as the microphone used in experiments to measure acoustics, is also considered. The control level at $z/D_o = 0.1$ is used to analyze the jet flow at the nozzle outlet, where the accelerated flow interacts with surrounding static fluid. The other three control levels ($z/D_o = 0.5$, 1 and 2) are located in the zone where coherent structures develop. More monitoring points have been sampled in numerical simulations, but only four are shown. The first two monitoring points are located inside the nozzle due to the fact that in some CFD studies with similar geometries, (inner pipe retracted), it has been demonstrated that CS begin to form inside the nozzle [52]. The main reason to choose P3 and P4 positions is the interest in capturing velocity fluctuations of the main structure and also capturing the inner recirculation zone, respectively. The point used to monitor static pressure P_{ac}„ that is not plotted in the figure has cylindrical coordinates of (0, $5.76D_o$, 0). It is important to note that the shape

shown in Fig. 5.1b corresponds to a part of the zr-plane where the nozzle and pipe walls are depicted; the inner pipe is retracted a distance D_o from the nozzle exit.

5.1.2 Numerical Modeling, boundary conditions and mesh

Before beginning with the study of the performance of URANS models applied to an unconfined swirl burner, some tests were carried out to make sure that results are independent of the position and type of boundary conditions. The same procedure was followed for a confined swirl burner numerical simulation in Chapter 4. A comparison between two geometries was performed. The first case considering that the computational domain contains the cylindrical plenum and tangential pipes (which feeds the secondary flow), the annular jet and the inner axial pipe (which feeds the primary flow) and the nozzle and surroundings (where both flows merge). The second case considers a reduced geometry where the cylindrical plenum and tangential pipes are not included but approximate boundary conditions used instead.

The analysis was as follows. First, numerical simulations for the complete geometry using RSM were executed based on the mass flow rate of low swirl case ($S_L = 0.58$ and $Re = 12000$). Control levels ($z/Do = 0.1$, 0.5, 1 and 2) were used to obtain mean velocity values. Also, some monitoring points were located along the annular pipe region, all of them before the nozzle zone. The purpose of these additional monitoring points was to identify velocity fluctuations. It was found that instabilities produced by vortex breakdown propagated always downstream

and never upstream. In other words, fluctuations inside the annular pipe were inexistent.

This result makes it possible to construct a reduced case in which the annular pipe is cut in a region where the flow is fully developed. As inlet boundary condition, a previously simulated velocity profile is imposed in order to ensure that swirl generation is maintained for the reduced geometry that lacks cylindrical plenum and tangential pipes, Fig. 5.2. Values of axial, tangential and angular velocities in control levels ($z/D_o = 0.1$, 0.5, 1 and 2) for this reduced geometry were compared with those of the complete case.

It was found that the velocity profiles were similar in all control levels and the frequencies of the fluctuations in the vortex breakdown zone were equal in both cases. It is arguably that the results differ from those in Chapter 4 where the conclusion was that the swirler must be simulated. However, this only indicates that local disturbances in confined swirl burners are propagated both upstream and downstream so that it is very important to choose a correct position of inlet boundary conditions, and, if the disturbances propagate until the swirler zone, the swirler needs to be part of the domain. In contrast, for unconfined swirl burners, it seems that local disturbances propagate only in the downstream direction, so that it is possible to make numerical simulations without considering the swirler in the domain.

Based on this, the computational domain includes only the annular jet, the inner axial pipe and the nozzle, Fig. 5.2. Inflow boundary conditions are imposed assuming uniform and steady velocity profiles at the inlet sections. For primary air, only the axial velocity component is imposed, while for secondary air, tangential

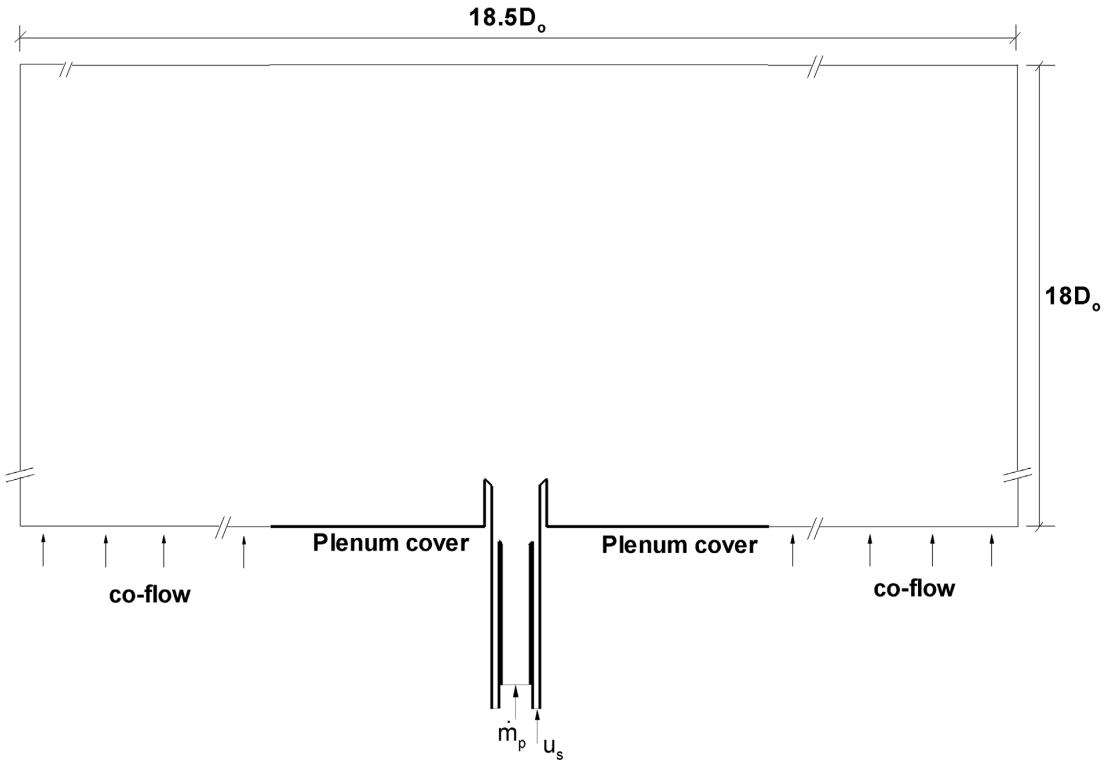

Figure 5.2: Computational domain.

and axial velocities components are considered.

For the high swirl case ($S_L = 0.64$ and $Re = 12000$), numerical simulations begin with arbitrary values of velocity components. When the axial and tangential velocity profiles are obtained at level $z/D_o = 0.1$, they are compared with experimental measurements at the same level. Then, the values of velocity components are adjusted until swirl number and velocity profiles match the experimental values. The methodology has been also validated by García-Villalba et al. [50, 51, 52] who demonstrated good accuracy in averaged and statistic results without the costly representation of the plenum.

With the problem of inlet boundary condition solved, simulations were performed with the Computational Fluid Dynamics solver FLUENT 6.3. The standard $k-\epsilon$ model [92] and a Reynolds stress model with linear pressure-strain term [48, 58, 88] are adopted to solve the incompressible unsteady Reynolds-averaged Navier-Stokes (URANS) equations. Second-order central differences for convection and diffusion terms and an implicit second-order scheme for the time derivatives are employed. The SIMPLE algorithm is used as the pressure-velocity coupling method. Standard wall functions are used for near-wall modeling [92]. The first grid point is located at a distance of $y^+ = 50$ for all meshes.

A far-field study is performed using a constant value of 1 bar for pressure as boundary condition at the exit. This value corresponds to the ambient pressure. Three different geometries with different lengths ($9D_o$, $18D_o$ and $27D_o$) are compared following the procedure of Chapter 4. Accordingly, the computational domain is extended to a length of $18D_o$. With respect to the lateral boundary, a constant value of 1 bar for pressure as boundary condition is used. Also, a

co-flow stream of 5% of the bulk velocity at level $z/D_o = 0.1$ is considered. In spite of the fact that this stream is not present in experiments, it is necessary to adopt it in the simulations of non-confined swirling flows [51]. The reason is that surroundings feed the flame with air, but those convective cells cannot be a part of the domain for obvious reasons of economy of the computation. An alternative way to correctly simulate this feeding is then by means of an artificial co-flow. García-Villalba [53] have shown that a value between 5% and 10% of the bulk velocity is appropriate; higher velocities would have an effect strong enough to alter the swirl behavior, and zero co-flow velocity would result in unrealistic swirl profiles.

Figure 5.3 shows computational grid. It can be noted that all zones are represented by structured mesh. Three meshes with different cell density are used for the study of grid independence, namely: a coarse grid with 535400 elements; a medium grid with 1255800 elements; and, a fine grid with 2811621 elements. Based on the recommendations given by Celik et al. [21], who claim that a grid refinement factor greater than 1.3 needs to be chosen to minimize truncation errors, we use $r_{2,1} = 1.328$ and $r_{3,2} = 1.308$.

5.2 Grid Independence Analysis

Swirl flow is characterized by high temporal instabilities. For this reason, numerical simulations must ensure high quality in the predictions, i.e. that they are independent of grid and of time step used. For steady-state systems, a widely accepted method to obtain an estimate of the numerical error is by means of grid-

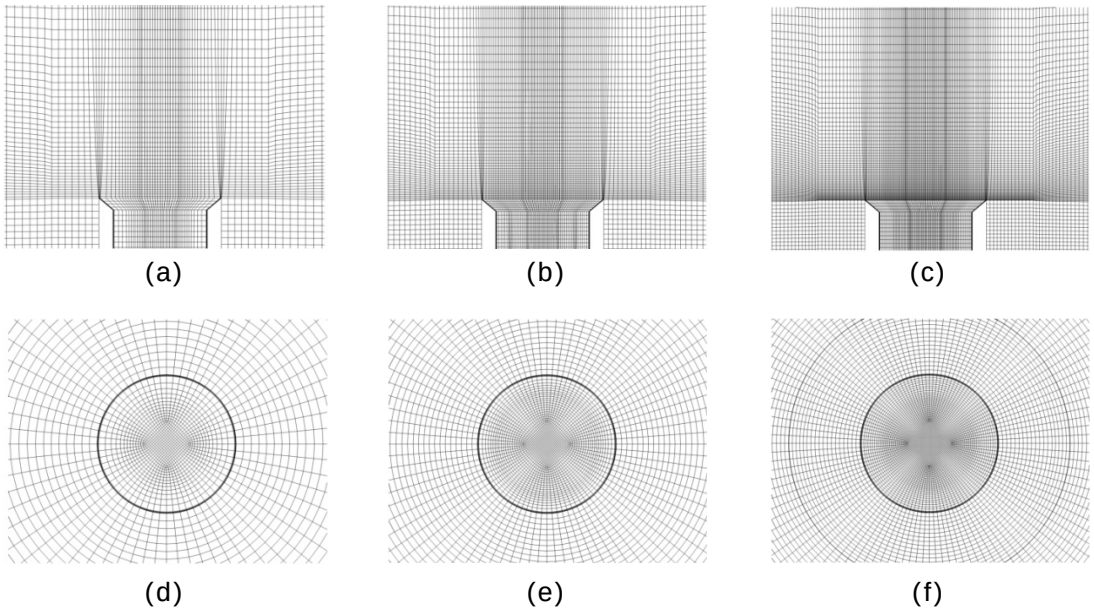

Figure 5.3: Mesh details: (a)(d) coarse grid, (b)(e) medium grid and (c)(f) fine grid.

refinement studies using classical Richard Extrapolation (RE) [21]. In this case, it is additionally necessary to perform an analysis of frequency content of the results and to refine the numerical time step. As a base case, we have used the values of Swirl and Reynolds numbers of $S_H = 0.64$ and $Re = 12000$, respectively.

The procedure is as follows. First, an artificial flow field is fabricated using solutions of simpler models or, in the case of medium and fine grids, values from the solution in the coarse grid are interpolated. The fabricated flow for coarse grid comes from a steady (RANS) solution obtained by using a first-order scheme for spatial discretization and the $k - \epsilon$ model. A time step of $\delta t = 10^{-4}\ s$ is used in the coarse grid to initiate the transient solution until it begins to settle down to a stable oscillation; then the average is calculated and extrapolated to the medium and fine grids, for which unsteady flow is calculated with the same time step. Finally, the average of each grid is obtained.

In order to estimate the effect of the numerical time step on the oscillations, three values are tested ($\delta t = 10^{-4}$, 2×10^{-5}, and 5×10^{-6}). These estimations are evaluated for the RSM model following the same procedure in the medium grid. For a detailed description see Chapter 4. Figure 5.4 shows the results for three values of δt. The power spectral density (PSD) of the static pressure for point P_{ac} is represented. Considering the first harmonic of $\delta t = 2 \times 10^{-5}$ as the reference value, there is a difference of 12% with respect to the prediction for $\delta t = 10^{-4}$ and of only 3% with respect to that of $\delta t = 5 \times 10^{-6}$. As a conclusion, a time step of $\delta t = 2 \times 10^{-5}$ is selected for the rest of the study.

Figure 5.5 shows the time-averaged axial velocity profiles at four stations computed in the three grids for the $k - \epsilon$ model. Differences can be appreciated

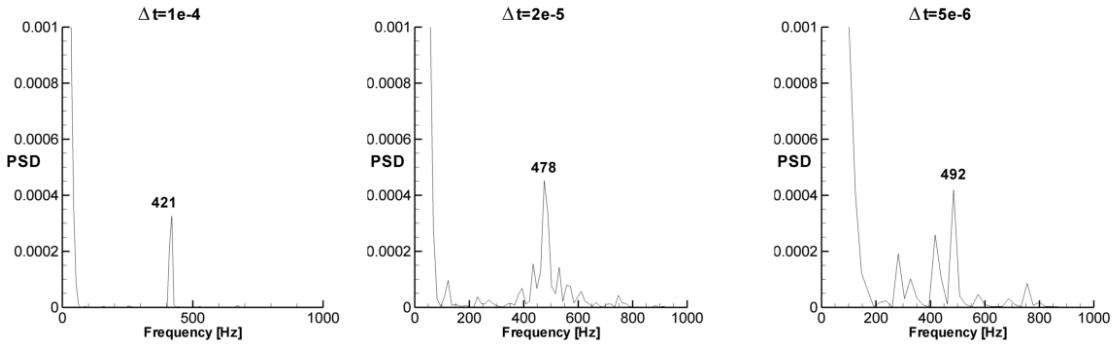

Figure 5.4: Spectral analysis for pressure monitored at the point P_{ac} for three time steps.

but they are small. Differences can be appreciated but they are small. One way to calculate the error is to follow the procedure recommended by Celik et al. [21], the so-called grid convergence index (GCI) method which is based on the Richardson extrapolation. At $z/D_o = 0.1$, the local apparent order of accuracy ranges from 0.04 to 11.52 with an average of 5.64. The maximum discretization uncertainty is 7.58%, which corresponds to $\pm 0.51\ m/s$. At $z/D_o = 1$, the local apparent order of accuracy ranges from 0.7 to 7.36 with an average of 6.85. The maximum discretization uncertainty is 6.67%, which corresponds to $\pm 0.45\ m/s$.

For the whole domain, the volume average of local apparent order of accuracy p is 7.72. The volumetric grid convergence index $GCI_{21} = 9.95\%$ and $GCI_{32} = 6.50\%$. Oscillatory convergence occurs in 23% of total grid points. These values indicate that computations of the time-averaged flow have a good accuracy using the medium grid. In addition to the analysis of inlet and outlet boundary conditions, this assures that results are independent of geometry, grid size, time step used, and type and position of the boundary conditions.

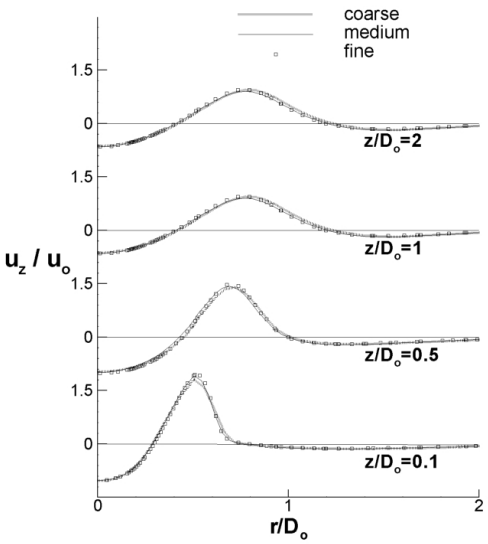

Figure 5.5: Mean axial velocity for the three grids.

5.3 Results and Discussion

In this section the swirl flow solutions obtained by URANS simulations are examined and compared with experimental data. First, predictions with both turbulence models are analyzed and then time series and spectra are presented. Finally, unsteady 3-D coherent structures are discussed.

5.3.1 Mean Flow Field

The experimental data set was obtained with the S-PIV technique [95]. The average of quantities was calculated with $1,000$ snapshots. Figure 5.6 shows the comparison between URANS models and the related experimental results. Figures 5.6a and 5.6b represent the and tangential velocities, respectively, for the low

swirl case ($S_L = 0.58$), Figures 5.6c and 5.6d show the same velocities for the high swirl case ($S_H = 0.64$). Results obtained with both the $k-\epsilon$ model results and Reynolds stress model are near the experimental measurements. Both models predict in good agreement the recirculation zone for high swirl flow (negative values of axial velocity), especially at $z/D_o = 0.1$. This is important because it means that the inlet boundary conditions are correctly modeled.

The experiments and simulations indicate the absence of recirculation zone at any level in the low swirl case, Figure 5.6a. The axial velocity is predicted with better accuracy by the RSM in comparison with $k-\epsilon$ model. But at $z/D_o = 2$ the two models have similar peaks for axial velocity. For the tangential velocity, Figure 5.6b, the $k-\epsilon$ model gives strongest peaks compared with RSM; the shape of the peaks predicted by $k-\epsilon$ model is in good agreement with the experimental measurements. For the high swirl case, the axial and tangential velocities are better represented by the $k-\epsilon$ model than by RSM.

5.3.2 Fluctuating velocity and spectra

Figure 5.7 shows the simulated (RSM) time series of axial velocity for the monitoring points defined in Figure 5.1. The time series of static pressure of the point P_{ac} are also plotted. It can be observed how the velocity amplitude is higher for the points $P1$ and $P2$ and drops for $P3$ and $P4$. $P4$ is residually oscillatory. The axial velocity fluctuations for the points $P1$ and $P2$ are of the order of $1.5u_o$.

The power spectral density of $P1$ and P_{ac} is shown in Figure 5.8. Clearly there is a dominant frequency for the pressure measurement P_{ac} at $478\ Hz$. For axial

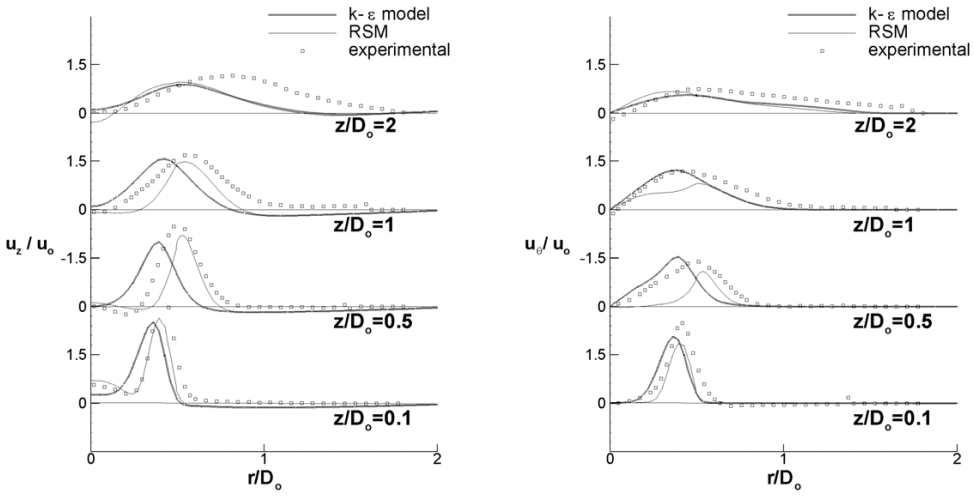

(a) axial velocity for low swirl case (b) tangential velocity for low swirl case

(c) axial velocity for high swirl case (d) tangential velocity for high swirl case

Figure 5.6: Axial and Tangential velocity of the URANS models vs. experimental data.

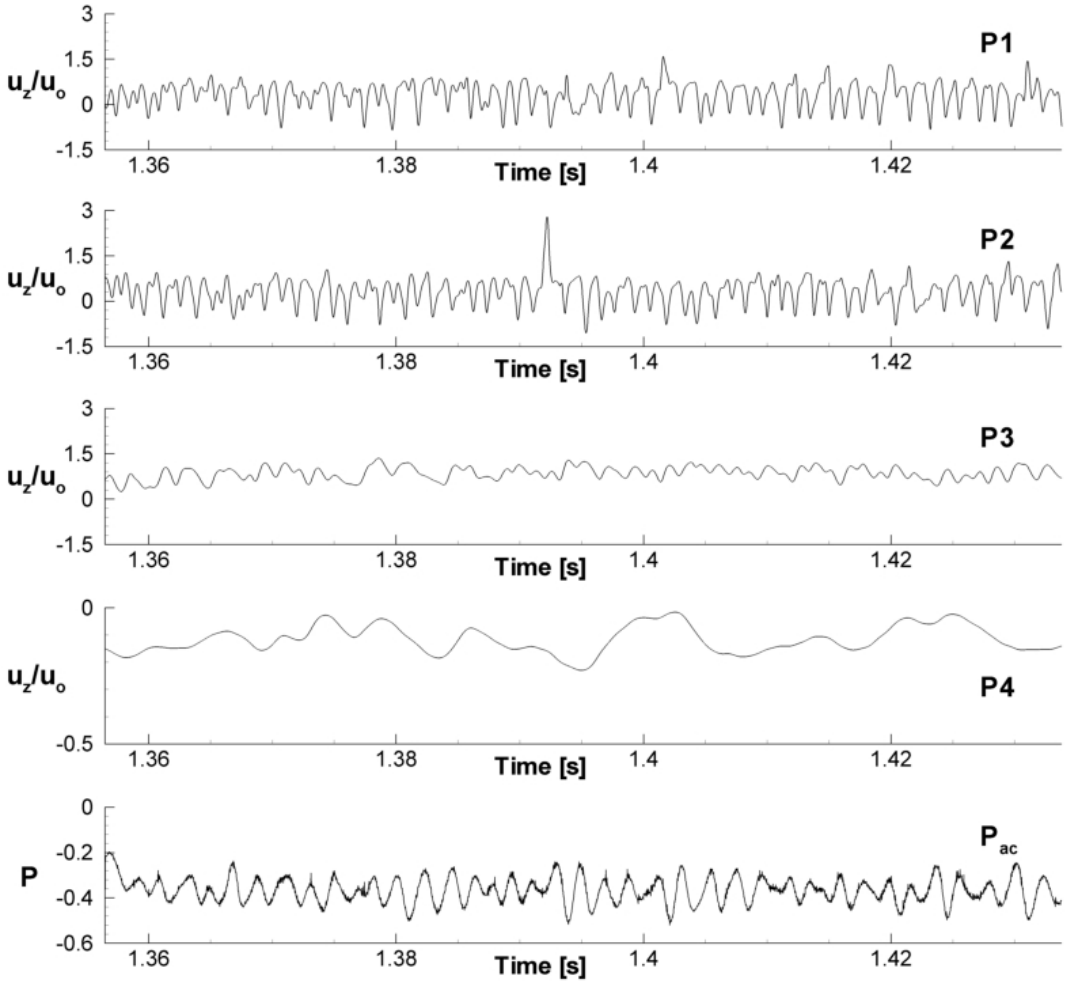

Figure 5.7: Time series of the axial velocity and static pressure $[Pa]$ for monitoring points $P1 - P5$ and P_{ac}.

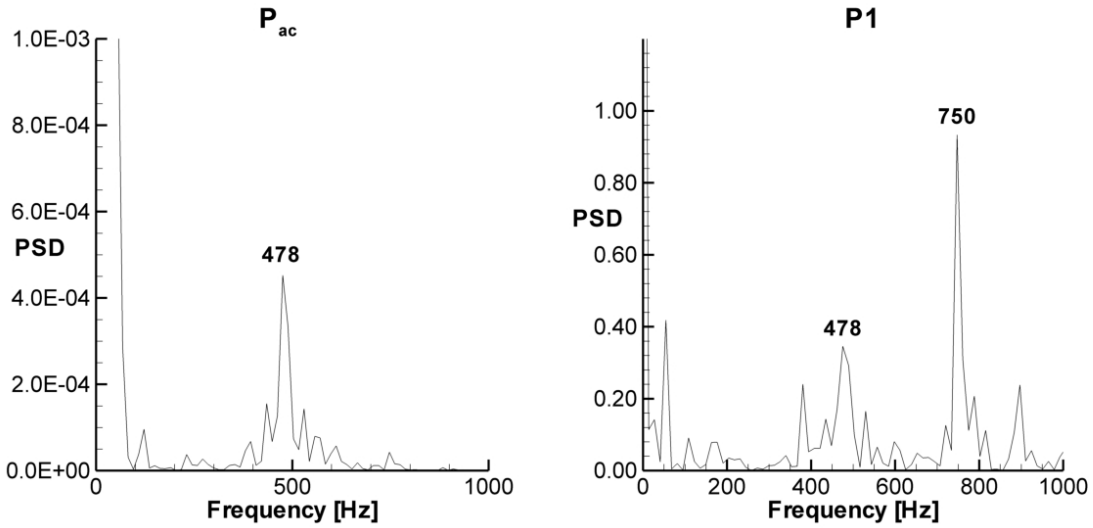

Figure 5.8: Power spectral density of the static pressure (P_{ac}) and the axial velocity ($P1$) for RSM and high swirl case.

velocity $P1$, the dominant frequency is 750, but a minor peak at a frequency of 478 Hz can be observed too. In experimental results at the same Reynolds and swirl numbers, the peak is located at a frequency of 500 Hz [94].

5.3.3 Instantaneous flow and coherent structures

Before starting with coherent structures analysis, snapshots of the simulations of axial vorticity are presented in Figure 5.9 for the case of RSM and high swirl number. This figure shows the snapshots during a complete cycle of oscillation based on the stronger frequency peak of $P1$ in Figure 5.8. White color indicates positive values of axial vorticity while dark colors indicate negative values. Thick-line indicates zero axial velocity. The purpose of drawing the zero axial velocity

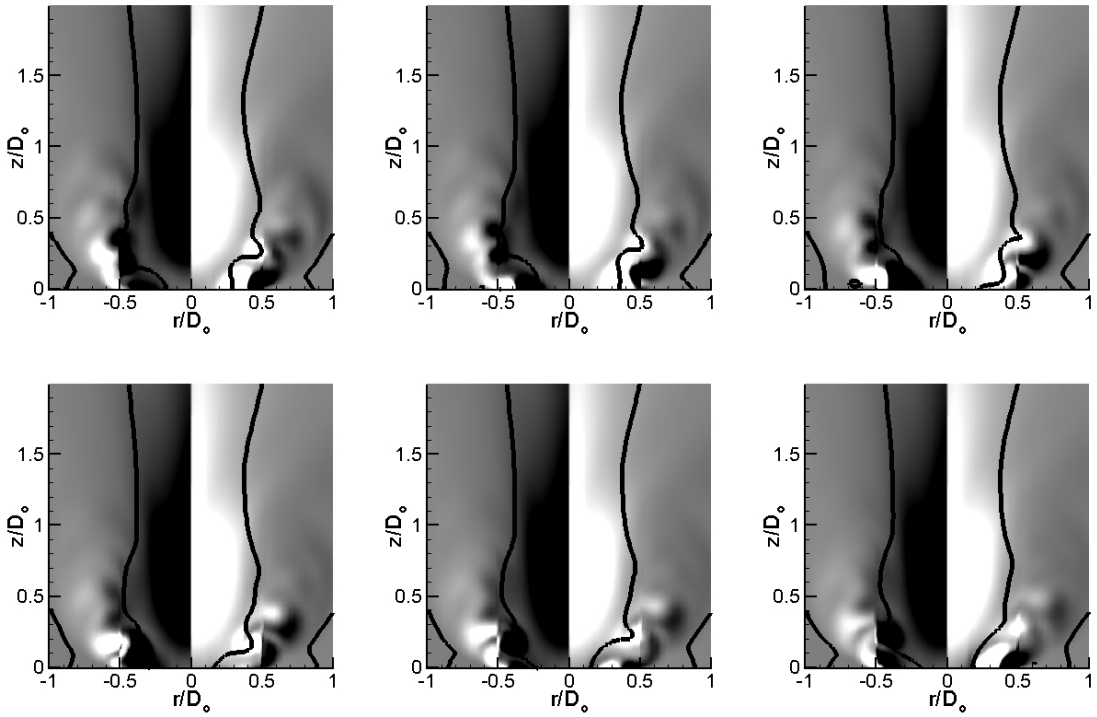

Figure 5.9: Axial vorticity snapshots in the $r-z$ plane for RSM and high swirl case for: (a) 0, (b) $\pi/3$, (c) $2\pi/3$, (d) π, (e) $4\pi/3$ and (f) $5\pi/3$. The maximum value of velocity is $1000\ s^{-1}$ (white) while the minimum value is $-1000\ s^{-1}$ (black).

line is to identify the so-called Inner Recirculation Zone (IRZ) of the swirl flow. This zone is represented in Figure 5.9 by the region delimited by the thick-line in the coordinates $-0.5 < r/D_o < 0.5$. The shape of the IRZ is distorted and asymmetric. The shape and asymmetry of this coherent structure is related to the vortices observed in Figure 5.9, as explained below.

In the right side of the Figure 5.9a there are two white color vortices coupled with three black ones. (Black and white indicate the sense of rotation).

Some white vortices clearly touch the zero axial velocity line as well as the complementary three black vortices on the opposite side of the graph. The term Inner Vortex (IV) is applied to those structures which touch the zero axial velocity line, whereas Outer Vortex (OV) is considered to comprise those structures coupled with the IV in the zone of positive axial velocity. It can be noted that the vortices evolve similarly as a 2D von Kármán Vortex Street with the IRZ acting as a bluff body. All the vortices propagate downstream and vanish during the first half of the period, Figure 5.9a-d. During the second half of the period, Figures 5.9d-f and back to 5.9a again, new vortices arise with weak intensity compared with those structures in the first half of the period. However, at this instance, it is impossible to know the type of vortices present in the flow. For that reason, it is necessary an advanced analysis of numerical data. The snapshot-POD method is employed with the complementary method of eduction of vortical coherent structures developed by Jeong and Hussain [80].

Legrand et al. [95] collected enough experimental data, ($1,000$ S-PIV statistically independent snapshots), and used the proper orthogonal decomposition method as a technique to identify coherent structures. The main advantage of using the POD method is that it consists of a linear procedure which processes input data, based on the Fredholm integral eigenvalue problem, that creates an orthogonal basis of a, in this case, non-linear phenomenon. In other words, POD takes an ensemble of the data and extracts basis functions; these functions are optimal in terms of the representativeness of the data.

There are two different POD existent approaches: Classical POD and the snapshot POD. In classical POD, the variable $\mathbf{X}$ is assimilated to the space $\mathbf{x}$=(x,y,z)

defined over the domain Ω_S and, based on the assumptions of stationarity and ergodicity, it is evaluated as an ensemble average or, in other words, as a temporal average. On the other hand, the variable **X** in snapshot POD is assimilated to the time t and it is evaluated as a space average over the domain Ω_S.

It is necessary to evaluate which one of the two POD approaches is more adequate for S-PIV and numerical simulations. S-PIV provides a good spatial resolution, but associated with a poor temporal resolution. Numerical simulations are highly resolved in space and time but only a very short time sample can be simulated. Therefore and based on the previous description, snapshot POD is the chosen method for treating experimental and numerical data.

Sirovich [141] introduced snapshot POD method as a way to capture a good picture of the large scale behavior in turbulent flows. The principal advantage of this technique is the fact that the autocovariance matrix can be approximated by a summation of snapshots instead of solving a $n \times n$ eigenvalue problem which is very time-consuming. In their experiments, Legrand et al. [95] used this method to reconstruct a helicoidal vortex by means of azimuthal vorticity 2D-fields. This structure is, presumably, the responsible of the pressure oscillation mechanisms which leads to the acoustic peak measured by the microphone. But, a deep analysis is necessary to understand the interactions between the coherent structures and measurements.

Recently, numerical simulation has emerged as a complementary tool for S-PIV measurements due to its capacity to resolve the system with a considerable quality in space and time. The performance of URANS models is evaluated by using these advanced postprocessing tools. For this, a case has been selected with high swirl,

RSM and a time step of $\delta t = 2x10^{-5}$. A window of $80 \times 80\ mm^2$, positioned in an equivalent place as in the experimental S-PIV measurements, has been used to obtain numerical data. The statistical representation was computed from $1,000$ snapshot (N). These $1,000$ snapshots were collected with the same sampling rate as in experiment, 0.5 seconds.

The procedure followed is the following. First, a matrix $\mathbf{M} = \left[\omega^0\ \omega^1\ \cdots\ \omega^N\right]$ is defined, where each column corresponds to a snapshot of the azimuthal vorticity (ω). Then, the autocovariance matrix is calculated, $\mathbf{C} = \mathbf{M}^T\mathbf{M}$, and the eigenvalue problem solved, $\mathbf{C}\mathbf{A}^i = \lambda^i\mathbf{A}^i$. Once eigenvalues are calculated, they are sorted in descending order, $\lambda_0 > \lambda_1 > \cdots > \lambda_N$, as well as the eigenvectors (each column of $\mathbf{A}^i$). Finally, the normalized POD modes were found as:

$$\phi^i = \frac{\sum_{n=1}^{N} A_n^i \omega^n}{\left\| \sum_{n=1}^{N} A_n^i \omega^n \right\|}, i = 0, \cdots, N \tag{5.1}$$

Each POD mode, ϕ^i, is the representation of the energy contained in the flow. In this sense, the most energetic realization is the mode 0 where the energy contained is about 72.03%; modes 1 and 2 contain 8.22% and 4.65%, respectively. Only three modes have been analyzed due to the fact that this quantity is enough to produce vortices [95]. It is possible to add more modes to improve smaller details of the vortex field, but some studies have demonstrated that the main structures are unchanged [115, 114]. Figure 5.10 the contribution of POD modes to each. The random nature of the sampled numerical data is clearly observed. Because of this, the data need to be shorted.

In this context, a phase averaging using POD coefficients can be obtained

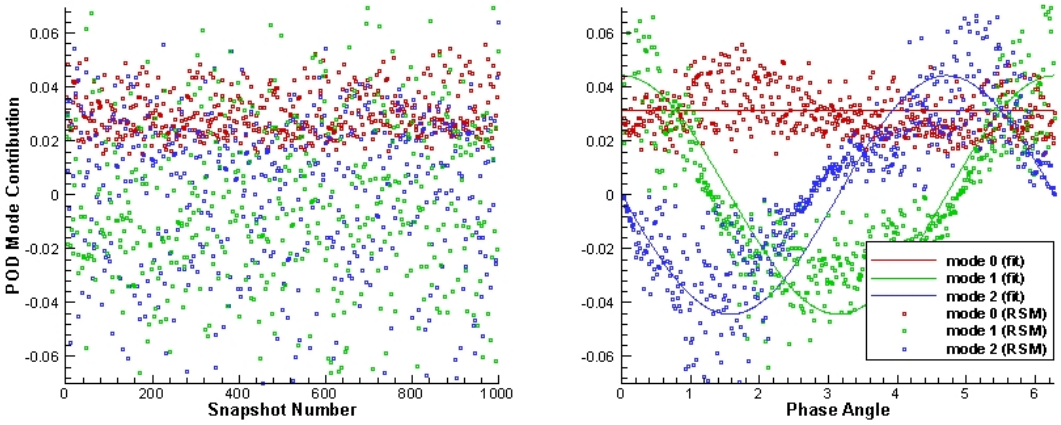

Figure 5.10: Snapshots POD modes contribution: randomly and phase averaging.

following the same procedure used for experimental data by et al. [95]. Data of azimuthal vorticity (ω_θ) can be decomposed as a sum of the time-independent mean flow, a quasi-periodic fluctuating component and a random fluctuating component: $\omega_\theta = \overline{\omega_\theta} + \widetilde{\omega_\theta} + \omega_\theta{}'$; the term $\overline{\omega_\theta} + \widetilde{\omega_\theta}$ is the phase averaged vorticity. Writing it as a Fourier expansion, with the use of only the three first POD modes and retaining the fundamental frequency, $\langle\omega_\theta\rangle \cong \overline{\omega_\theta} + \sum_{n=1}^{\infty}(B_n\cos(\varphi) + C_n\sin(\varphi))$, Legrand [94] approximates the autocovariance matrix, **C**, in an alternative way and calculate the eigenvalues as:

$$\begin{aligned} \lambda_i^0 &\approx \frac{1}{\sqrt{N}} \\ \lambda_i^1 &\approx \pm\sqrt{\frac{2}{N}}\cos\left(\frac{2\pi i}{N}\right) \\ \lambda_i^2 &\approx \pm\sqrt{\frac{2}{N}}\sin\left(\frac{2\pi i}{N}\right) \end{aligned} \tag{5.2}$$

Using this procedure it can be observed that the eigenvalues depend only on the number of snapshots; also, it can be noted that the eigenvalues 1 and 2 are shifted by a quarter of period. Due to this, some authors have related these two POD modes to the convection of the vortices. Figure 5.10 shows the POD mode contribution that has been alternatively calculated, fit lines, and the POD mode contribution based on the autocovariance matrix $\mathbf{C} = \mathbf{M}^T\mathbf{M}$ that has been alternatively calculated and the fit lines. It can be observed a sinusoidal evolution of the random collected data and their respective strong dispersion when the data have been phase averaged. With this, the vorticity fields can be re-evaluated using any phase angle.

Figure 5.11 shows the phase averaged POD reconstruction for (a) experimental and (b) numerical data with a value of phase angle $\varphi = 0°$; both graphics share the same vorticity scale. It can be observed that numerical simulations are able to predict the same number of cores. Furthermore, structures captured by S-PIV of experimental data are of the same size in comparison with vortices in numerical simulations. Or, in other words, RSM seems to be an acceptable way of predicting the strength of the coherent structures. In addition, it is observed

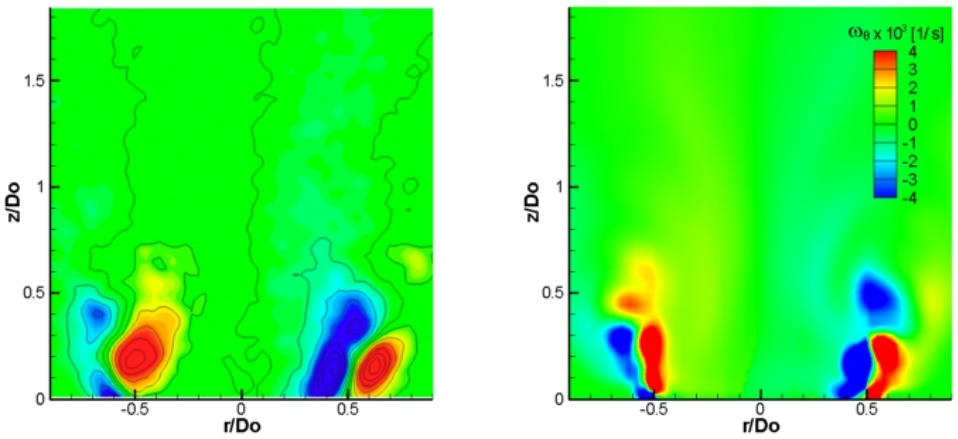

(a) (b)

Figure 5.11: POD reconstruction of azimuthal vorticity for high swirl case: (a) experimental [94] and (b) numerical.

that the inner vortices are surrounded by counter-rotating vortices, and they are clearly divided by shear layers. It can be noted that experimental and numerical POD reconstruction lacks the IRZ observed in Figure 5.9. It indicates that axial vorticity dominates over azimuthal vorticity for the IRZ. Since the axial vorticity is capable to predict both the inner vortices and IRZ, we use it for the analysis of the coherent structures.

Since the simulation has been validated with experimental measurements, it is possible to perform a 3D analysis of the coherent structures. Three methods are usually employed to visualize vortices: isosurfaces of axial velocity, isosurfaces of axial vorticity and isosurfaces calculated with the λ_2 technique (method developed in [80]). Figure 5.12 shows the coherent structures obtained following these

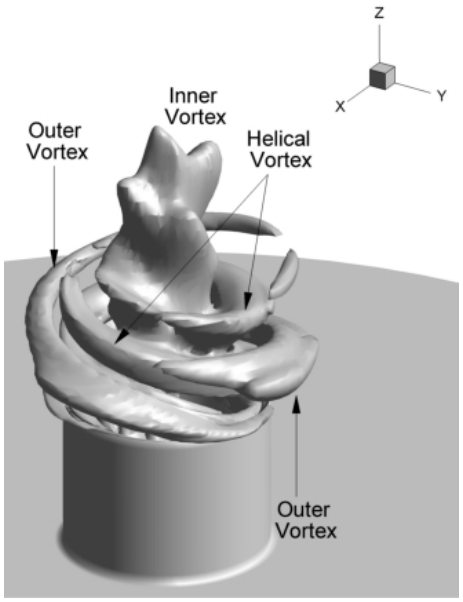

(a) λ_2 technique

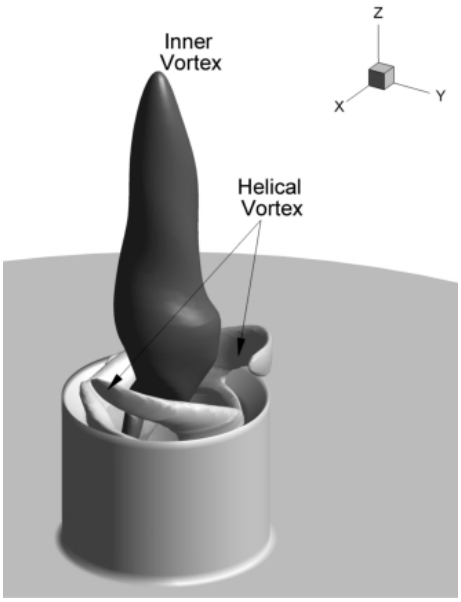

(b) axial velocity, $u_z = -5\ m/s$ (dark) and $u_z = 10\ m/s$ (bright)

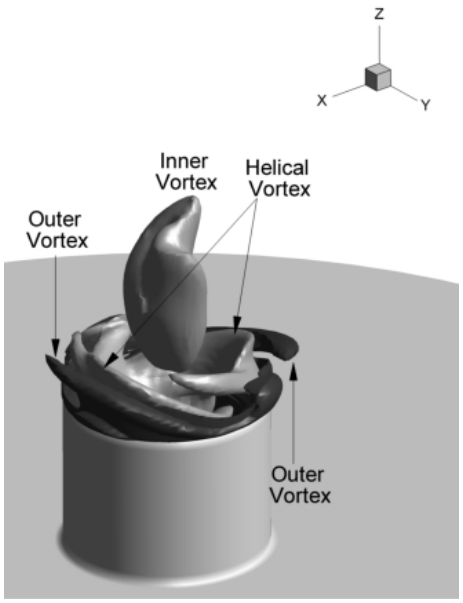

(c) axial vorticity, $\omega_z = 2500\ 1/s$ (dark) and $\omega_z = -2500\ 1/s$ (bright)

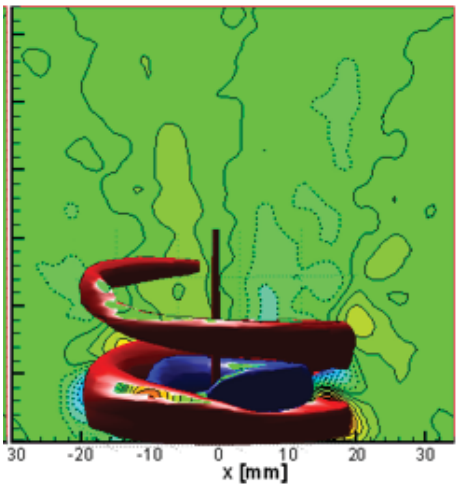

(d) extrapolated representation of azimuthal isovorticity

Figure 5.12: Isosurfaces for the high swirl case and RSM. (a)-(c) are numerical and (d) is an experimental reconstruction.

three methods. Figure 5.12a represents the outcome of the λ_2 technique, in which vortices are defined as a connected region with two negative eigenvalues of $S^2 + \Omega^2$, S and Ω being the symmetric and antisymmetric parts of the velocity gradient tensor, respectively. The isosurface has a value $\lambda_2 = -10$ expressed in $(D_o/u_o)^2$ units. Figures 5.12a and 5.12c represent isosurfaces of axial velocity and vorticity respectively.

Three sets of coherent structures can be clearly distinguished in Figures 5.12a and 5.12c: an inner recirculation zone, an inner helical vortex that can be treated as two spiral vortices (the so-called precessing vortex cores), and other two outer spiral vortices formed with the surrounding flow. When only axial velocity is considered, Figure 5.12b, isosurfaces lack the inner recirculation zone. These results appreciably resemble those found experimentally and numerically in [73, 138, 20, 52, 157, 158]. In these series of works, several types of flow structures are observed and related to large turbulence intensities, and it is claimed that those structures could be generated by the Kelvin-Helmholtz instability. In addition, the influence of PVC over IRZ explains the distorted shape of the latter. All these interactions generate velocity and pressure instabilities which can be easily monitored [118].

The complexity of the CS shown in Figure 5.12 is also manifest in other aspects of the numerical results. Recalling Figure 5.8, we note that monitoring point P1 is located close to the nozzle outlet, a position where the two inner spiral vortices would pass. Then, the two frequency peaks numerically predicted could be identified as follows: $479\ Hz$ is the fundamental frequency that is detected in remote places P_{ac}, , at which the set of CS rotates, while $750\ Hz$ indicates the

passage of two vortices, almost, but not exactly, at doubled rotation speed. Similar results were obtained by Fernandes et al. [41].

Finally, Figure 5.12d shows the reconstruction of spiral vortices by Legrand et al. [95] based on their 2D POD analysis of experimental data in the same geometry and conditions. Although both flows resemble each other very much, there is an important difference. Based on their reconstruction, authors claim that only two spiral vortices are generated, an inner spiral vortex which is formed inside the nozzle and another one formed with surrounding air.

Chapter 6

Summary and conclusions

Numerical studies of unsteady isothermal, single-phase turbulent flow in a pilot scale pulverized-fuel swirl combustor and an atmospheric low swirl burner have been completed using the standard $k-\epsilon$ and Reynolds stress turbulence models. Special care has been taken to assure numerical accuracy, grid independence and far-field representation. For this class of simulations, also the exact representation of the inlet devices reveals itself specially important. The numerical computation converges to oscillatory solutions for all analyzed cases, thus offering the possibility of advanced modeling of flow pulsation and instability, at a relatively low numerical cost.

6.1 General conclusions

The main advantage of URANS schemes is the low computational cost, since they require far lower spatial and temporal resolution than LES. In addition, it has been

demonstrated that few snapshots are enough in URANS to get a reliable numerical approximation of a realistic pulsating flow.

One of the important issues in numerical simulations is the influence of the mesh on the accuracy of the solution. The grid convergence index (GCI) has been used to estimate the uncertainty associated with numerical errors. This analysis of the error on the solution confirmed that meshes have been constructed adequately.

With the help of advanced post-processing techniques, the coherent structures that appear in the flow have been identified. These techniques allow to observe that the coherent structures rotate around the axial axis. The basic types of coherent structures that have been observed in the confined swirl burner are a bubble-type recirculation zone and a spiral-type structure that surrounds. While for the flow of the unconfined swirl burner, a bubble-type recirculation zone and a helical-type structure that surrounds have been observed. The instabilities produced by coherent structures have been analyzed with the fast Fourier transform of the static pressure and velocity monitors.

6.2 Effect of inlet and outlet boundary conditions

Special emphasis in the influence of the position of boundary conditions was considered in two burners (confined swirl burner and atmospheric swirl burner). For the analysis, 3D numerical simulations were run under turbulent and isothermal conditions of a single-phase fluid. Two configurations were considered for the inlet conditions: a domain with swirler and a domain without swirler but including correspondent velocity profiles.

The results showed that coherent structures were maintained in the two burners. But, only in the atmospheric swirl burner case, the mean of the axial velocity and the frequency peaks obtained by means of the estimation of power spectral density of the static pressure monitors gave the same value independently of the type of inlet condition. This means that the instabilities produced by vortex breakdown in atmospheric burners propagate downstream and never downstream. In the case of the confined swirl burner, the instabilities propagates in all directions.

It is worth mentioning that the position of the outlet boundary condition was also analyzed. Although the influence is less compared with the inlet condition, an optimal distance was found where the effect of the outlet boundary condition was minimal.

6.3 Comparison of the $k - \epsilon$ and Reynolds stress turbulence models

The simulated flow has been studied by several methods of post-processing, including advanced techniques for eduction of vortical coherent structures, also with the objective of comparing the performance of the two turbulence closures. Both give realistic predictions; they describe a complex, and quasi-periodic flow with spiral and helical vortexes that conform a precessing vortex core and a pulsating inner recirculation zone. This behaviour is captured by the monitors. For the confined swirl burner, when these signals are processed by FFT, the frequency

peak predicted by the $k-\epsilon$ model differs in a 35% compared with the prediction of the RSM, where the frequency peaks are stronger. Results are quite convincing and compare reasonably with the experimental literature. Particularly realistic is the prediction via RSM, for which the flow lacks exact symmetry and periodicity, and exhibits more stronger and persistent vertical motions. In contrast, albeit with essentially the same features, the $k-\epsilon$ model leads to a flow of more schematic nature.

For the atmospheric swirl burner, the mean velocity showed that both models predict values close to the experimental measurements. For the low swirl case, the axial velocity adjusts better for the experimental data with the RSM compared with the $k-\epsilon$ model while for the tangential velocity the $k-\epsilon$ model gives a better approximation. For the high swirl case, the axial and tangential velocities adjust better with the $k-\epsilon$ model. With respect to the time series, they showed a similar behavior present in the confined burner, namely, the signals are periodic. For this case, the frequency peaks were validated with experimental data where the difference of the numerical simulation and experimental data differ only in 4.4%.

6.4 Coherent structures eduction

Actually, there are different techniques to identify the coherent structures present in a turbulent flow. For this thesis, two common techniques (velocity and vorticity isosurfaces) and one advanced visualization technique (λ_2) were considered. In all techniques, it was possible identify the recirculation zones, spiral vortex, helical

vortex and some spiral and toroidal structures that form around the main flow. However, due to the complexity of coherent structures and the interaction each other, only the λ_2 technique was able to capture with enough clarity all the structures including those weak structures. Velocity and vorticity isosurfaces are incapable to detect these weak structures.

More importantly, the coherent structures predicted by the two turbulence models have great differences when they are analyzed by λ_2 technique. The coherent structures given by $k-\epsilon$ model are weak compared with the RSM which indicates that they dissipate quickly. By the other hand, the RSM capture many details of the coherent structures presents in the flow, i. e., the inner recirculation zone (IRZ) which is distorted by the precessing vortex core (PVC).

6.5 Comparison of numerical simulation with S-PIV

Exhaustive numerical simulations of the swirling turbulent flow experimentally characterized by S-PIV by Legrand et al. [95] have been presented, under the premise of detecting pulsating phenomena, vortex breakdown and coherent structures, and investigating the usefulness of economic URANS methods in this context. Comparing the numerical results obtained by RSM with the experimental S-PIV measurements, it can be concluded that the turbulence model is able to predict the same number of cores.

The numerical flow resembles very much the experimental one, and duplicates its features. Average flow, pulsating frequency and vortex intensities are adequately predicted. The utility of URANS computations for simulating complex

flows is evident, at least as a complementary tool together with experimental measurement, since they produce all the necessary information to construct 3D coherent structures within an acceptable approximation.

6.6 Perspectives for future work

Aside from rigorous experimental validation in the model combustor, future work will be centered on elucidating the essential balance of an URANS simulation: economy of the turbulence model vs. quality of the prediction. To this end, the URANS scheme for the flow will be coupled with a second phenomena, such as turbulent dispersion of particles, density variation through temperature gradients or species mixture, or density variation through simple models of partially premixed gas combustion.

From a point of view of post-processing techniques, classical spectral analysis generally uses fast Fourier transform (FFT) which is a common tool in practical applications. However, fast Fourier transform fails in the processing of short data sequences. In other words, fast Fourier transform is not capable to capture very low frequency peaks. But now, various other approaches are available: autoregressive (AR), moving average (MA) and autoregressive moving average (ARMA) methods. These methods, developed for radar, sonar of geophysical applications, etc. are not well known for fluid mechanics and combustion applications. The advantage of the use of modern spectral methods is that very low frequency peaks could be obtained, adding frequency resolution and statistical stability to the current information.

Chapter 7

Conclusiones

Estudios numéricos de flujo inestable, isotérmico, monofásico, turbulento en un quemador piloto de combustible pulverizado de giro inducido y en un quemador atmosférico de bajo giro inducido han sido realizados usando los modelos $k - \epsilon$ estándar y el modelo de esfuerzos de Reynolds. Se ha tenido especial cuidado en asegurar precisión numérica, independencia de malla y una adecuada representación del campo lejano. También, la exacta representación de los dispositivos de entrada revela que es especialmente importante para éste tipo de simulaciones. Los cálculos numéricos convergen a una solución oscilatoria para todos los casos analizados, ofreciendo así la posibilidad de un modelado avanzado de flujo pulsante e inestable a un costo numérico relativamente bajo.

7.1 Conclusiones Generales

La principal ventaja de los esquemas URANS es el bajo coste computacional, debido a que estos requieren de menos resolución temporal y espacial que el que necesita LES. Además, se ha demostrado que las URANS necesitan de pocas instantáneas para obtener una aproximación numérica confiable de un flujo pulsante. Uno de los aspectos importante en las simulaciones numéricas es la influencia de la malla sobre la precisión de la solución. El índice de convergencia de malla ha sido usado para estimar la incertidumbre asociada con los errores numéricos. Este análisis de error confirma que la mala ha sido construida adecuadamente.

Con la ayuda de técnicas avanzadas de post-proceso, las estructuras coherentes presentes en el flujo han sido identificadas. Estas técnicas permiten observar que las estructuras coherentes rotan alrededor del eje axial. Los tipos básicos de estructuras coherentes que han sido observadas para el caso del quemador confinado de giro inducido son: una zona de recirculación del tipo burbuja y una estructura del tipo espiral que la envuelve. Mientras que para el flujo del quemador atmosférico de giro inducido se ha observado una zona de recirculación del tipo burbuja y una estructura del tipo helicoidal que la envuelve. Las inestabilidades producidas por estas estructuras han sido analizadas mediante la transformada rápida de Fourier de los monitores de presión estática y de velocidad.

7.2 Efecto de las condiciones de contorno de entrada y de salida

Fue puesto especial énfasis en la influencia de la posición de las condiciones de contorno en ambos quemadores. Para el análisis, simulaciones en 3D fueron ejecutadas bajo condiciones turbulentas e isotérmicas de un flujo monofásico. Fueron consideradas dos configuraciones para las condiciones de entrada: un dominio con el generador de giro y un dominio sin generador de giro pero con sus correspondientes perfiles de velocidades.

Los resultados mostraron que las estructuras coherentes fueron mantenidas en ambos quemadores. Pero, solamente en el caso del quemador atmosférico de giro inducido, el promedio de la velocidad axial y los picos de frecuencia obtenidos mediante la estimación de la densidad de potencia espectral de los monitores de presión estática dieron el mismo resultado independientemente del tipo de condición de entrada. Esto significa que las inestabilidades producidas por el rompimiento de vórtice en los quemadores atmosféricos se propagan aguas abajo y nunca aguas arriba, En el caso del quemador confinado de giro inducido, las inestabilidades se propagan en todas direcciones.

Es importante mencionar que la posición de la condición de contorno de salida también fue analizada. Aunque su influencia es menor comparada con la condición de entrada, se encontró una distancia óptima donde el efecto de la condición de salida fuera mínimo.

7.3 Comparación de los modelos $k-\epsilon$ y esfuerzos de Reynolds

El flujo simulado ha sido estudiado mediante varios métodos de post-proceso, incluyendo técnicas avanzadas para la educción de estructuras vorticiales coherentes, con el objetivo de comparar el desempeño de los dos modelos de turbulencia. Ambos modelos proporcionan predicciones realistas; describen un flujo complejo, casi-periódico con vórtices espirales y helicoidales que confirman una precesión de núcleo de vórtice y una zona de recirculación pulsante. Este comportamiento es capturado por los puntos de monitorización. Para el quemador confinado de giro inducido, cuando las señales son procesadas por FFT, el pico de frecuencia que predice el modelo $k-\epsilon$ estándar es distinto en un 35% comparado con la estimación del RSM, donde el pico de frecuencia es, además, más fuerte. Los resultados son muy convincentes y se comparan razonablemente bien con la literatura experimental. Resulta particularmente realista la predicción hecha por RSM, para el cual el flujo carece de simetría y periodicidad exacta, y exhibe movimientos verticales más fuertes y persistentes. En contraste, aunque con esencialmente las mismas características, el modelo $k-\epsilon$ estándar lleva a un flujo de naturaleza más esquemática.

Para el quemador atmosférico de giro inducido, el promedio de la velocidad mostró que ambos modelos predicen valores cercanos a las mediciones experimentales. Para el caso de giro inducido bajo, la velocidad axial ajusta mejor para los datos experimentales con el RSM si se compara con el modelo $k-\epsilon$ estándar,

mientras que para la velocidad tangencial, el modelo $k - \epsilon$ estándar proporciona una mejor aproximación. Para el caso de giro inducido alto, las velocidades axial y tangencial ajustan mejor con el modelo $k - \epsilon$ estándar. En lo que respecta a las series temporales, estos muestran un comportamiento similar al que está presente en el quemador de flujo confinado, es decir, las señales son periódicas. Para este caso, los picos de frecuencia fueron validados con datos experimentales donde la diferencia de la simulación numérica y los datos experimentales difieren solamente en un 4.4%.

7.4 Educción de estructuras coherentes

Actualmente, existen diferentes técnicas para identificar las estructuras coherentes presentes en un flujo turbulento. Para esta tesis, dos técnicas comunes (isosuperficies de velocidad y vorticidad) y una técnica de visualización avanzada (λ_2) fueron consideradas. Con todas las técnicas, fue posible identificar las zonas de recirculación, los vórtices en espiral, los vórtices helicoidales y algunas estructuras espirales y toroidales que forman alrededor del flujo principal. Sin embargo, debido a la complejidad de las estructuras coherentes y a su interacción entre ellas, solamente la técnica λ_2 fue capaz de mostrar con suficiente claridad todas las estructuras incluyendo las estructuras débiles. Las isosuperficies de velocidad y vorticidad no son capaces de detectar estas estructuras débiles. Las estructuras coherentes que se predicen mediante los dos modelos de turbulencia tienen grandes diferencias cuando son analizadas por la técnica λ_2. Las estructuras coherentes dadas por el modelo $k - \epsilon$ estándar son débiles en comparación con

el modelo RSM. Por otro lado, el modelo RSM captura mejor los detalles de las estructuras coherentes presentes en el flujo, por ejemplo, la zona de recirculación interna la cual es deformada por la precesión de núcleo de vórtice (PVC).

7.5 Comparación de la simulación numérica con el S-PIV

Simulaciones numéricas exhaustivas del flujo turbulento caracterizado mediante S-PIV por Legrand et al. [95] han sido presentados, bajo la premisa de la detección del fenómeno pulsante, rompimiento de vórtice y estructuras coherentes, y la investigación de la utilidad de los métodos económicos URANS en este contexto. Comparando los resultados numéricos obtenidos por RSM con las mediciones experimentales S-PIV, puede concluirse que el modelo de turbulencia es capaz de predecir el mismo número de núcleos. El flujo obtenido por medios numéricos se asemeja mucho al experimental, duplicando sus características. Flujo promedio, frecuencia pulsante y la intensidad de vórtices son adecuadamente predichos. La utilidad de los cálculos URANS para simular flujos complejos es evidente al menos en el uso como una herramienta complementaria de las mediciones experimentales, ya que producen toda la información necesaria para construir estructuras coherentes en 3D dentro de una aproximación aceptable.

7.6 Perspectivas para el trabajo futuro

Además de la validación experimental rigurosa en el modelo del quemador, el trabajo futuro deberá estar centrado en dilucidar el balance esencial de una simulación URANS: economía del modelo de turbulencia vs. calidad de la predicción. Para este fin, los esquemas URANS para el flujo se acoplarán con un segundo fenómeno, como lo puede ser la dispersión turbulenta de partículas, la variación de la densidad por medio de gradientes de temperatura o mezcla de especies, o la variación de la densidad por medio de modelos simples de combustión de gas parcialmente premezclado. Desde un punto de vista de técnicas de post-proceso, el análisis espectral clásico usa la transformada rápida de Fourier la cual es una herramienta común en aplicaciones prácticas. Sin embargo, la FFT falla en el proceso de secuencias de datos cortas. En otras palabras, la transferencia rápida de Fourier no es capaz de capturar los picos de muy baja frecuencia. Pero ahora, varias aproximaciones alternativas están disponibles: método autoregresivo (AR), método de media móvil (MA) y el método autoregresivo de media móvil (ARMA). Estos métodos, desarrollados para aplicaciones geológicas y geofísicas de radar y sonar no son del todo conocidos en el campo de la mecánica de fluidos y ni tampoco en las aplicaciones de combustión. La ventaja del uso de los métodos espectrales modernos es que se podrían obtener los picos de muy baja frecuencia, añadiendo resolución y estabilidad estadística a la información que se tiene.

Appendix A

Basic concepts of turbulent swirling flows

A.1 Characteristic Turbulent Time and Length Scales

Turbulent flows are characterized by the existence of a multitude of eddies of different sizes. This is due to the energy of turbulent flows is dissipated by the break up of large eddies into smaller eddies which in turn break up into even smaller eddies. This process continues until viscous forces start to dominate and the smallest eddies are dissipated. This so–called eddy cascade hypothesis goes back to Kolmogorov's theory for homogeneous, isotropic turbulence. It states that a stationary energy transfer from the large eddies down to the smallest eddies occurs in the so-called *inertial subrange* of turbulence. This energy transfer is local in the sense that energy from one eddy is transferred only to the eddy of

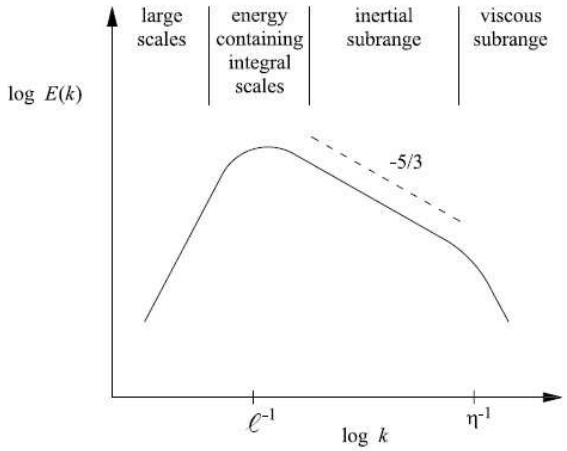

Figure A.1: Energy Spectrum of Homogeneous, Isotropic Turbulence [117].

the next smaller length scale. Because of the locality of the energy transfer, the energy transfer rate, i.e. the kinetic energy per eddy turnover time, is independent of the length scale of the eddies and thus constant within the inertial subrange. This scale invariance is the most important hypothesis for large Reynolds number flows. It is integrated into every standard turbulence model, thereby satisfying the requirement of Reynolds number independence in the Reynolds number limit, and a model for turbulent combustion should also abide by this premise.

The energy spectrum $E(k)$ of the homogeneous, isotropic turbulence as a function of the reciprocal of the eddy size, the wave number k, is shown in Fig. A.1. The constant energy transfer rate in the inertial subrange leads to a slope of -5/3, which results from dimensional analysis.

Two important characteristic turbulent length scales bounding the inertial subrange can also be identified in this figure, the Kolmogorov length scale η and

the integral length scale ℓ.

The Kolmogorov length scale η denotes the scale of the smallest eddies. At this length scale, viscous forces dominate, thereby converting the kinetic energy of the smallest eddies into thermal energy. The Kolmogorov length scale thus has to be a function of the kinematic viscosity ν and the kinetic energy dissipation rate ϵ. It can be determined by dimensional analysis

$$\eta = \left(\frac{\nu^3}{\epsilon}\right) \tag{A.1}$$

In addition, the kolmogorov time scale t_η, which is proportional to the turnover time of a Kolmogorov eddy, can be calculated by dimensional analysis

$$t_\eta = \sqrt{\frac{\nu^3}{\epsilon}} \tag{A.2}$$

Combining (A.1) and (A.2), the turnover velocity of a Kolmogorov eddy can be defined as

$$v_\eta = (\nu\epsilon)^{1/4} \tag{A.3}$$

The integral length scale ℓ corresponds to the length scale of those eddies that contain the most energy. The integral length scale ℓ can be defined with the help of the normalized two-point correlation function

$$R(x,r) = \frac{\overline{v'(x,t)v'(x+r,t)}}{\sqrt{\overline{v'^2(x,t)}}\sqrt{\overline{v'^2(x+r,t)}}} \tag{A.4}$$

depicted in Fig. A.2. The quantity R is a measure for the correlation of the velocity fluctuations v' measured at the points x and $x+r$, thereby indicating to what degree the turbulent properties of two points with distance r influence each other. The velocity correlation function is equal to unity in the limit of $r \to 0$ and decreases asymptotically to zero for large r. The integral length scale is defined by means of (A.4),

$$\ell = \int_0^\infty R(x,r)dr \tag{A.5}$$

In Fig. A.2, ℓ is located where the shaded areas above and below the two-point velocity correlation function are of equal size. Hence, the integral length scale ℓ can be interpreted as the length scale from which point on the velocity fluctuations are predominantly uncorrelated.

In addition, the integral time scale τ, which is proportional to the turnover time ℓ/v' of an integral eddy, can be defined as

$$\tau = \frac{k}{\epsilon} \tag{A.6}$$

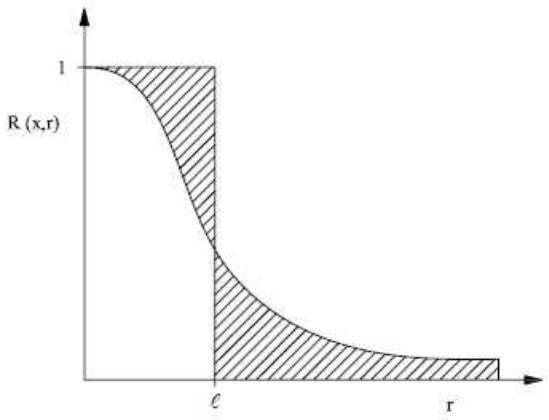

Figure A.2: The Normalized Two-Point Velocity Correlation Function

where the turbulent kinetic energy k is defined by

$$k = \frac{1}{2}\overline{v'v'} \tag{A.7}$$

Due to the constant energy transfer rate in the inertial subrange, the kinetic energy dissipation rate ϵ in (A.6) is equal to the kinetic energy rate ϵ^* fed into the energy cascade at the integral length scale, Fig. A.1. This kinetic energy rate ϵ^* can be determined by

$$\epsilon = \epsilon^* \sim O\left(\frac{v'^3}{\ell}\right) \tag{A.8}$$

A.2 Governing equations

In a turbulent flow, the velocity field $\mathbf{U}(\mathbf{x}, t)$ is random. The Navier-Stokes equations apply equally to turbulent flows, but here the aim of theory must be different. Since $\mathbf{U}$ is a random variable, its value is inherently unpredictable. A theory that predicts a particular value for $\mathbf{U}$ is almost certain to be wrong. In 1894, Reynolds derived the most basic equations that govern the mean velocity field $\langle \mathbf{U}(\mathbf{x}, t) \rangle$.

The decomposition of the velocity $\mathbf{U}(\mathbf{x}, t)$ into its mean $\langle \mathbf{U}(\mathbf{x}, t) \rangle$ and the fluctuation

$$\mathbf{u}(\mathbf{x}, \mathbf{t}) \equiv \mathbf{U}(\mathbf{x}, t) - \langle \mathbf{U}(\mathbf{x}, t) \rangle \tag{A.9}$$

is referred to as the *Reynolds decomposition*, i.e.,

$$\mathbf{U}(\mathbf{x}, t) = \langle \mathbf{U}(\mathbf{x}, t) \rangle + \mathbf{u}(\mathbf{x}, \mathbf{t}) \tag{A.10}$$

It follows from the continuity equation and by subtraction

$$\nabla \mathbf{u} = 0 \tag{A.11}$$

For the momentum equation, the first step is to write the substantial derivate

in conservative form,

$$\frac{DU_j}{Dt} = \frac{\partial U_j}{\partial t} + \frac{\partial}{\partial x_i}(U_i U_j) \tag{A.12}$$

so that the mean is

$$\left\langle \frac{DU_j}{Dt} \right\rangle = \frac{\partial \langle U_j \rangle}{\partial t} + \frac{\partial}{\partial x_i} \langle U_i U_j \rangle \tag{A.13}$$

Then, substituting the Reynolds decomposition for U_i and U_j, the nonlinear term becomes

$$\langle U_i U_j \rangle = \langle U_i \rangle \langle U_j \rangle + \langle u_i u_j \rangle \tag{A.14}$$

The velocity covariances $\langle u_i u_j \rangle$ are called Reynolds stresses. From the previous equations,

$$\left\langle \frac{DU_j}{Dt} \right\rangle = \frac{\partial \langle U_j \rangle}{\partial t} + \langle U_i \rangle \frac{\partial \langle U_j \rangle}{x_i} + \frac{\partial}{\partial x_i} \langle u_i u_j \rangle \tag{A.15}$$

Defining the mean substantial derivate as

$$\frac{\bar{D}}{\bar{D}t} \equiv \frac{\partial}{\partial t} + \langle \mathbf{U} \rangle \cdot \nabla \tag{A.16}$$

For any property $Q(\mathbf{x}, t)$, $\bar{D}Q/\bar{D}t$ represent its rate of change following a point moving with the local mean velocity $\langle \mathbf{U}(\mathbf{x}, t) \rangle$.

Based on this analysis, the mean-momentum or Reynolds equations are

$$\frac{\bar{D} \langle U_j \rangle}{\bar{D}t} = \nu \nabla^2 \langle U_j \rangle - \frac{\partial \langle u_i u_j \rangle}{\partial x_i} - \frac{1}{\rho} \frac{\partial \langle p \rangle}{\partial x_j} \tag{A.17}$$

In appearance, the Reynolds equations and the Navier-Stokes equations are the same, except for the term in the Reynolds stresses.

A.3 The $k - \epsilon$ Model

The $k - \epsilon$ model [91], belongs to the class of two-equation models. The objective of the $k - \epsilon$ model is to provide a closure for the Reynolds stress tensor $\partial \langle u_i u_j \rangle$ and the turbulent transport terms in the averaged Navier-Stokes equations at the integral length scale ℓ.

In addition to the turbulent viscosity hypothesis, the $k - \epsilon$ model consists of: the model transport equation for k, the model transport equation for ϵ and the specification of the turbulent viscosity as

$$\nu_T = C_\mu k^2/\epsilon \tag{A.18}$$

where $C_\mu = 0.09$.

The transport equation for k is

$$\frac{\bar{D}k}{\bar{D}t} = -\nabla \cdot \mathbf{T}' + \mathcal{P} - \epsilon \tag{A.19}$$

where $\mathcal{P}$ is the rate of production of turbulent kinetic energy and $\mathbf{T}'$ is

$$T_i' = \frac{1}{2}\left\langle u_i u_j u_j \right\rangle + \left\langle u_i p' \right\rangle/\rho - 2\nu \left\langle u_i s_{ij} \right\rangle \tag{A.20}$$

The transport equation for ϵ is

$$\frac{\bar{D}\epsilon}{\bar{D}t} = \nabla \cdot \left(\frac{\nu_T}{\sigma_\epsilon}\nabla\epsilon\right) + C_{\epsilon 1}\frac{\mathcal{P}\epsilon}{k} - C_{\epsilon 2}\frac{\epsilon^2}{k} \tag{A.21}$$

Standard $k-\epsilon$ model generally use the model constants $C_\mu = 0.09$, $C_{\epsilon 1} = 1.44$, $C_{\epsilon 2} = 1.92$, $\sigma_k = 1.0$ and $\sigma_\epsilon = 1.3$.

The $k-\epsilon$ model assumes local isotropy of the fluctuating quantities and directly resolves only processes at length scales larger than the integral length scale ℓ. For flows where significant anisotropy exists, the assumption of local isotropy is

inadequate. Furthermore, important turbulent structures may be damped due to the high turbulent viscosity.

A.4 Reynolds Stress Model

The Reynolds stress model (RSM) abandons the isotropic eddy-viscosity hypothesis and closes the Reynolds-averaged Navier-Stokes equations by solving transport equations for the Reynolds stress, together with an equation for the dissipation rate [90, 88]. This means that seven additional transport equations must be solved. It allows to account the effects of streamline curvature, swirl, rotation, and rapid changes in strain rate in a more rigorous manner than two-equation models. However, the fidelity of RSM predictions is still limited by the closure assumptions employed to model various terms in the exact transport equations for the Reynolds stress. The modeling of the pressure-strain and dissipation-rate terms is often to be responsible for compromising the accuracy of RSM predictions.

The RSM might not always yield results that are clearly superior to the simpler models in all classes of flows to warrant the additional computational expense. However, use of the RSM is a must when the flow features of interest are the result of anisotropy in the Reynolds stress (swirling flows).

The exact form of the Reynolds stress transport equation may be derived by taking moments of the exact momentum equation. This is a process wherein the exact momentum equations are multiplied by a fluctuating property, the product then being Reynolds-averaged. But, several of the terms in the exact equation are unknown and modeling assumptions are required in order to close the equations.

The modeled transport equations of Reynolds stress can be written in the following form.

$$\frac{\bar{D}}{\bar{D}t}\left\langle u_i u_j\right\rangle + \frac{\partial}{\partial x_k}\left(\underbrace{\left\langle u_i u_j u_k\right\rangle + \frac{1}{\rho}\left\langle u_i p'\right\rangle \delta_{jk} + \frac{1}{\rho}\left\langle u_j p'\right\rangle \delta_{ik} - \nu\frac{\partial\left\langle u_i u_j\right\rangle}{\partial x_k}}_{\mathcal{T}_{kij}}\right) = \underbrace{-\left\langle u_i u_k\right\rangle \frac{\partial\left\langle U_j\right\rangle}{\partial x_k} - \left\langle u_j u_k\right\rangle \frac{\partial\left\langle U_i\right\rangle}{\partial x_k}}_{\mathcal{P}_{ij}} + \underbrace{\left\langle \frac{p'}{\rho}\left(\frac{\partial u_i}{\partial x_j} + \frac{\partial u_j}{\partial x_i}\right)\right\rangle}_{\mathcal{R}_{ij}} - \underbrace{2\nu\left\langle \frac{\partial u_i}{\partial x_k}\frac{\partial u_j}{\partial x_k}\right\rangle}_{\epsilon_{ij}} \tag{A.22}$$

where $\mathcal{T}_{kij}$ is the Reynolds-stress flux, $\mathcal{P}_{ij}$ is the production tensor, $\mathcal{R}_{ij}$ the pressure-rate-of-strain tensor and ϵ_{ij} is the dissipation tensor.

The pressure-rate-of-strain term, $\mathcal{R}_{ij}$, in Equation A.22 is modeled according to the proposals by Gibson and Launder [58], Fu et al. [48] and Launder [88, 89]. The approach modeling $\mathcal{R}_{ij}$ uses the following decomposition:

$$\mathcal{R}_{ij} = \mathcal{R}_{ij,1} + \mathcal{R}_{ij,2} + \mathcal{R}_{ij,W} \tag{A.23}$$

where $\mathcal{R}_{ij,1}$ is the slow pressure-strain terms, also known as the return-to-isotropy term, $\mathcal{R}_{ij,2}$ is called the rapid pressure-strain term, and, $\mathcal{R}_{ij,W}$ is the wall-reflection term.

The low pressure-strain term, $\mathcal{R}_{ij,1}$, is modeled as

$$\mathcal{R}_{ij,1} \equiv -C_1\rho\frac{\epsilon}{k}\left[\left\langle u_i u_j\right\rangle - \frac{2}{3}\delta_{i,j}k\right] \tag{A.24}$$

with $C_1 = 1.8$.

The rapid pressure-strain term, $\mathcal{R}_{ij,2}$, is modeled as

$$\mathcal{R}_{ij,2} \equiv -C_2 \left[\mathcal{P}_{ij} - \frac{2}{3}\delta_{i,j}\mathcal{P}_k \right] \tag{A.25}$$

The redistribution of normal stresses near the wall, $\mathcal{R}_{ij,W}$, is modeled as

$$\mathcal{R}_{ij,W} \equiv -2C_1^{'}\frac{\epsilon}{k}\left\langle u_n^2 \right\rangle f + C_1^{'}\frac{\epsilon}{k}\left\langle u_n^2 \right\rangle f \tag{A.26}$$

where $f = \frac{k^{\frac{3}{2}}}{2.55 x_n \epsilon}$, $C_1^{'} = 0.5$ and n is the normal coordinate to the wall.

Bibliography

[1] V. Alekseenko, S., V. Bilsky, A., M. Dulin, V., and M. Markovich, D. Experimental study of an impinging jet with different swirl rates. *International Journal of Heat and Fluid Flow*, 28(6):1340–1359, 2007.

[2] V. Alekseenko, S., M. Dulin, V., S. Kozorezov, Y., and M. Markovich, D. Effect of axisymmetric forcing on the structure of a swirling turbulent jet. *International Journal of Heat and Fluid Flow*, 29(6):1699–1715, 2008.

[3] V. Alekseenko, S., A. Kuibin, P., L. Okulov, V., and I. Shtork, S. Helical vortices in swirl flow. *J. Fluid Mech.*, 382:195–243, 1999.

[4] J. Ali, M. and V. Georgios, H. Reynolds stress model in the prediction of confined turbulent swirling flows. *Journal of Fluids Engineering*, 128(6):1377–1382, 2006.

[5] V. Apte, S., K. Mahesh, P. Moin, and C. Oefelein, J. Large-eddy simulation of swirling particle-laden flows in a coaxial-jet combustor. *Int. J. Multiph.*

Flow, 29(8):1311–1331, 2003.

[6] S. Archer, S., K. Gupta, A., and K. Kitagawa. Spectroscopic examination and analysis of unconfined swirling flames. *J. Korean Phys. Soc.*, 49(1):298–304, 2006.

[7] G. Balarac, O. Metais, and M. Lesieur. Mixing enhancement in coaxial jets through inflow forcing: A numerical study. *Physics of Fluids*, 19(7):075102–17, 2007.

[8] G. Balarac and M. Si-Ameur. Mixing and coherent vortices in turbulent coaxial jets. *Comptes Rendus MÃ©canique*, 333(8):622–627, 2005.

[9] E. Barton, I. Comparison of simple- and piso-type algorithms for transient flows. *International Journal for Numerical Methods in Fluids*, 26(4):459–483, 1998.

[10] B. Benjamin, T. Theory of the vortex breakdown phenomenon. *Journal of Fluid Mechanics Digital Archive*, 14(04):593–629, 1962.

[11] A. Berger, S. and G. Erlebacher. Vortex breakdown incipience: Theoretical considerations. *Physics of Fluids*, 7(5):972–982, 1995.

[12] F. Biagioli and F. Güthe. Effect of pressure and fuel-air unmixedness on nox emissions from industrial gas turbine burners. *Combustion and Flame*, 151(1-2):274–288, 2007.

[13] F. Biagioli, F. Güthe, and B. Schuermans. Combustion dynamics linked to flame behaviour in a partially premixed swirled industrial burner. *Experimental Thermal and Fluid Science*, 32(7):1344–1353, 2008.

[14] P. Billant, M. Chomaz, J., and P. Huerre. Experimental study of vortex breakdown in swirling jets. *J. Fluid Mech.*, 376:183–219, 1998.

[15] T. Broeckhoven, M. Brouns, J. Vanherzeele, S. Vanlanduit, and Ch. Lacor. Piv measurements of a double annular jet for validation of numerical simulations. In *13th Int Symp on Applications of Laser Techniques to Fluid Mechanics*, Lisbon, Portugal, 2006.

[16] L. Brown, G. and M. Lopez, J. Axisymmetric vortex breakdown. part 2. *J. Fluid Mech.*, 221:553–576, 1990.

[17] C. Brücker. Study of vortex breakdown by particle tracking velocimetry (ptv) .2. spiral-type vortex breakdown. *Exp. Fluids*, 14(1-2):133–139, 1993.

[18] C. Brücker and W. Althaus. Study of vortex breakdown by particle tracking velocimetry (ptv) .1. bubble-type vortex breakdown. *Exp. Fluids*, 13(5):339–349, 1992.

[19] C. Brücker and W. Althaus. Study of vortex breakdown by particle tracking velocimetry (ptv) part 3: Time-dependent structure and development of breakdown-modes. *Experiments in Fluids*, 18(3):174–186, January 1995.

[20] E. Cala, C., C. Fernandes, E., V. Heitor, M., and I. Shtork, S. Coherent structures in unsteady swirling jet flow. *Exp. Fluids*, 40(2):267–276, 2006.

[21] B. Celik, I., U. Ghia, J Roache, P., and J. Freitas, C. Procedure for estimation and reporting of uncertainty due to discretization in cfd applications. *Journal of Fluids Engineering*, 130(7):078001–4, 2008.

[22] R. K. Cheng. Velocity and scalar characteristics of premixed turbulent flames stabilized by weak swirl. *Combustion and Flame*, 101(1-2):1–14, 1995.

[23] R. K. Cheng, D. Littlejohn, W. A. Nazeer, and K. O. Smith. Laboratory studies of the flow field characteristics of low-swirl injectors for adaptation to fuel-flexible turbines. *Journal of Engineering for Gas Turbines and Power*, 130(2):021501–10, 2008.

[24] M. Coats, C. Coherent structures in combustion. *Prog. Energy Combust. Sci.*, 22(5):427–509, 1996.

[25] A. Coghe, G. Solero, and G. Scribano. Recirculation phenomena in a natural gas swirl combustor. *Experimental Thermal and Fluid Science*, 28(7):709–714, 2004.

[26] C. Cortés and A. Gil. Modeling the gas and particle flow inside cyclone separators. *Progress in Energy and Combustion Science*, 33(5):409–452, 2007. ISI Document Delivery No.: 219HU Times Cited: 13 Cited Reference Count: 137 Cortes, Cristobal Gil, Antonia PERGAMON-ELSEVIER SCIENCE LTD.

[27] F. Cozzi and A. Coghe. Behavior of hydrogen-enriched non-premixed swirled natural gas flames. *Int. J. Hydrog. Energy*, 31(6):669–677, 2006.

[28] J. Craft, T. and E. Launder, B. New wall-reflection model applied to the turbulent impiping jet. *AIAA Journal*, 30:2970–2972, 1992.

[29] C. Danielson, G. and Lanczos. Some improvements in practical fourier analysis and their application to x-ray scattering from liquids. *J. Franklin Inst.*, 233:365–380 and 435–452, 1942.

[30] J. J. Derksen, S. Sundaresan, and H. E. A. van den Akker. Simulation of mass-loading effects in gas-solid cyclone separators. *Powder Technology*, 163(1-2):59–68, 2006. ISI Document Delivery No.: 049LM ELSEVIER SCIENCE SA.

[31] P. A. Durbin. A perspective on recent developments in rans modeling. *In: Rodi, W., Fueyo, N. (Eds.), Engineering Turbulence Modelling And Experiments 5*, pages 3–15, 2002.

[32] C. Duwig and L. Fuchs. Large eddy simulation of vortex breakdown/flame interaction. *Physics of Fluids*, 19(7):075103–20, 2007.

[33] M. Escudier. Vortex breakdown: Observations and explanations. *Progress in Aerospace Sciences*, 25(2):189–229, 1988.

[34] M. P. Escudier, J. Borstein, and T. Maxworthy. The dynamics of confined vortices. *Proceedings of the Royal Society of London. Series A, Mathematical and Physical Sciences*, 382(1783):335–360, 1982.

[35] M. P. Escudier and J. J. Keller. Vortex breakdown: a two-stage transition. *Aerodynamics of Vortical Flows in Three Dimensions, Paper 25*, 1983.

[36] M. P. Escudier and J. J. Keller. Recirculation in swirling flow - a manifestation of vortex breakdown. *Aiaa J.*, 23(1):111–116, 1985.

[37] M. P. Escudier, A. K. Nickson, and R. J. Poole. Influence of outlet geometry on strongly swirling turbulent flow through a circular tube. *Physics of Fluids*, 18(12):125103–18, 2006.

[38] M. P. Escudier and N. Zehnder. Vortex-flow regimes. *Journal of Fluid Mechanics Digital Archive*, 115:105–121, 1982.

[39] J. H. Faler and S. Leibovich. Disrupted states of vortex flow and vortex breakdown. *Physics of Fluids*, 20(9):1385–1400, 1977.

[40] J. H. Faler and S. Leibovich. An experimental map of the internal structure of a vortex breakdown. *Journal of Fluid Mechanics Digital Archive*, 86(02):313–335, 1978.

[41] E. C. Fernandes, M. V. Heitor, and S. I. Shtork. An analysis of unsteady highly turbulent swirling flow in a model vortex combustor. *Exp. Fluids*, 40(2):177–187, 2006.

[42] W. Fick, A. J. Griffiths, and T. O'Doherty. Visualisation of the precessing vortex core in an unconfined swirling flow. *Optical Diagnostics in Engineering*, 2(1):19–31, 1997.

[43] F. Flemming, C. Olbricht, B. Wegner, A. Sadiki, J. Janicka, F. Bake, U. Michel, B. Lehmann, and I. Rohle. Analysis of unsteady motion with respect to noise sources in a gas turbine combustor: Isothermal flow case. *Flow Turbulence and Combustion*, 75:3–27, 2005.

[44] M. Freitag and M. Klein. Direct numerical simulation of a recirculating, swirling flow. *Flow, Turbulence and Combustion*, 75:51–66, 2005.

[45] M. Freitag, M. Klein, M. Gregor, D. Geyer, C. Schneider, A. Dreizler, and J. Janicka. Mixing analysis of a swirling recirculating flow using dns and experimental data. *International Journal of Heat and Fluid Flow*, 27(4):636–643, 2006.

[46] J. Fröhlich, M. García-Villalba, and W. Rodi. Scalar mixing and large-scale coherent structures in a turbulent swirling jet. *Flow, Turbulence and Combustion*, 80(1):47–59, 2008.

[47] D. Froud, T. O'Doherty, and N. Syred. Phase averaging of the precessing vortex core in a swirl burner under piloted and premixed combustion conditions. *Combustion and Flame*, 100(3):407–410, 1995.

[48] S. Fu, B. E. Launder, and M. A. Leschziner. Modeling strongly swirling recirculating jet flow with reynolds-stress transport closures. *In Sixth Symposium on Turbulent Shear Flows*, 1987.

[49] F. O. Gallaire, M. Ruith, E. Meiburg, J. M. Chomaz, and P. Huerre. Spiral vortex breakdown as a global mode. *J. Fluid Mech.*, 549:71–80, 2006.

[50] M. Garcia-Villalba and J. Fröhlich. Les of a free annular swirling jet - dependence of coherent structures on a pilot jet and the level of swirl. *International Journal of Heat and Fluid Flow*, 27(5):911–923, 2006.

[51] M. Garcia-Villalba, J. Fröhlich, and W. Rodi. Identification and analysis of coherent structures in the near field of a turbulent unconfined annular swirling jet using large eddy simulation. *Physics of Fluids*, 18(5):055103–17, 2006.

[52] M. Garcia-Villalba, J. Fröhlich, and W. Rodi. Numerical simulations of isothermal flow in a swirl burner. *Journal of Engineering for Gas Turbines and Power*, 129:377–386, 2007.

[53] M. Garcia-Villalba, J. Fröhlich, W. Rodi, O. Petsch, and H. Büchner. Large eddy simulation of flow instabilities in co-annular swirling jets. In *Direct and Large-Eddy Simulation VI*, pages 201–208. 2006.

[54] A. K. Garg and S. Leibovich. Spectral characteristics of vortex breakdown flowfields. *Physics of Fluids*, 22(11):2053–2064, 1979.

[55] T. Gassoumi, K. Guedri, and R. Said. Numerical study of the swirl effect on a coaxial jet combustor flame including radiative heat transfer. *Numerical Heat Transfer Part A-Applications*, 56(11):897–913, 2009. ISI Document Delivery No.: 535ME Times Cited: 0 Cited Reference Count: 27 Gassoumi, Taoufik Guedri, Kamel Said, Rachid TAYLOR & FRANCIS INC.

[56] A. E. German and T. Mahmud. Modelling of non-premixed swirl burner flows using a reynolds-stress turbulence closure. *Fuel*, 84(5):583–594, 2005.

[57] A. Giannadakis, K. Perrakis, and Th Panidis. A swirling jet under the influence of a coaxial flow. *Experimental Thermal and Fluid Science*, 32(8):1548–1563, 2008.

[58] M. N. Gibson and B. E. Launder. Ground effects on pressure fluctuations in the atmospheric boundary layer. *Journal of Fluids Mechanics*, 89:491–511, 1978.

[59] P. Gopalakrishnan, M. K. Bobba, and J. M. Seitzman. Controlling mechanisms for low nox emissions in a non-premixed stagnation point reverse flow combustor. *Proceedings of the Combustion Institute*, 31(2):3401–3408, 2007.

[60] F. F. Grinstein and C. Fureby. Les studies of the flow in a swirl gas combustor. In *30th International Symposium on Combustion*, pages 1791–1798, Chicago, IL, 2004. Combustion Inst.

[61] B. Y. Guo, T. A. G. Langrish, and D. F. Fletcher. Simulation of turbulent swirl flow in an axisymmetric sudden expansion. *Aiaa J.*, 39(1):96–102, 2001.

[62] B. Y. Guo, T. A. G. Langrish, and D. F. Fletcher. Cfd simulation of precession in sudden pipe expansion flows with low inlet swirl. *Appl. Math. Model.*, 26(1):1–15, 2002.

[63] H. Guohui, S. Dejun, Y. Xieyuan, and T. Binggang. Studies on stability and dynamics of a swirling jet. *Acta Mechanica Sinica*, 17(3):237–244, 2001.

[64] A.K. Gupta, Lilley D.G., and Syred N. *Swirl Flows*. Tunbridge Wells, Kent, England, Abacus Press, 1984, 488 p., 1984.

[65] P. Habisreuther, C. Bender, O. Petsch, H. Bucher, and H. Bockhorn. Prediction of pressure oscillations in a premixed swirl combustor flow and comparison to measurements. *Flow Turbulence and Combustion*, 77:147–160, 2006.

[66] M. G. Hall. Vortex breakdown. *Annual Review of Fluid Mechanics*, 4:195–218, 1972.

[67] K. Hanjalic. Will rans survive les? a view of perspectives. *Journal of Fluids Engineering*, 127(5):831–839, 2005.

[68] Y. Hardalupas and A. Selbach. Imposed oscillations and non-premixed flames. *Progress in Energy and Combustion Science*, 28(1):75–104, 2002.

[69] K. Harvey, J. Some observations of the vortex breakdown phenomenon. *Journal of Fluid Mechanics*, 14:585–592, 1962.

[70] M. A. Herrada and R. Fernandez-Feria. On the development of three-dimensional vortex breakdown in cylindrical regions. *Physics of Fluids*, 18(8):084105–15, 2006.

[71] L. Y. Hu, L. X. Zhou, and Y. H. Luo. Large-eddy simulation of the sydney swirling nonpremixed flame and validation of several subgrid-scale models. *Numerical Heat Transfer Part B-Fundamentals*, 53(1):39–58, 2008. ISI Document Delivery No.: 251DR Times Cited: 1 Cited Reference Count: 23 Hu, L. Y. Zhou, L. X. Luo, Y. H. TAYLOR & FRANCIS INC.

[72] L. Y. Hu, L. X. Zhou, and J. Zhang. Large-eddy simulation of a swirling diffusion flame using a som sgs combustion model. *Numerical Heat Transfer Part B-Fundamentals*, 50(1):41–58, 2006. ISI Document Delivery No.: 046ZB Times Cited: 9 Cited Reference Count: 15 TAYLOR & FRANCIS INC.

[73] R. F. Huang and F. C. Tsai. Flow field characteristics of swirling double concentric jets. *Experimental Thermal and Fluid Science*, 25(3-4):151–161, 2001.

[74] R. F. Huang and S. C. Yen. Aerodynamic characteristics and thermal structure of nonpremixed reacting swirling wakes at low reynolds numbers. *Combustion and Flame*, 155(4):539–556, 2008.

[75] Y. Huang and V. Yang. Dynamics and stability of lean-premixed swirl-stabilized combustion. *Progress in Energy and Combustion Science*, 35(4):293–364, August 2009.

[76] G. Iaccarino, A. Ooi, P. A. Durbin, and M. Behnia. Reynolds averaged simulation of unsteady separated flow. *International Journal of Heat and Fluid Flow*, 24(2):147–156, 2003.

[77] International Energy Agency (IEA). *Key World Energy Statistics 2010*. OECD/IEA, 2010.

[78] T. Ivanic, E. Foucault, and J. Pecheux. Dynamics of swirling jet flows. *Experiments in Fluids*, 35(4):317–324, 2003.

[79] S. Jakirlic, K. Hanjalic, and C. Tropea. Modeling rotating and swirling turbulent flows: A perpetual challenge. *Aiaa J.*, 40(10):1984–1996, 2002.

[80] J. Jeong and F. Hussain. On the identification of a vortex. *Journal of Fluids Mechanics*, 285:69–94, 1995.

[81] P. Jochmann, A. Sinigersky, M. Hehle, O. Schafer, R. Koch, and H. J. Bauer. Numerical simulation of a precessing vortex breakdown. *Int. J. Heat Fluid Flow*, 27(2):192–203, 2006.

[82] L. N. Jones, P. H. Gaskell, H. M. Thompson, X. J. Gu, and D. R. Emerson. Anisotropic, isothermal, turbulent swirling flow in a complex combustor geometry. *Int. J. Numer. Meth. Fluids*, 47:1053–1059, 2005.

[83] B. C. Khoo, K. S. Yeo, D. F. Lim, and X. He. Vortex breakdown in an unconfined vortical flow. *Experimental Thermal and Fluid Science*, 14(2):131–148, 1997.

[84] S. Kim, H., K. Arghode, V., B. Linck, M., and K. Gupta, A. Hydrogen addition effects in a confined swirl-stabilized methane-air flame. *International Journal of Hydrogen Energy*, 34(2):1054–1062, 2009.

[85] W. Kriaa, K. Abderrazak, G. M., H.and LePalec, and P. Bournot. A numerical study of non-isothermal turbulent coaxial jets. *Heat and Mass Transfer*, 44(9):1051–1063, 2008.

[86] C. Külsheimer and H. Büchner. Combustion dynamics of turbulent swirling flames. *Combust. Flame*, 131(1-2):70–84, 2002.

[87] M. Kurosaka, M. Kikuchi, K. Hirano, T. Yuge, and H. Inoue. Interchangeability of vortex-breakdown types. *Experiments in Fluids*, 34(1):77–86, 2003.

[88] B. E. Launder. Second-moment closure and its use in modeling turbulent industrial flows. *International Journal for Numerical Methods in Fluids*, 9:963–985, 1989.

[89] B. E. Launder. Second-moment closure: present... and future? *International Journal of Heat and Fluid Flow*, 10(4):282–300, 1989.

[90] B. E. Launder, G. J. Reece, and W. Rodi. Progress in the development of reynolds-stress turbulence closure. *J. Fluid Mech.*, 68(3):537–566, 1975.

[91] B. E. Launder and D. B. Spalding. *Lectures in mathematical models of turbulence*. Academic Press, London, England, 1972.

[92] B. E. Launder and D. B. Spalding. The numerical computation of turbulent flows. *Computer Methods in Applied Mechanics and Engineering*, 3(2):269–289, 1974.

[93] K. H. Lee, T. Setoguchi, S. Matsuo, and H. D. Kim. An experimental study of the under-expanded swirling jet with secondary coaxial stream. In *24th International Symposium on Shock Waves*, pages 83–92, Beijing, PEOPLES R CHINA, 2004. Springer.

[94] M. Legrand. *Estudio y caracterización de un quemador estabilizado con giro*. PhD thesis, 2008.

[95] M. Legrand, J. Nogueira, A. Lecuona, S. Nauri, and P. A. Rodriguez. Atmospheric low swirl burner flow characterization with stereo piv. *Experiments in Fluids*, 48(5):901–913, 2010.

[96] Y. Lei, J. Zhang, and L. X. Zhou. Simulation of swirling turbulent flows of coaxial jets in a combustor. *Numerical Heat Transfer Part A-Applications*, 37(2):189–199, 2000. ISI Document Delivery No.: 288GG Times Cited: 1 Cited Reference Count: 18 HEMISPHERE PUBL CORP.

[97] S. Leibovich. Structure of vortex breakdown. *Annu. Rev. Fluid Mech.*, 10:221–246, 1978.

[98] H. Liang and T. Maxworthy. Experimental investigations of a swirling jet in both stationary and rotating surroundings. *Experiments in Fluids*, 45(2):283–293, 2008.

[99] T. T. Lim and Y. D. Cui. On the generation of a spiral-type vortex breakdown in an enclosed cylindrical container. *Phys. Fluids*, 17(4):9, 2005.

[100] C.A. Lin. Modeling a confined swirling coaxial jet. *Centre for Turbulence Reseach. Annual Research Briefs*, pages 211–219, 1998.

[101] O. Lucca-Negro and T. O'Doherty. Vortex breakdown: a review. *Prog. Energy Combust. Sci.*, 27(4):431–481, 2001.

[102] L. Lumley, J. The structure of inhomogeneous turbulence. In V. I. Tatarski ed. by A. M., Yaglom, editor, *Atmospheric Turbulence and Wave Propagation*, pages 166–178, Nauka, Moscow, 1967.

[103] L. Lumley, J. *Stochastic tools in turbulence*. Academic, New York, 1970.

[104] W. Malalasekera, Kkjr Dinesh, S. S. Ibrahim, and M. P. Kirkpatrick. Large eddy simulation of isothermal turbulent swirling jets. *Combust. Sci. Technol.*, 179(8):1481–1525, 2007.

[105] W. Malalasekera, K. K. J. Ranga-Dinesh, S. S. Ibrahim, and A. R. Masri. Les of recirculation and vortex breakdown in swirling flames. *Combust. Sci. and Tech.*, pages 809–832, 2008.

[106] F. Martinelli, A. Olivani, and A. Coghe. Experimental analysis of the precessing vortex core in a free swirling jet. *Exp. Fluids*, 42(6):827–839, 2007.

[107] W. Meier, P. Weigand, X. R. Duan, and R. Giezendanner-Thoben. Detailed characterization of the dynamics of thermoacoustic pulsations in a lean premixed swirl flame. *Combustion and Flame*, 150(1-2):2–26, 2007.

[108] H. Mocikat, T. Gurtler, D. Petrak, and H. Herwig. Ldv measurements in complex swirling flows, their physics and a database for cfd evaluations. *Exp. Fluids*, 46(4):693–704, 2009.

[109] S. Mondal, A. Datta, and A. Sarkar. Influence of side wall expansion angle and swirl generator on flow pattern in a model combustor calculated with k-[var epsilon] model. *International Journal of Thermal Sciences*, 43(9):901–914, 2004.

[110] D. Mourtazin and J. Cohen. The effect of buoyancy on vortex breakdown in a swirling jet. *J. Fluid Mech.*, 571:177–189, 2007.

[111] F. Novak and T. Sarpkaya. Turbulent vortex breakdown at high reynolds numbers. *Aiaa J.*, 38(5):825–834, 2000.

[112] A. Olivani, G. Solero, F. Cozzi, and A. Coghe. Near field flow structure of isothermal swirling flows and reacting non-premixed swirling flames. *Experimental Thermal and Fluid Science*, 31(5):427–436, 2007.

[113] B. Patte-Rouland, G. Lalizel, J. Moreau, and E. Rouland. Flow analysis of an annular jet by particle image velocimetry and proper orthogonal decomposition. *Meas. Sci. Technol.*, 12:1404–1412, 2001.

[114] B. Patte-Rouland, G. Lalizel, J. Moreau, and E. Rouland. Flow analysis of an annular jet by particle image velocimetry and proper orthogonal decomposition. *Measurement Science and Technology*, 12(9):1404–1412, 2001. Cited By (since 1996): 36 Export Date: 24 April 2011 Source: Scopus.

[115] R. Perrin, M. Braza, E. Cid, S. Cazin, A. Barthet, A. Sevrain, C. Mockett, and F. Thiele. Obtaining phase averaged turbulence properties in the near wake of a circular cylinder at high reynolds number using pod. *Experiments in Fluids*, 43(2):341–355, 2007.

[116] S. Pfadler, A. Leipertz, F. Dinkelacker, J. Wäsle, A. Winkler, and T. Sattelmayer. Two-dimensional direct measurement of the turbulent flux in turbulent premixed swirl flames. *Proceedings of the Combustion Institute*, 31(1):1337–1344, 2007.

[117] S. B. Pope. *Turbulent Flows*. Cambridge University Press, 2000.

[118] K. J. Ranga Dinesh, K. and P. Kirkpatrick, M. Study of jet precession, recirculation and vortex breakdown in turbulent swirling jets using les. *Computers & Fluids*, 38(6):1232–1242, 2009.

[119] S. Reza. An experimental investigation of the near-field flow development in coaxial jets. *Physics of Fluids*, 15(5):1233–1246, 2003.

[120] L. F. Richardson. The approximate arithmetical solution by finite differences of physical problems involving differential equations, with an

application to the stresses in a masonty dam. *Transactions of the Royal Society of London, Ser. A*, 210:307–357, 1910.

[121] L. F. Richardson and J. A. Gaunt. The deferred approach to the limit. *Philos. Trans. R. Soc. London, Ser. A*, 226:299–361, 1927.

[122] P. J. Roache. Quantification of uncertainty in computational fluid dynamics. *Annu. Rev. Fluid Mech.*, 29:123–160, 1997.

[123] P. J Roache. *Verification and validation in computational science and engineering*. Hermosa Publishers, Albuquerque, 1998.

[124] S. Roux, G. Lartigue, T. Poinsot, U. Meier, and C. BÃ©rat. Studies of mean and unsteady flow in a swirled combustor using experiments, acoustic analysis, and large eddy simulations. *Combustion and Flame*, 141(1-2):40–54, 2005.

[125] M. R. Ruith, P. Chen, E. Meiburg, and T. Maxworthy. Three-dimensional vortex breakdown in swirling jets and wakes: direct numerical simulation. *Journal of Fluid Mechanics*, 486(1):331–378, 2003.

[126] R. Sadanandan, M. Stohr, and W. Meier. Simultaneous oh-plif and piv measurements in a gas turbine model combustor. *Appl. Phys. B-Lasers Opt.*, 90(3-4):609–618, 2008.

[127] A. Sadiki, A. Maltsev, B. Wegner, F. Flemming, A. Kempf, and J. Janicka. Unsteady methods (urans and les) for simulation of combustion systems. *International Journal of Thermal Sciences*, 45(8):760–773, 2006.

[128] P. G. Saffman and G. R. Baker. Vortex interactions. *Annual Review of Fluid Mechanics*, 11:95–122, 1979.

[129] E. Sanmiguel-Rojas, M. A. Burgos, C. del Pino, and R. Fernandez-Feria. Three-dimensional structure of confined swirling jets at moderately large reynolds numbers. *Physics of Fluids*, 20(4):044104–13, 2008.

[130] T. Sarpkaya. On stationary and travelling vortex breakdowns. *Journal of Fluid Mechanics Digital Archive*, 45(03):545–559, 1971.

[131] T. Sarpkaya. Turbulent vortex breakdown. *Phys. Fluids*, 7(10):2301–2303, 1995.

[132] U. Schildmacher, K., R. Koch, and H. J. Bauer. Experimental characterization of premixed flame instabilities of a model gas turbine burner. *Flow, Turbulence and Combustion*, 76(2):177–197, 2006.

[133] C. Schneider, A. Dreizler, and J. Janicka. Fluid dynamical analysis of atmospheric reacting and isothermal swirling flows. *Flow Turbul. Combust.*, 74(1):103–127, 2005.

[134] E. Schneider, A. Maltsev, A. Sadiki, and J. Janicka. Study on the potential of bml-approach and g-equation concept-based models for predicting swirling partially premixed combustion systems: Urans computations. *Combustion and Flame*, 152(4):548–572, 2008.

[135] L. Selle, G. Lartigue, T. Poinsot, R. Koch, K. U. Schildmacher, W. Krebs, B. Prade, P. Kaufmann, and D. Veynante. Compressible large eddy

simulation of turbulent combustion in complex geometry on unstructured meshes. *Combust. Flame*, 137(4):489–505, 2004.

[136] H. J. Sheen, W. J. Chen, and S. Y. Jeng. Recirculation zones of unconfined and confined annular swirling jets. *Aiaa J.*, 34(3):572–579, 1996.

[137] S. I. Shtork, C. E. Cala, and E. C. Fernandes. Experimental characterization of rotating flow field in a model vortex burner. *Exp. Therm. Fluid Sci.*, 31(7):779–788, 2007.

[138] S. I. Shtork, C. E. Cala, E. C. Fernandes, and M. V. Heitor. Coherent helical structures in swirl flows. *Tech. Phys. Lett.*, 31(8):660–662, 2005.

[139] S. I. Shtork, N. F. Vieira, and E. C. Fernandes. On the identification of helical instabilities in a reacting swirling flow. *Fuel*, 87(10-11):2314–2321, 2008.

[140] G. A. Siamas, X. Jiang, and L. C. Wrobel. Direct numerical simulation of the near-field dynamics of annular gas-liquid two-phase jets. *Physics of Fluids*, 21(4):14, 2009. ISI Document Delivery No.: 456XF Times Cited: 0 Cited Reference Count: 54 Siamas, George A. Jiang, Xi Wrobel, Luiz C. AMER INST PHYSICS.

[141] L. Sirovich. Turbulence and the dynamics of coherent structures. i - coherent structures. ii - symmetries and transformations. iii - dynamics and scaling. *Quarterly of Applied Mathematics*, 45:561–571, 1987.

[142] P. R. Spalart. Strategies for turbulence modelling and simulations. *International Journal of Heat and Fluid Flow*, 21(3):252–263, 2000.

[143] R. E. Spall and B. M. Ashby. A numerical study of vortex breakdown in turbulent swirling flows. *J. Fluids Eng.-Trans. ASME*, 122(1):179–183, 2000.

[144] R. E. Spall and T. B. Gatski. A computational study of the topology of vortex breakdown. *Proc. R. Soc. London Ser. A-Math. Phys. Eng. Sci.*, 435(1894):321–337, 1991.

[145] R. E. Spall, T. B. Gatski, and R. L. Ash. The structure and dynamics of bubble-type vortex breakdown. *Proc. R. Soc. London Ser. A-Math. Phys. Eng. Sci.*, 429(1877):613–637, 1990.

[146] A. Spencer, J. McGuirk, J., and K. Midgley. Vortex breakdown in swirling fuel injector flows. *Journal of Engineering for Gas Turbines and Power*, 130(2):021503–8, 2008.

[147] H. B. Squire. Analysis of the vortex breakdown phenomenon. part i. *Miszellaneen der angewandten Mechanik*, pages 306–312, 1962.

[148] O. Stein and A. Kempf. Les of the sydney swirl flame series: A study of vortex breakdown in isothermal and reacting flows. *Proc. Combust. Inst.*, 31:1755–1763, 2007.

[149] C. Stone and S. Menon. Parallel simulations of swirling turbulent flames. *The Journal of Supercomputing*, 22(1):7–28, 2002.

[150] T. Stuart, J. A critical review of vortex-breakdown theory. In *Proc. Symp. Vortex Control and Breakdown Behaviour*, Baden, Switzerland, 1987.

[151] N. Syred. A review of oscillation mechanisms and the role of the precessing vortex core (pvc) in swirl combustion systems. *Progress in Energy and Combustion Science*, 31:93–161, 2006.

[152] M. Tanahashi, S. Inoue, M. Shimura, S. Taka, G. M. Choi, and T. Miyauchi. Reconstructed 3d flame structures in noise-controlled swirl-stabilized combustor. *Exp. Fluids*, 45(3):447–460, 2008.

[153] G. Tang, Z. Yang, and J. J. McGuirk. Large eddy simulation of isothermal confined swirling flow with recirculation. *In: Rodi, W. Fueyo N. Engineering Turbulence Modelling and Measurements 5*, pages 885–894, 2002.

[154] D. Toporov, P. Bocian, P. Heil, A. Kellermann, H. Stadler, S. Tschunko, M. Förster, and R. Kneer. Detailed investigation of a pulverized fuel swirl flame in co2/o2 atmosphere. *Combustion and Flame*, 155(4):605–618, 2008.

[155] A. Townsend, A. *The Structure of Turbulent Shear Flow*. Cambridge University Press, Cambridge, 1976.

[156] M. J. Tummers, A. W. Hübner, E. H. van Veen, K. Hanjalic, and Th H. van der Meer. Hysteresis and transition in swirling nonpremixed flames. *Combustion and Flame*, 156(2):447–459, 2009.

[157] M. Vanierschot and E. Van den Bulck. Hysteresis in flow patterns in annular swirling jets. *Experimental Thermal and Fluid Science*, 31(6):513–524, 2007.

[158] M. Vanierschot and E. Van den Bulck. Influence of swirl on the initial merging zone of a turbulent annular jet. *Physics of Fluids*, 20(10):105104–18, 2008.

[159] P. Wang and S. Bai, X. Large eddy simulations of turbulent swirling flows in a dump combustor: a sensitivity study. *International Journal for Numerical Methods in Fluids*, 47(2):99–120, 2005.

[160] P. Wang, X. S. Bai, M. Wessman, and J. Klingmann. Large eddy simulation and experimental studies of a confined turbulent swirling flow. *Physics of Fluids*, 16(9):3306–3324, 2004.

[161] B. Wegner, A. Maltsev, C. Schneider, A. Sadiki, A. Dreizler, and J. Janicka. Assessment of unsteady rans in predicting swirl flow instability based on les and experiments. *International Journal of Heat and Fluid Flow*, 25(3):528–536, 2004.

[162] X. Wei, J. Zhang, and L. X. Zhou. A new algebraic mass flux model for simulating turbulent mixing in swirling flow. *Numerical Heat Transfer Part B-Fundamentals*, 45(3):283–300, 2004. ISI Document Delivery No.: 775EG Times Cited: 8 Cited Reference Count: 13 TAYLOR & FRANCIS INC.

[163] P. Weigand, W. Meier, R. Duan, X., W. Stricker, and M. Aigner. Investigations of swirl flames in a gas turbine model combustor - i. flow field, structures, temperature, and species distributions. *Combust. Flame*, 144(1-2):205–224, 2006.

[164] P. Weigand, W. Meier, X. R. Duan, R. Giezendanner-Thoben, and U. Meier. Laser diagnostic study of the mechanism of a periodic combustion instability in a gas turbine model combustor. In *2nd International Workshop on Trends in Numerical and Physical Modelling of Turbulent Processes in Gas Turbine Combustors and Automotive Engines*, pages 275–292, Heidelberg, GERMANY, 2004. Springer.

[165] B. Wicker, R. and K. Eaton, J. Structure of a swirling, recirculating coaxial free jet and its effect on particle motion. *International Journal of Multiphase Flow*, 27(6):949–970, 2001.

[166] L. Xia, J., L. Smith, B., C. Benim, A., J. Schmidli, and G. Yadigaroglu. Effect of inlet and outlet boundary conditions on swirling flows. *Computers & Fluids*, 26(8):811–823, 1997.

[167] H. T. Xu and J. L. Niu. Numerical simulation and experimental validation of the swirling turbulent air flow and mixing processes. *Numerical Heat Transfer Part A-Applications*, 46(6):571–586, 2004. ISI Document Delivery No.: 853QR Times Cited: 8 Cited Reference Count: 31 TAYLOR & FRANCIS INC.

[168] L. Young, D., B. Liao, C., and J. Sheen, H. Computations of recirculation zones of a confined annular swirling flow. *International Journal for Numerical Methods in Fluids*, 29(7):791–810, 1999.

[169] J. Zhang and C. M. Chen. Simulation of turbulent reacting flow in a swirl combustor. *Numerical Heat Transfer Part A-Applications*, 53(6):605–624, 2008. ISI Document Delivery No.: 231XN Times Cited: 4 Cited Reference Count: 18 Zhang, Jian Chen, Chunming TAYLOR & FRANCIS INC.

[170] J. Zhang, J. B. He, L. X. Zhou, and S. Nieh. Simulation of swirling turbulent heat transfer in a vortex heat exchanger. *Numerical Heat Transfer Part A-Applications*, 48(7):607–625, 2005. ISI Document Delivery No.: 972UM Times Cited: 3 Cited Reference Count: 13 TAYLOR & FRANCIS INC.

[171] J. Zhang and C. K. Zhu. Simulation of swirling turbulent flow and combustion in a combustor. *Numerical Heat Transfer Part A-Applications*, 55(5):448–464, 2009. ISI Document Delivery No.: 415JN Times Cited: 1 Cited Reference Count: 18 Zhang, Jian Zhu, Chengkai TAYLOR & FRANCIS INC.